Spring 4-2006

A Mutagenic Approach to Test a Structural Model for the Self-Association of Human Plasma Vitronectin

Kevin C. Walters
University of Tennessee-Knoxville

A Mutagenic Approach to Test a Structural Model for the Self-Association of Human Plasma Vitronectin

Kevin C. Walters
Senior Honors Thesis
Spring 2006
Dr. Cynthia Peterson

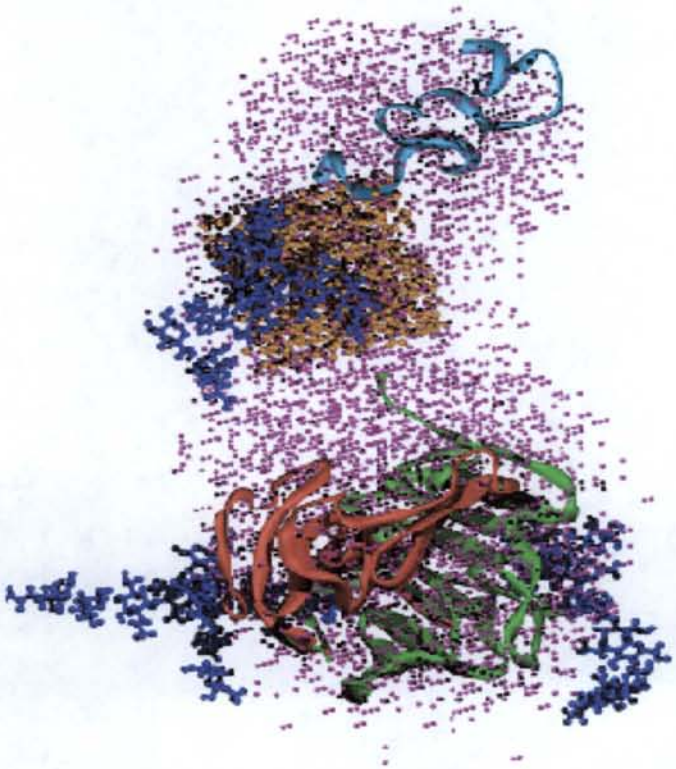

Abstract

Vitronectin is a multifunctional glycoprotein found in both the circulation and the extracellular matrix (ECM). Through its capacity to interact with a wide variety of ligands it helps to mediate several key physiological processes. These include coagulation, cell adhesion and migration, tumor metastasis and tissue remodeling, and immune system response. An interesting feature of the protein is its ability to adopt different functional forms, presumably as a result of varying physiological conditions. A monomeric form of vitronectin found in the circulation helps to regulate proteolytic cascades. Conversely, a multimeric form of vitronectin found in the ECM helps to regulate pericellular proteolysis as well as cell adhesion and migration. The process by which the monomer assembles into higher order complexes remains relatively uncharacterized, but is believed to be mediated by the binding of vitronectin to physiological partners including plasminogen activator inhibitor type-1 (PAI-1). This results in a structural change that is proposed to promote intermolecular self-association via polymerization of the central β-propeller domain.

The structures of several homologous proteins with a four-bladed β-propeller motif have been solved, but these naturally occurring β-sheet proteins typically do not associate into higher order oligomers. This suggests that in these cases regulatory features must exist which inhibit β-sheet interaction in favor of the monomeric protein. An extensive analysis of known β-sheet protein structures in the database (Richardson, JS., Richardson, DC. 2002. *PNAS*. 99:2754-2759) has resulted in a set of rules for β-strands that govern the formation of more extensive intra- or intermolecular structures. These authors suggest that certain features of β-edge strands may be responsible for preventing propagation via hydrogen bonding to additional β-strands. This analysis was used as a general guideline to examine the edge residues in the β-propeller structure

for the central domain of vitronectin in order to predict the features responsible for its associative behavior. Molecular models of the protein were studied and compared with homologous proteins known not to participate in self-association in order to make predictions about specific edge strands and amino acid residues involved. These observations were used to test predicted polymerization schemes via site directed mutagenesis of specific edge residues. Features noted in the Richardson study that prevented β-sheet interactions were incorporated at key points within the central domain of vitronectin. This strategy should provide valuable insight into the mechanistic aspect of the formation of vitronectin complexes. Furthermore, this study serves as an important test of the notion that specific structural features may serve as a "negative design" to inhibit β-sheet association and can be used to distinguish central and peripheral strands in β-propeller structures.

Introduction

Vitronectin is a human plasma glycoprotein found in both the circulation and the extracellular matrix (ECM). Produced primarily in the liver, it has the capacity to interact with a wide variety of ligands which helps it to mediate such key physiological processes as coagulation, cell adhesion and migration, tumor metastasis and tissue remodeling, and immune system response (Xu et al. 2001). Since its discovery in 1967, extensive research has been performed with the primary focus of characterizing the binding sites for various ligands. The desire to better understand the functionality of the protein, however, necessitates a better understanding of its three dimensional structure. Although vitronectin has not been successfully crystallized and remains too large for high-resolution structural determination by NMR, a general sense of its organization can be surmised from preliminary data.

Vitronectin is organized into three separate domains that allow for the numerous biochemical properties of the functional protein. The 53-residue N-terminal domain consists of 44 amino acids identical to the circulating protein somatomedin B (Suzuki et al 1984). Contained within this domain are binding sites for plasminogen activator inhibitor type 1 (PAI-1) (Sieffert et al. 1991), integrins (Cherney et al. 1993), and the urokinase plasminogen activator receptor (uPAR) (Deng et al. 1996). An unstructured linker region (residues 54-130) connects the N-terminal domain with a central domain (residues 131-342) thought to mediate binding to some

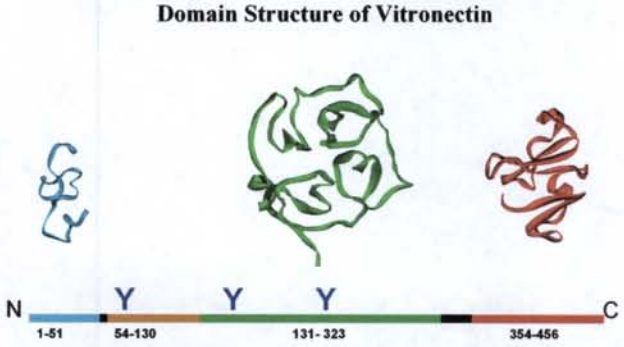

Fig. 1. Domain structure of vitronectin. The Structures for the N-terminal somatomedin B, central β-propeller, and C-terminal heparin binding domains as predicted by combined computational analyses and NMR measurements. Lynn et al (2005) Biochemistry 44, 565-74.

bacteria including *Staphylococcus aureus* and *Staphylococcus pyogenes* (Liang et al. 1993, 1997). The C-terminal domain (residues 347-459) serves as the binding site for several ligands including heparin (Kost et al. 1992) and collagen (Ishikawa-Sakurai et al. 1993).

Computational threading and docking algorithms (Xu et al. 2001), while somewhat unsuccessful for the N-terminal somatomedin B (SMB) domain, have predicted a four bladed β-propeller fold for the central domain (probability > 99%) and a two bladed β-propeller fold for the C-terminal domain (probability > 90%). Subsequent studies have solved the structure of the SMB domain through two-dimensional NMR (Mayasundari et al. 2004) and peptide mapping to identify disulfide bonds (Horn et al. 2004). Additional studies using small angle x-ray scattering measurements (Lynn et al. 2004) have successfully generated low resolution models predicting an overall peanut shape for the intact protein (see cover).

As these models indicate, the central domain of vitronectin contains extensive β-sheet content. We hypothesize that this feature makes the central domain integral for one of vitronectin's more notable features, its ability to adopt different functional forms presumably as a result of varying physiological conditions. A monomeric form of vitronectin is found in the circulation where it helps to mediate proteolytic cascades. Conversely, a multimeric form of vitronectin is found in the ECM where it helps to regulate pericellular proteolysis, cell adhesion, and cell migration. The process by which the monomer assembles into higher order complexes remains relatively uncharacterized, but is believed to be mediated by the binding of vitronectin to PAI-1, one of its most physiologically significant binding partners.

Through its association with vitronectin, PAI-1 plays a key role in the remodeling of the extracellular matrix that occurs during physiological processes like fibrinolysis and cell migration and pathophysiological processes like tumor growth and metastasis (Reuning et al.

1998). A serine protease inhibitor (serpin), PAI-1 is the primary inhibitor of both the urokinase- and tissue-type plasminogen activators which allows it to regulate vascular and pericellular plasmin-mediated proteolysis. Although PAI-1 is conformationally labile and has a tendancy to spontaneously adopt a more stable yet inactive conformation, its circulating form is found primarily in association with vitronectin which has been demonstrated to substantially increase its half life (Declereck et al. 1988).

Both PAI-1 and vitronectin have been shown to co-localize to areas of active ECM remodeling as occurs with tissue injury or tumor invasion (Bloemendal et al. 2004). While PAI-1 is secreted locally into the pericellular environment, vitronectin is incorporated from a circulatory pool by an undefined mechanism. Several lines of evidence show that, in addition to the stabilization effect vitronectin has on PAI-1, PAI-1 reciprocally affects the binding properties of vitronectin. Namely, the binding of PAI-1 to vitronectin has been show to convert the protein to a multimeric form that displays enhanced binding to the ECM (Minor et al. 2002). A later sedimentation velocity analysis (Minor et al. 2005) has provided a mechanism for the assembly of these complexes in a stepwise and concentration-dependent manner. Low concentrations of PAI-1 occupy

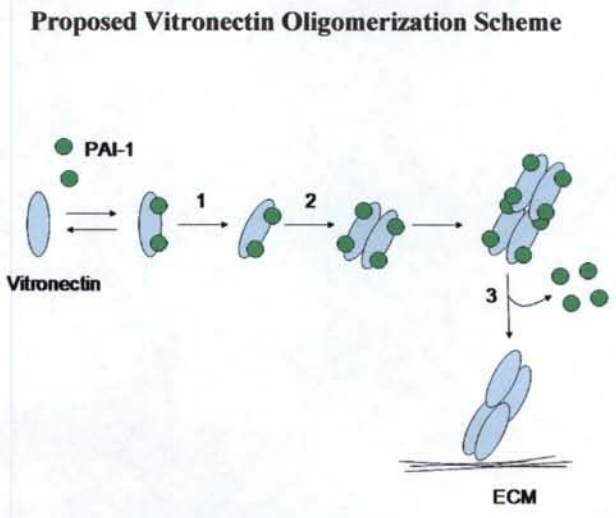

Fig. 2. The interaction of vitronectin with PAI-1 in a 2:1 stoichiometry induces a conformational change in the protein (1) which favors self association and the formation of multivalent vitronectin complexes (2) through intermolecular β-sheet polymerization of the central domain. These large complexes are highly stable and display enhanced binding to the extracellular matrix.

a single high affinity binding site in the SMB domain and form a 1:1 soluble complex. Higher concentrations of PAI-1 have been shown to bind to a second lower affinity binding site (Podor et al. 2000) on vitronectin forming a 2:1 insoluble complex with localization and function distinctly different from its plasma counterpart (Bloemendal et al. 2004). It was demonstrated that PAI-1 bound to both vitronectin binding sites simultaneously, and suggested that this formation of a 2:1 complex is the critical step for the assembly of higher order complexes (Minor et al. 2005). Unpublished stopped- flow kinetics data from this lab indicate that the unique 2:1 PAI-1/vitronectin complex undergoes a conformational change allowing assembly of the 4:1 complex and ultimately large oligomers with altered function.

On a structural level, we hypothesize that it is the central domain of vitronectin with its extensive β-sheet content that allows the formation of these complexes through intermolecular associations of its β-sheets. It has been well established that β-propellers are prominent structures for the intermolecular associations of proteins. This is supported by protein interactions such as the WD-40 structures in signal transduction (Chen et al. 2004), β-propeller domains in matrix metalloproteinases (Stricker et al. 2001), and the head regions of integrins that recognize ECM ligands (Springer et al. 2002). These examples are supporting evidence for this idea that the central domain is the primary mediator of intermolecular associations. Furthermore, both the N-terminal and C-terminal domains have been eliminated as candidates for involvement in the formation of higher order complexes. The SMB domain when isolated has been shown to be stable and monomeric under physiological conditions (Mayasundari et al. 2004), and the folding and denaturation of vitronectin have shown that binding of the heparin ligand to the C-terminal domain does not disrupt the formation of higher-order complexes (Zhuang et al. 1996).

The structures of several homologous proteins with a four-bladed propeller motif have also been solved, but these naturally occurring β-sheet proteins typically do not associate into higher order oligomers. This suggests that in these cases regulatory features must exist that inhibit β-sheet interaction in favor of the monomeric protein. Additionally, unchecked β-bonding has been implicated in the pathology of many diseases such as the fibrillar structure associated with some neurodegenerative disorders including Alzheimer's (Kirschner et al. 1986). Extensive analysis of β-sheet proteins performed by Richardson et al. (2004) has resulted in a set of rules for β-strands that govern the formation of more extensive intra- or intermolecular structures. The results of this study showed that β-sheet proteins use various combinations of β-bulges, prolines, charged residues, short edge strands, and loop shielding to prevent aggregation and maintain solubility.

Structurally, β-propeller proteins are known to exist in conformations of four to eight radial blades comprised of up-and-down β-sheet structures. The innermost edges of the structure are protected from further β-interactions by the inherent fold of the molecule. Among the different edge blocking strategies used, the Richardson study identified two predominant patterns that were observed in approximately thirty of the thirty-five β-propeller structures in the sample. The first strategy is the placement of a charged side chain on a low-curvature surface next to the edge strand where it would be buried most by potential β-sheet associations. The location of this chain is variable – it may be on the edge strand itself, on the next strand, or even contributed by an adjacent structure. The second predominant strategy is the use of a β-bulge or proline residue to disfavor further β-sheet interactions via structural hindrance of β-bonding on the convex side of the strand. This study also identified several less common means of protection employed by β-edge residues with the general observation being that the edge strands of most naturally

occurring β-sheet proteins are shielded, irregular, short, or otherwise made unsuitable for further interactions. These mechanisms serve to promote stability over aggregation, and are termed negative design as they do not improve the general structure of the β-sheet, but exist as a preventative measure for an undesirable alternative.

Aims of this Research Plan

One important implication of the Richardson study is that one may use specific structural features to distinguish central and peripheral strands in β-propeller structures, and that these features may be incorporated as a means to inhibit intermolecular β-sheet associations. Our hypothesis is that the PAI-1 induced formation of vitronectin complexes is mediated by β-sheet associations of the central domain. Based on this, the first goal of this study was to locate and characterize the edge residues on the β-propeller region in the central domain of vitronectin. This identification was then compared to the negative design features highlighted by the Richardson study to make preliminary conjectures about the ability of the edge residues to undergo β-sheet polymerization as a mode of *in vivo* aggregation resulting in the multimeric matrix form of the protein. The β-propeller structural model was also compared with its homologues that do not undergo a self-association event in order to catalogue any differences that may result in disparate behavior. After completion of the structural analysis and a general prediction of edge strand involvement in self-association, the second goal was to test these predictions through mutagenesis studies. Site directed mutagenesis was used to incorporate negative design features in order to further define the edge strands and specific residues involved. This should provide valuable insight into the mechanistic aspect of the formation of vitronectin complexes, and help

to test the notion that specific structural features may serve as negative design to further inhibit β-sheet associations.

Materials and Methods

Structural analysis of vitronectin and homologues—The proposed β-propeller structure for the central domain of vitronectin (Xu et al. 2001) was compared with the crystal structure of its hemopexin (Faber et al. 1995), gelatinase (Gohlke et al. 1996), and collagenase (Gomis-Ruth et al. 1996) homologues using the molecular modeling program Insight II. Each of the structures was aligned based on common features including the location of bulges and the overall folding pattern. Each structure was examined individually to determine which edge strand amino acid residues appeared capable of participating in intermolecular β-sheet bonding. Finally, the edge strands identified for each structure were compared in order to identify any sequence homologies and obvious negative design strategies incorporated within the structure of the protein. These observations were used to design rational mutations for the incorporation of negative design within wild-type vitronectin.

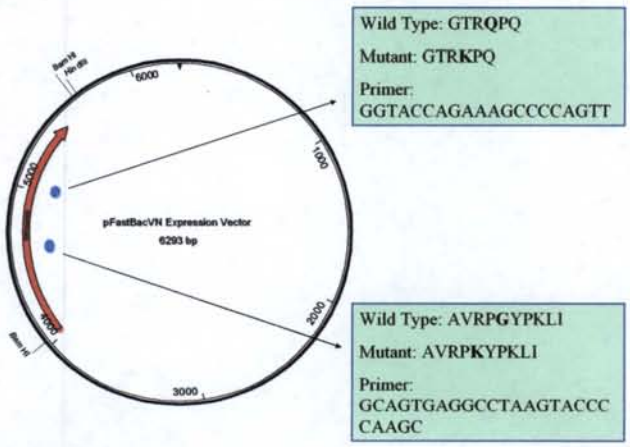

Fig. 3. This shows the primers constructed for the mutagenesis experiments.

Oligonucleotide Design—Primers were designed with the aid of DNAstar's Lasergene 7 genome analysis program. One forward primer was created for each mutation thus allowing for simultaneous mutagenesis of the same strand of the template plasmid. Primer #1 for the upper left strand changed glutamine 331 to a lysine residue. It was 20 base pairs in length with a calculated T_m of 70°C, one mismatch (asterisked), and a sequence of 5'-GGTACCAGAA*AGCCCCAGTT-3'. Primer #2 for the lower left strand changed glycine 191 to a lysine residue. It was 25 base pairs in length with a calculated T_m of

70°C, two mismatches (asterisked), and a sequence of 5'-GCAGTGAGGCCTA*A*GTACCCCAAGC-3'. Each of these mutations was selected to incorporate the charged residue towards the center of the edge strand and have a minimal impact on protein folding.

Mutagenesis/Screening—Site directed mutagenesis was performed on wild type vitronectin cDNA cloned into the pFastBac expression vector (Gibson et al. 2001) using the described primers and the QuikChange Multi Site-Directed Mutagenesis Kit purchased from Stratagene. The expression vector was grown in *E. coli* DH10α cells and prepared with the Qiagen plasmid miniprep kit. The experimental reaction was carried out with the following mixture: 2.5µl 10x QuikChange Multi reaction buffer, 16µl distilled water (to a final volume of 25µL), 1µl ds-DNA template (50ng), 2µl primer #1 (100ng), 1.5µl primer #2 (100ng), 1µl dNTP mix, and 1µl QuikChange Multi enzyme blend. The reaction was performed for 30 cycles with the following temperatures and times: 95°C at 1 minute, 55°C for 1 minute, 65°C for 12 minutes. 1µl of the *Dpn* I restriction enzyme was added to each amplification reaction to digest any remaining template DNA. 1.5µl of the *Dpn* I-treated DNA was transformed into XL10-Gold Ultracompetent Cells which added the second strand to the single stranded mutant plasmid. The general transformation procedure was as follows: 45µl of XL10-Gold Ultracompetent cells were thawed on ice and mixed with 2µl of β-mercaptoethanol for 10 minutes. The DNA was then added and the mix was incubated on ice for 30 min. The reaction was then heat-pulsed at 42°C for 30 seconds after which time 0.5ml of preheated (42°C) NZY+ broth was added and the mix was incubated with shaking (250 rpm) at 37°C for one hour. The transformants were screened by plating on LB-ampicillin agar plates. After an incubation period of 16 hours at 37°C, 5 colonies

were selected, grown in LB-ampicillin broth, and the DNA was isolated with the Qiagen plasmid miniprep kit. Samples were then sequenced to ensure proper incorporation of both mutations.

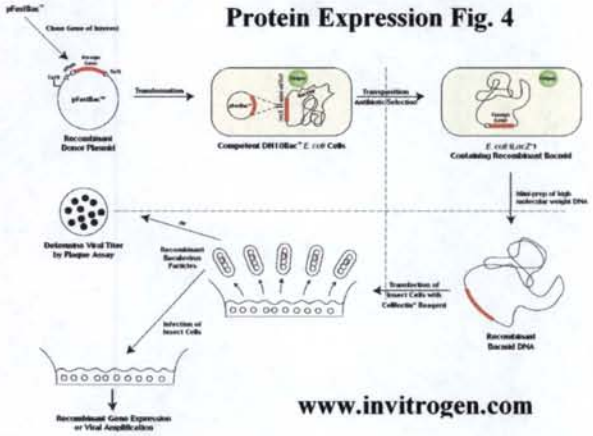

Protein Expression Fig. 4

Expression in baculovirus—The mutant protein was expressed using the Bac-to-Bac Baculovirus Expression system purchased from Invitrogen. Recombinant Bacmid DNA was obtained by transforming the mutated pFastBac expression vector into DH10Bac *E. coli* cells for transposition into the Bacmid. Successful transposition was verified through blue/white selection on LB-agar plates with kanamycin, gentamycin, and tetracycline. White colonies were selected and re-streaked on LB-agar plates with antibiotics to verify transposition. The recombinant bacmid DNA was then isolated using the S.N.A.P. MidiPrep Kit purchased from Invitrogen.

For the expression in Sf9 insect cells, 9 x 10^5 Sf9 cells per well were plated in a 6-well tissue culture plate in 2 ml of unsupplemented Grace's Medium and allowed to attach for one hour. DNA was transfected into the cells using the Cellfectin reagent purchased from Invitrogen. 200µl of the DNA:lipid complex was added to 0.8ml of Grace's Medium. This was then added to the attached cells which were incubated at 27°C for 5 hours. After the incubation period, the DNA:lipid complexes were removed and 2ml of complete growth media were added to the cells which were incubated at 27°C for 72 hours.

After the 72 hour incubation period, the medium containing the P1 viral stock was collected and centrifuged to remove cells and large debris. This was stored at +4°C protected from light. Cell fractions were obtained by boiling the cells in SDS reducing buffer, centrifuging

to remove cellular debris, and collecting the lysate. Both the lysate and a sample from the P1 viral stock were analyzed for protein expression using SDS-PAGE and Western Blot.

Protein Analysis—Samples from both the cell fraction and the media fraction were analyzed for vitronectin content using SDS-PAGE. Samples were initially boiled in SDS-reducing buffer for five minutes and loaded onto a 10% polyacrylamide gel where they were allowed to run at 100V for an hour. After this time span, the gel was subjected to a Western Blot and stained with anti-vitronectin antibodies (made in rabbit). The transfer for the Western Blot was performed by electroblotting onto nitrocellulose using a Biorad semi-dry blotting system. The sponges, nitrocellulose, and gel were saturated with transfer buffer (57.4g glycine, 12.0g tris base, 800ml methanol, 2L water) and blotted at 15V for 30 minutes. After this time, the nitrocellulose was soaked in a 10% milk blocking solution at room temperature for 1 hour with constant shaking. After the blocking period, it was washed with PBS + 0.1% weight/volume Tween (8g NaCl, 0.2g KCl, 1.44g Na_2HPO_4, 0.24g KH_2PO_4 for PBS and 2g Tween-80, 200mL 10X PBS for Tween), and placed in blocking solution containing the anti-vitronectin antibodies for 1 hour with constant shaking. The filter was again washed with PBS/Tween and submerged in blocking solution containing goat anti-rabbit antibody conjugated with alkaline phosphate horseradish peroxidase for 1 hour at room temperature. After washing again with PBS/Tween, the filter was placed in a 4-chloro-1-napthol developing solution and allowed to incubate until color appeared. The filters were then washed in tap water to stop the reaction and placed in aluminum foil at room temperature to preserve color.

Results

Structural analysis of vitronectin and homologues—Important information about the intermolecular self-association of vitronectin is gained from an analysis of the central domain believed to be the primary mediator. A proposed structural model for the central β-propeller domain (Xu et al. 2001) was analyzed both individually and docked with the rest of the protein in order to identify the edge residues that appeared capable of undergoing β-bonding. This model was then compared with the crystal structures of hemopexin (Faber et al. 1995), gelatinase (Gohlke et al. 1996), and collagenase (Gomis-Ruth et al. 1996) homologues which do not display intermolecular β-bonding behavior.

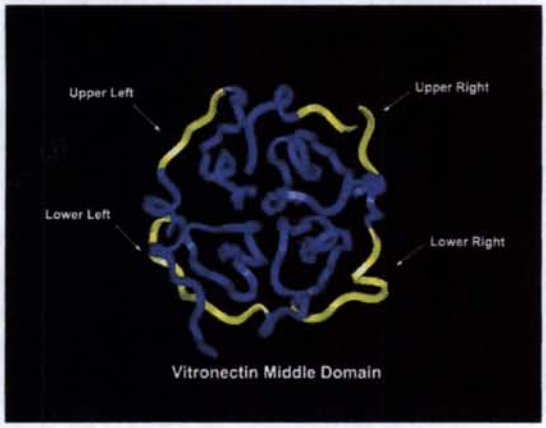

Fig. 5. The proposed structure for the central domain of vitronectin with the identified edge residues colored in yellow. The assigned strands for the respective blades are shown.

The first step in the structural analysis was the identification of edge residues on the β-propeller structure of the central domain. The highlighted sequences (Fig. 5) are the proposed edge residues for this domain of the protein. For the upper left strand of vitronectin, the identified amino acid sequence is –Gly-Thr-Arg-Gln-Pro-Gln. Proceeding clockwise around the molecule, the identified sequence for the upper right strand is –Ser-Gln-Glu-Glu-Cys-Glu-Gly-Ser. The sequence for the lower right strand is –Gly-Val-Leu-Asp-Pro-Asp-Tyr-Pro-Arg-Asn-. For the lower left strand, the identified sequence is –Ala-Val-Arg-Pro-Gly-Tyr-Pro-Lys-Leu-Ile.

In terms of negative design found in natural β-sheet proteins, several predictions can be made about the polymerization of vitronectin based on the identified structural features and amino acid sequences. Examination of the upper left strand of vitronectin shows that it contains

none of the structural motifs identified by the Richardson study (including bulges, shielding, and short length) that would be predicted to inhibit self-association. These findings are corroborated by the analysis of the amino acid sequence which shows the presence of a single charged species (arginine) and one proline. 3-D analysis of this strand with Insight II, however, shows that this proline does not induce a bulge that would appear to greatly disrupt potential β-sheet interactions. The charged residue is not at a noticeably "low" point within the molecule where it would be significantly buried by further intermolecular interactions. This analysis concludes that this portion of the structure lacks most negative design features and would predict that it could promote the formation of multimeric structures.

For the upper right strand of the protein, structural observation immediately shows a predominant bulge at the cysteine residue in the chain. The sulfhydryl group of this residue is responsible for the attachment of the C-terminal domain in the docked structure. A chemical analysis of this region of the molecule also shows that it contains three negatively charged residues (glutamate) that flank the cysteine bulge. This locates the charges at a low point in the chain where they would be buried by further β-sheet interactions. This segment of the protein contains both of the two most prevalent forms of negative design that have been well established as breakers of β-bonding. It is therefore predicted that this region would not participate heavily in intermolecular β-sheet polymerization.

Many of the same structural features observed in the upper right strand of vitronectin are also seen in the lower right strand, namely a predominant bulge in the center of the chain. This region also has three charged residues (aspartate, arginine), two of which flank the proline bulge. Because this region of the protein contains both of the primary negative design features, it is predicted to be unlikely to participate in intermolecular self-association.

Structural analysis of the lower left strand of vitronectin indicates that this may be a likely candidate for polymerization. There are no visible bulges, turns, or other structural hindrances. Although this region of the molecule does contain two charged residues (arginine, lysine), they do not conform to negative design observations as they do not appear to be localized at particularly low points within the molecule. This would argue that they do not inhibit the formation of β-bonds. This region also contains two prolines, but does not appear to be highly distorted. As it lacks both of the predominant features of negative design, it is likely that this region may also participate in β-sheet polymerization.

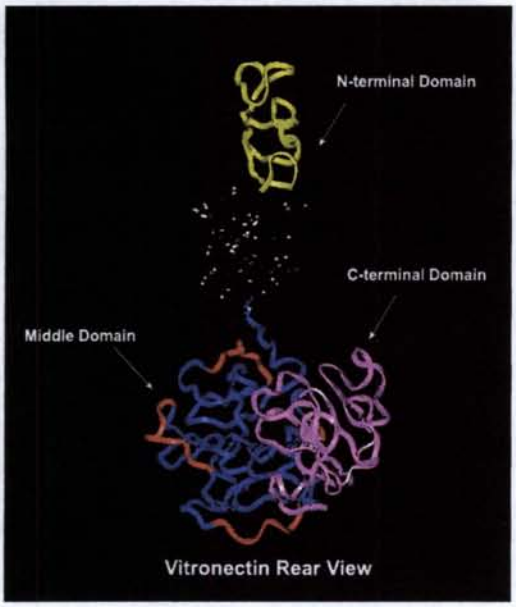

Fig. 6. Shows the holistic structure of the vitronectin protein. The N-terminal domain is colored in yellow, the middle domain in blue, and the C-terminal domain in purple. The red segments are the proposed edge residues for the central domain. Note how they appear to form a belt around the molecule.

An analysis of the location of the central domain edge residues on the holistic model predicted by small angle x-ray scattering measurements supports the initial conclusions for the likelihood of β-sheet polymerization. As shown in Figs. 6-8, the edge residues form a belt around the outside edge of the lower lobe of the protein. It is interesting to note that this leaves the edge strands in a position where they may participate in intermolecular interactions, and that there appears to be partial shielding by the c-terminal domain.

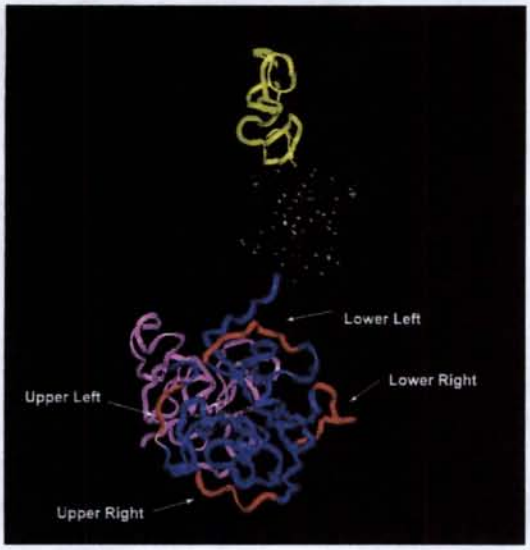

Fig. 7. This shows the location of the identified residues (separated into strands) relative to the holistic vitronectin protein

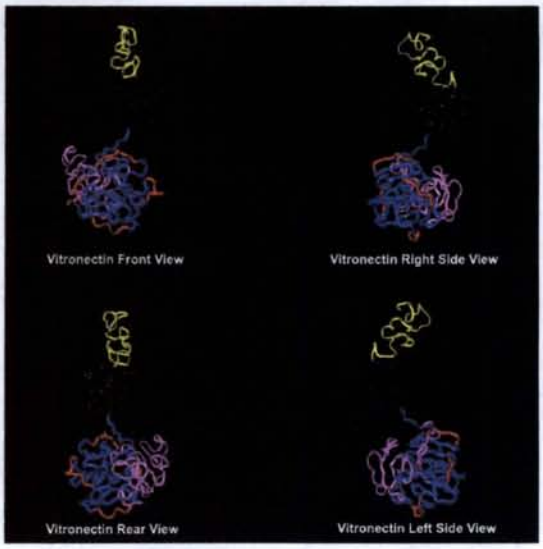

Fig. 8. This shows a 360° rotation of the vitronectin protein. The N-terminal domain is yellow, the middle domain is blue, and the C-terminal domain is purple. The red segments are the proposed edge residues for the central domain. Note the formation of the band around the molecule.

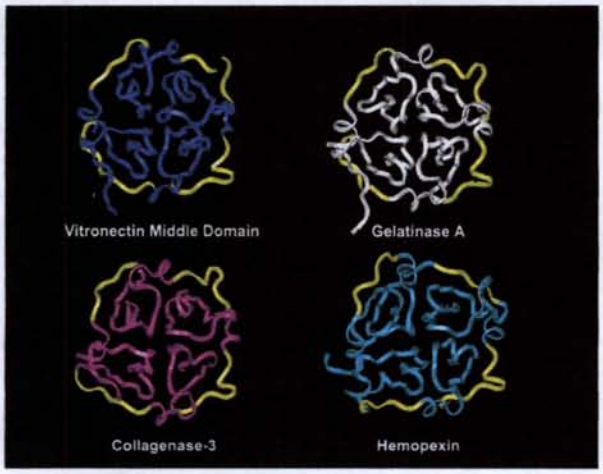

Fig.9. This shows a comparison of the structural homology between the middle domain of vitronectin and gelatinase A, collagenase-3, and hemopexin. The identified edge residues for each structure are marked in yellow.

It has been observed that the proteins on which the structure of vitronectin was based do not undergo *in vivo* polymerization. The structures of each of these proteins were aligned (Fig. 9) based on obvious features and general folding patterns in order to examine the differences between them and gain some insight into the mechanism of polymerization for vitronectin. Although the sequence homology is not obvious (Table 1), structural analysis and individual sequence analysis do yield some patterns of negative design.

Table I. Edge Residues for Vitronectin and Homologous Proteins By Strand

Protein	Upper Left	Lower Left	Upper Right	Lower Right
Vitronectin	GTRQPQ	AVRPGYPKLI	SQEECEGS	GVLDPDYPRN
Gelatinase A	KSVKFG	RDKPMGPL	KKMDPGFPKL	TLERGYPKP
Collagenase-3	NRIVRVM	VDAELFL	HIMDKDYPRL	YDILEGYPKK
Hemopexin	AKNLQPQ	GWHSWP	ATWTEL	GYTLVNGYPKR

Key:
■ = Positive Charge
■ = Negative Charge
■ = β-bulge

For gelatinase A, the structure on which the accepted model for vitronectin has been based, many of the observations remain the same. There are two predominant β-bulges in the upper and lower right strands of the protein. The upper right strand contains four charged residues (lysine, aspartate). The aspartate residue immediately adjacent to the proline bulge would react unfavorably to β-sheet bonding. The lower right strand of gelatinase contains a bulge and three charged residues (arginine, glutamate, lysine). Thus, these two regions exhibit both of the primary negative design features indicated by the Richardson study to disfavor β-sheet polymerization.

In comparison with vitronectin, the upper left strand of gelatinase contains two positively charged residues instead of one. The lower left strand contains three charged residues (arginine, aspartate, lysine) and two prolines. While these observations are inconclusive for a determination about possible polymerization based on negative design, the subtle differences may be enough to inhibit intermolecular β-sheet interactions.

An initial structural analysis of collagenase-3 indicates the same structural barriers observed in vitronectin and gelatinase A. The upper right strand contains a β-bulge that is flanked by two charged residues (arginine, aspartate), and two additional charges (histidine, lysine). This is a classic and predominant example of negative design. The lower right strand has a bulge and four charged residues (aspartate, glutamate, lysine). In this case, it is likely that the

extreme bulge alone is sufficient to break potential β-polymers. The lower left portion of collagenase-3 (although lacking bulges) contains two charged molecules (aspartate, glutamate). Again, these last two observations are inconclusive in terms of negative design, but the structural subtleties (i.e. charge differences, etc.) may prove enough to inhibit further interaction.

Finally, the structural model presented for hemopexin least resembles that of vitronectin and provides the most inconclusive results for polymerization predictions based on negative design. The upper right strand is the only one of the four structures found not to contain a β-bulge. Although there may be some shielding by the loop that overhangs this portion of the molecule, and it contains one charged residue (glutamate), there is not enough data here to support the conclusion that this inhibits β-bonding. The lower right portion of hemopexin contains a predominant β-bulge which likely prevents further β-sheet interaction. The lower left portion of hemopexin consists of a small bulge, and one potentially charged residue (histidine). Although shielding and charged residues contributed by neighboring regions of the molecule may play a role in prevention, there is not enough conclusive evidence to make reliable predictions regarding β-sheet polymerization based on negative design. The upper left portion of hemopexin is more distorted in comparison with the structure of vitronectin, and contains a charged residue (lysine) as well as one proline residue. It is predicted that this proline in conjunction with the charged molecule may introduce enough negative design within this region to inhibit polymerization.

Site Directed Mutagenesis—Based on the predictions made by the analysis of the structural model of the central domain, it was decided that two positively charged lysine residues would be inserted as this was expected to have the least impact on overall protein folding. Furthermore, this type of incorporation has previously been demonstrated to interfere with the

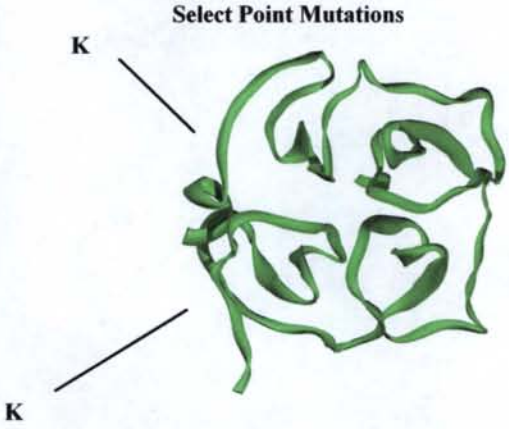

Fig. 10. Shows the location of the inserted lysine residues in terms of the structure of the central β-propeller domain.

formation of intermolecular β-sheet bonds (Wang et al. 2002). The sequences for the upper left strand and lower left strand are – Gly-Thr-Arg-Gln-Pro-Gln- and – Ala-Val-Arg-Pro-Gly-Tyr-Pro-Lys-Ile- respectively. For the upper left strand it was decided to replace glutamine 331 with a lysine. This places the charged residue towards the middle of the strand and avoids replacing existing charges and a proline which would be expected to have a fairly significant impact on protein folding. For the lower left strand, it was decided to replace glycine 191 with a lysine. Likewise, this places the charged residue towards the center of the strand and should have a low impact on overall protein folding. Successful incorporation of these residues was confirmed by sequencing data.

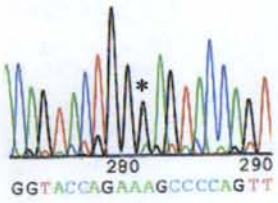

Fig. 11. Sequencing data confirming correct incorporation of primer # 1 for the upper left strand. Mutated residues are marked with asterisks.

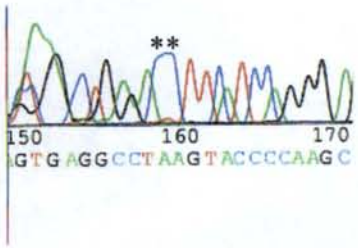

Fig. 12. Sequencing data confirming the correct incorporation of primer #2 for the lower left strand. Mutated residues are marked with asterisks.

SDS-PAGE and Western Blot – Wild Type

Fig. 13 SDS-PAGE and Western Blot performed on wild type vitronectin expressed using the Baculovirus expression system. The band on the left is the protein isolated from the media, the band on the right is the standard indicating a size of about 67kD.

SDS-PAGE and Western Blot - Mutant

Fig. 14. SDS-PAGE and Western Blot performed on mutant vitronectin expressed using the Baculovirus expression system. The band on the left is the protein isolated from the cells, the band on the right is a control.

Protein expression and analysis—Previous studies from this lab have confirmed the production of wild type vitronectin by the Baculovirus expression system and have demonstrated the presence of the protein in the media from which it can be isolated (Gibson et al. 2001). In the first expression experiment, these results were reproduced using the wild type pFastBac expression vector (Fig. 11). The relatively sharp band indicates production of protein around 67kD which is consistent with the expected size for vitronectin. The second experiment confirmed the successful production of the vitronectin mutant protein and demonstrated its presence within the cells (Fig. 12). It appears that the protein is not secreted into the media in large enough quantities to be detected by a Western Blot, but previous experience with this expression system has indicated that this may be a result of a low titer viral infection rather than protein expression errors. Viral amplification experiments are currently underway and it is expected that a higher titer infection will result in protein transport to the media as our previous results have demonstrated.

Summary and Future Direction

The identification and characterization of the edge residues of the central domain of vitronectin were successful and raise some interesting ideas. The primary conclusion to be drawn from the first part of this study is that the two most likely regions for β-sheet polymerization to occur are the upper and lower left strands of vitronectin. Moreover, the structural models show that these edge residues form a band around the outer portion of the molecule that is not inhibited by other regions of the protein. This is encouraging as it further suggests the possibility of β-sheet polymerization occurring at these sites.

The mutagenic studies demonstrate the successful production of the mutant vitronectin protein using the Baculovirus expression system. Confinement of the protein to the cell fractions is most likely a result of a low viral titer infection, however, another possibility to contend with may be protein folding anomalies. Subsequent experiments are being repeated with the primary aim of increasing viral titer in order to analyze the effects of mutation on the folding and expression of vitronectin. There are also many other ongoing efforts in this lab to address the mechanism behind the self-association of vitronectin. Namely, a chimeric protein is being created by exchanging the central domain of vitronectin with its hemopexin and gelatinase counterparts. This will provide more conclusive evidence as to whether or not the self-association of vitronectin is actually mediated by intermolecular β-sheet interactions in the central domain of the protein.

With the information generated by this project, the lab is now poised to directly test the hypothesis that mutations may be used to introduce negative design features that inhibit self-association of the virtonectin protein. This data narrows the possible targets to a select few amino acid residues, and provides several suggestions for future studies. To date, few studies have been

performed to directly show that negative design features may be introduced to disrupt intermolecular associations of proteins through β-sheet polymerization. This work helps to expand the body of knowledge in this area, and serves as a good example of the use of mutagenesis to study the structure/function relationships in protein self-association.

References

Bloemendal, HJ., De Boer, HC., Koop, EA., Van Dongen, AJ., Goldschmeding, R. Landman, WJ., Logtenberg, T., Gebbink, MF., Voest. EE. 2004. Activated vitronectin as a target for anticancer therapy with human antibodies. *Cancer Immunol. Immunother.* 53: 799-808.

Chen, S., Spiegelberg, B. D., Lin, F., Dell, E. J., and Hamm, H. E. 2004. "Interaction of Gβψ with RACK1 and other WD40 repeat proteins." *Journal of Molecular and Cellular Cardiology.* 37: 399-408.

Cherney, R.C., Honan, M.A., Thiagarajan, P. 1993. Site-Directed mutagenesis of the arginine-glycine-aspartic acid in vitronectin abolishes cell adhesion. *J Biol Chem* 268: 9725-9729.

Declerck, P.J., De Mol, M., Alessi, MC., Baudner, D., Paques, EP., Preissner, KT., Muller-Berghaus, G., Collen, D. 1988. Purification and characterization of a plasminogen activator inhibitor 1 binding protein from human plasma. Identification as a multimeric form of S protein (vitronectin). *J Biol Chem* 263: 15454-15461.

Deng, G., Royle, G., Wang, S., Crain, K., Loskutoff, D.J., 1996. Structural and functional analysis of the plasminogen activator inhibitor-1 binding motif in the somatomedin B domain of vitronectin. *J Biol Chem* 271: 12716-12723.

Faber, H. R., Groom, C. R., Baker, H. M., Morgan, W. T., Smith, A., and Baker, E. N. 1995 "1.8 A crystal structure of the C-terminal domain of rabbit serumhaemopexin." *Structure* 3(6), 551-559.

Gibson, AD., Peterson, CB., 2001. Full-length and truncated forms of vitronectin provide insight into effects of proteolytic processing on function. *Biochim Biophys Acta.* 9;1545(1-2):289-304.

Gohlke, U., Gomis-Ruth, F. X., Crabbe, T., Murphy, G., Docherty, A. J. P., and Bode, W.-P. 1996 "The C-terminal (haemopexin-like) domain structure of humangelatinase-A (MMP2): structural implications for its function." *FEBS Lett* 373, 126-130.

Gomis-Ruth, F. X., Gohlke, M., Betz, M., Knauper, V., Murphy, G., Lopez-Otin, C., and Bode, W. 1996 "The helping hand of collagenase-3 (MMP-13): 2.7A crystal structure of its C-terminal haemopexin-like domain." *J. Mol. Biol.* 264, 556-566.

Horn, NA., Hurst, GB. Mayasundari, A., Whittemore, NA., Serpersu, EH., Peterson, CB. 2004. Assignment of the four disulfides in the N-terminal somatomedin B domain of native vitronectin isolated from human plasma. *J Biol Chem* 279: 35867-35878.

Ishikawa-Sakurai, M., Hayashi, M. 1993. Two collagen-binding domains of vitronectin. *Cell Struct Funct* 18: 253-259.

Kirschner, DA., Abraham, C., Selkoe, DJ., 1986. X-ray diffraction from intraneuronal paired helical filaments and extraneuronal amyloid fibers in Alzheimers disease indicates cross-beta formation. *Proc Natl Acad Sci USA.* 83: 503-507.

Liang, OD., Maccarana, M., Flock, JI., Paulsson, M., Preissner, KT., Wadstrom, T. 1993. Multiple interactions between human vitronectin and *Staphylococcus aureus. Biochim Biophys Acta* 1225: 57-63.

Liang, OD., Preissner, KT., Chhatwal, GS. 1997. The hemopexin-type repeats of human vitronectin are recognized by *Streptococcus pyogenes. Biochem Biophys Res Commun.* 234: 445-449.

Mayasundari, A. Whittemore, NA, Serpersu, E. Peterson, CB. 2004. The solution structure of the N-terminal domain of human vitronectin. *J Biol Chem.* 279: 29359-29366.

Minor, KH., Peterson, CB. 2002. Plasminogen activator inhibitor type 1 promotes the self-association of vitroncetin into complexes exhibiting altered incorporation into the extracellular matrix. *J Biol Chem* 277: 10337-10345.

Minor, KH., Schar, CR., Blouse, GE., Shore, JD., Lawrence, DA., Schuck, P., Peterson, CB., 2005. A mechanism for assembly of complexes of vitronectin and plasminogen activator inhibitor-1 from sedimentation velocity analysis. *J Biol Chem* 280: 28711-28720.

Podor, TJ., Shaughnessy, SG., Blackburn, MN., Peterson, CB. 2000. New Insights into the Size and Stoichiometry of the Plasminogen Activator Inhibitor Type-1·Vitronectin Complex. *J Biol Chem* 275: 25402-25410.

Reuning, U., Magdolen, V., Wilhelm, O., Fischer, K., Lutz, V., Graeff, H., Schmitt, M., 1998. Multifunctional potential of the plasminogen activation system in tumor invasion and metastasis. *Int. J. Oncol.* 13: 893-906.

Richardson, JS., Richardson, DC. 2002. Natural β-sheet proteins use negative design to avoid edge-to-Edge aggregation. *PNAS.* 99:2754-2759.

Sieffert, D., Loskutoff, D.J., 1991. Kinetic analysis of the interaction between type 1 plasminogen activator inhibitor and vitronectin and evidence that the bovine inhibitor binds to a thrombin-deprived amino-terminal fragment of bovine vitronectin. *Biochem Biophys Acta* 1078: 28-30.

Springer, T. A. 2002 "Predicted and experimental structures of integrins and β-propellers." *Curr. Opin. Struct. Biol.* 12, 802-813.

Stricker, T. P., Dumin, J. A., Dickeson, S. K., Chung, L., Nagase, H., Parks, W. C., and Santoro, S. A. 2001 "Structural analysis of the α2 integrin I domain/procolloagenase-1-(matrix metalloproteinase-1) interaction." *J. Biol. Chem.* 276, 29375-29381.

Suzuki, S., Pierschbacher, MD., Hayman, EG., Nguyen, K. Ohgren, Y. et al. 1984. Domain
structure of vitronectin. *J Biol Chem* 259: 15307-14.

Wang, W., Hecht, MH., 2002. Rationally designed mutations convert de novo amyloid-like fibrils into monomeric beta-sheet proteins. *Proc Natl Acad Sci U S A*. 99:2760-5.

Xu, D., Baburaj, K., Peterson, CB. 2001. Model for the Three-Dimensional Structure of Vitronectin: Predictions for the Multi-Domain Protein from Threading and Docking. *Proteins: Structure, Function, and Genetics.* 44:312-320.

Zhuang, P. Blackburn, MC., Peterson, CB., 1996. Characterization of the Denaturation and renaturation of Human Plasma Vitronectin. I. Biophysical Characterization of Protein unfolding and Multimerization. *J Biol Chem* 271: 14323-14332.

Kevin C. Walters
Summer Internship Progress Report
Advisor: Dr. Cynthia Peterson
9/01/2005

Introduction

Vitronectin is a multifunctional glycoprotein found in both the circulation and the extracellular matrix (ECM). Through its capacity to interact with a wide variety of ligands it helps to mediate several key physiological processes including coagulation, cell adhesion and migration, tumor metastasis and tissue remodeling, and immune system response. An interesting feature of the protein is its ability to adopt different functional forms presumably as a result of varying physiological conditions. The monomeric form of vitronectin is found in the circulation where it helps to regulate proteolytic cascades. Conversely, a multimeric form of vitronectin is found in the ECM where it helps to regulate pericellular proteolysis as well as cell adhesion and migration. The process by which the monomer assembles into higher order complexes remains relatively uncharacterized, but is believed to be mediated by the binding of vitronectin to plasminogen activator inhibitor type-1 (PAI-1).

Since its discovery in 1967, extensive research has been performed with the primary focus of characterizing the binding sites for various ligands. Although vitronectin has not been successfully crystallized, advances in technologies with biological application have proved useful in studying how the structure of the protein relates to its function. Combined computational analyses and NMR measurements have produced structural models for the three domains of vitronectin. The central domain is of particular interest because it was shown to contain extensive β-sheet content organized into a four bladed propeller-type structure. It is believed that this domain of vitronectin is integral in the formation of higher order complexes through intermolecular propagation of its β-sheets.

In other studies, it has been observed that β-propellers are prominent structures present during the intermolecular associations of proteins. Some well-known examples of this include the WD-40 structures in signal transduction, β-propeller domains in matrix metalloproteinases, and the head regions of integrins that recognize ECM ligands. These examples further suggest the central domain of vitronectin as a mediator of intermolecular associations. The N-terminal and C-terminal domains also have been eliminated as possible candidates for higher order complex formation. The N-terminal somatomedin B (SMB) domain has been isolated and shown to be monomeric and stable under physiological conditions. Also, earlier work with the folding and denaturation of vitronectin has shown that binding of the heparin ligand to the C-terminal domain did not disrupt the formation of higher order complexes.

The structures of several homologous proteins with a four bladed propeller motif have been solved, but these naturally occurring β-sheet proteins typically do not associate into higher-order oligomers. This suggests that in these cases regulatory features must exist which inhibit β-sheet interaction in favor of the monomeric protein. Extensive analysis of β-sheet proteins performed by Richardson et al. has resulted in a set of rules for β-strands that govern the formation of more extensive intra- or intermolecular structures. They suggest that certain features of β edge strands may be responsible for preventing propagation via hydrogen bonding to additional β-strands. This analysis was used as a general guideline to contrast the edge residues in β-propeller structures for vitronectin, hemopexin, and homologues in order to predict the features responsible for the association behavior observed in vitronectin. The goal of this project is to test these predictions via mutagenesis studies in which entire domains are substituted followed by

site directed mutagenesis to further define the specific edge residues involved. This will provide a valuable insight into the mechanistic aspect of the formation of vitronectin complexes. Furthermore, this study serves as an important test of the notion that specific structural features may serve as a "negative design" to inhibit further β-sheet association and distinguish central and peripheral strands in β-propeller structures.

Experimental Outline

For these experiments, a drosophila expression system will be used in lieu of the baculovirus expression system with the hope of generating a greater level of expression than typically observed. In order to create the chimeric or mutated protein, the gene for vitronectin will first be amplified through a polymerase chain reaction (PCR) to produce a high yield of DNA fragments. The general protocol for the PCR reaction is as follows: mixed into a small test tube are 1μl pcDNA4/ssvn vitronectin template, 3μl MgCl buffer (with four different concentrations), 3μl dNTPs, 3μl forward primer, 3μl reverse primer, 1μl of Taq DNA polymerase (diluted 1:4), and 16μl of water. This is then placed into a thermocycler under the following run conditions: 94°C for two minutes, 94°C for thirty seconds, 55°C for thirty seconds, 72°C for thirty seconds, and 72°C for two minutes. The process is allowed to repeat for twenty-five cycles after which time a yield will be determined via gel electrophoresis. After determining which concentration of buffer produced the highest yield of vitronectin gene fragments, they will be ligated into the cloning vector PCR2.1 from Invitrogen's TA cloning kit. For the ligation, three reactions are set up with 1:2, 3:2. 5:2 ratios of PCR product to cloning vector. In addition, 1μl of 10X ligation buffer, 1μL T4 DNA ligase, and 5μl of water are added to each reaction.

They are placed in a 15°C water bath overnight. The ligation products are then transformed into competent DH-5α *E. coli* cells and spread onto plates coated with X-gal and IPTG. The IPTG serves as an inducer of the lac operon and the X-gal helps to indicate colonies that have taken up the PCR gene. The vitronectin inserts into the middle of a gene coding for β-galactosidase which can cleave X-gal to form a blue product. Thus the colonies that have successfully taken up the gene are white while the others are blue. Several white colonies are grown up and the plasmid DNA is purified with the Qiagen miniprep kit. The plasmid is then digested with the BglII and AgeI enzymes under the following conditions: 3μl DNA, 0.5μl BglII, 0.5μL AgeI, 1μl Buffer #2, and 5μl of water. This mixture is incubated at 37°C for one hour after which time the products are separated on an agarose gel and the vitronectin fragment is purified with the Qiagen gel extraction kit. Likewise, the expression vector is also digested and purified under the same conditions. Finally, the two products are ligated together to complete a cloned expression vector. This expression vector will then be used to induce the S2 drosophila cells to produce wild type vitronectin as a test for yield with this particular expression system. Finally, the expression vector can be used as a template to create a chimeric protein via domain swapping with vitronectin homologues and as a template for site directed mutagenesis. The analysis of the oligomerization status of the protein will be performed with a western blot.

Progress towards Research Aims

This work was initiated by comparing the homologous β-propeller domains of vitronectin, hemopexin, collagenase, and gelatinase with a primary focus on differentially

charged edge strands and the presence of β-bulges, two predominant features noted in the Richardson study that may prevent oligomerization. Based on this comparative analysis, work began to create a recombinant expression vector for the drosophila expression system. During this process, however, there were many technical difficulties resulting in changes to the cloning strategy.

First, in order to create the recombinant expression vector, stock vitronectin template and primers were used as described in the experimental method. When this failed to yield usable plasmid DNA, a blunt ligation reaction was attempted. This was performed in the same manner as previously described, but bypassed ligation into the cloning vector PCR2.1. Instead, the PCR products were digested, purified, and inserted directly into the expression vector. Again this failed to produce any usable recombinant plasmid DNA. Following this second failure, a series of control reactions were performed in order to pinpoint the defective step in the cloning process. Initially it was believed that the problematic area was a contaminated reagent. With this in mind, all experiments were repeated with new reagents, paying particular attention to sterile technique and the possibility of cross contamination. Again they failed to create the desired product. Finally, through analysis of restriction digests and sequencing information, it was determined that the source of error was the stock of primers used for the PCR reaction which potentially exhibited weak or non-specific binding and hence prevented the amplification of the desired product. Thus, new primers were designed with the help of the DNAstar computer program. To date, these primers have proved effective and all currently attempted steps have produced successful results.

Future Outline

After overcoming the initial problems with the cloning strategy, the future plan is to continue with the project as outlined in the experimental methods portion of this paper. To date, the vitronectin gene is being ligated into the vector for the drosophila expression system with results expected in a few days. We are also taking advantage of the ability to express vitronectin in a variety of host systems by concurrently using the baculovirus expression system to help ensure the production of a usable vector which can then be mutated as desired. Chimeric proteins containing replacements for the entire β propeller domain will be generated as described and tested for known vitronectin functions including heparin binding, integrin binding, uPAR binding, and PAI-1 binding and stabilization. The role of specific amino acid residues in the oligomerization process will be analyzed through site-directed mutagenesis techniques. Mutations that disfavor the formation of the multimer will be screened for using native PAGE and western blotting with anti-vitronectin antibodies. It is important here to remain cautious and anticipate the problems that may yet occur with this mutagenesis experiment. For one, the replacement of an entire domain of vitronectin may disrupt the normal packing and folding of the protein. Also, these changes may disrupt the secondary PAI-1 binding sites in vitronectin which may be problematic as it is the interaction with PAI-1 which is believed to induce the formation of multimeric vitronectin complexes. Furthermore, the evaluation of the oligomerization status of the protein is likely not to be as straightforward as running a Western blot. These problems, however, will be addressed on a case-by-case basis as the project progresses.

ANALYSIS OF LARGE SOLAR PARTICLE EVENTS WITH EXTRACTION OF DOSES PER ENERGY CONTRIBUTION WITH IMPLICATIONS FOR SPACE RADIATION SHIELDING

ENGINEERING PRACTICE PROJECT #1

Caleb D. Bastian

Submitted 8/5/2005

ABSTRACT

This research uses an upper bound on the radiation doses received by astronauts in space by using the data available of the large Oct 19, 1989 solar particle event. Organ doses and dose equivalents are estimated using BRYNTRN, a space radiation transport code developed at NASA Langley Research Center which transports incident solar protons and their reaction products (protons, neutrons, 2H, 3H, 3He, and 4He) through the various areal densities of aluminum and then through an additional quantity of water[1]. The calculated doses and dose equivalents as a function of water depth, obtained from the assumed input SPE spectrum, are then folded with the body organ self-shielding distributions obtained from the CAM model to yield dose and dose-equivalent estimates for the organs of interest. By using various lower energy cutoffs' in the calculations, organ doses and dose equivalents are extracted and modeled as a function of energy and aluminum density using MATLAB; as a result, skin, eye, and blood forming organ doses and dose equivalents are available for any particular particle energy for a variety of aluminum densities. Additionally, this research determines the minimum aluminum density needed to stay within the confines of the ICRP 60 dose recommendations to be approximately 25 g/cm^2. A large number of figures depicting the doses and dose equivalents as functions of particle energy and aluminum density are included in the appendix.

TABLE OF CONTENTS

1.0 INTRODUCTION

1.1 BACKGROUND

Within the next couple of decades, manned missions to Mars will be undertaken. However, before any foray into space past the moon is undertaken, research must be done that can develop methods of estimating the effects of galactic cosmic rays (GCRs), energetic solar particle events (SPEs), and other radiation phenomena on astronauts and on-board technology.

Chronic exposures to the background galactic cosmic ray (GCR) environment is mainly a matter of concern for stochastic effects, such as the induction of cancer with subsequent mortality in many cases, and late deterministic effects, such as cataracts and possible damage to the central nervous system. The actual risks of cancer induction and mortality for the very important high-energy heavy ion component of the GCR spectrum are essentially unknown, but are the subject of numerous, current radiobiological investigations using laboratory beams and animal and cell culture systems.

The earth's magnestosphere shields earth and spacecraft within it from charged particles; however, once outside of the magnestosphere, SPEs become of concern. Large SPEs, although uncommon, are dangerous to organisms and onboard electronics. Large fluxes of energetic particles, namely protons and alpha particles, often have very high energies and can be extremely detrimental to organisms, spacecraft, and space missions. This research focuses on providing organ doses and dose equivalents from the Oct 19, 1989 SPE as a function of aluminum density and particle energy.

1.2 STATEMENT OF THE PROBLEM

With SPEs, the individual dose contributions of energetic particles of differing energies shielded by various aluminum densities are not easily calculated or known. These values can be extracted and tabulated with varying aluminum thicknesses using the computational code BRYNTRN and the additional codes DOSEFIT and SUMDLOC. Thirteen different aluminum areal densities are considered, each with 20 different water depths. Seventeen different lower energy cutoffs are used on the energy spectrum so that the doses in each of these energy bands can be extracted with sufficient resolution. These results identify the combinations of particle energy and aluminum depths that fall within the ICRP 60 recommended occupational dose limits.

2.0 SPACE RADIATION ENVIRONMENT

2.1 INTRODUCTION

The high-energy particles that permeate space are of acute concern in planning missions pass the Earth's magnetosphere. Solar particle events in particular, are of immense concern due to a periodic occurrence and large range in energy. Particle energies ranging from several MeV to many orders of magnitude in GeV are quite possible. Although particles of extremely high energy are rare, they can penetrate appreciable shielding thickness and have a high linear energy transfer (LET), causing much energy to be imparted in traversing shielding or tissue. This results in undesirable secondary particles and radiation fields which cause additional damage. Because of their energy and violent nature of interaction with matter, solar particle events pose a significant risk to space crews on interplanetary missions.

2.2 SOLAR PARTICLE RADIATION AND SUNSPOT ACTIVITY

During a period of maximum sunspot activity of the sun, particle emissions are marked by large fluxes of energetic ions and increased plasma emissions. During this increased population of energetic ions, human space activity is retarded due to satellite and communication affects when solar plasma interacts with the Earth's magnetosphere and upper atmosphere and the increased risk of tissue damage.[4]

2.3 ENERGETIC SOLAR PARTICLE EVENTS

Solar particle events are characterized using several different terms, chiefly flux, fluence, and spectral hardness. Flux can either be described by integral or differential quantities. Integral flux is the number of particles/cm^2/sr/s above some energy, whereas

differential flux is the number of particles/cm^2/sr/s/MeV^2. Fluence is time-integrated flux and is very useful because it is used to describe the number of particles observed during an event. This characterizes the total energy from the event and is useful in determining dose quantities. Spectral hardness and softness describe the relationship between fluence and energy. A hard spectrum has little decrease in particle population as energy decreases. In soft spectra, fluence drops rapidly as energy energy increases. Essentially, these describe the number of energetic particles in which one is concerned.

2.4 Solar Proton Events

Proton flux and fluence characterize solar proton events. Some correlation between proton event frequencies observed near Earth and solar activity exist, but there is no distinct pattern in proton even occurrence.[4] Stuart and Shea[6] have performed statistical analyses of three recent solar cycles (19, 20, 21) in an effort to determine the frequency of large events. They found that a log-normal distribution characterizes the proton event fluence during periods of maximal solar activity; however, very large SPEs are less frequent than expected using the log-normal model, implying that the presence of an upper bound in frequency.

2.5 Interplanetary Mission Planning

As described earlier, the two principal radiation dose contributors in space are the GCR and SPEs. The GCR spectrum is highest during the solar cycle minimum, as seen in figure 2.5.1

Figure 2.5.1. GCR fluxes for representative ions in solar cycle.

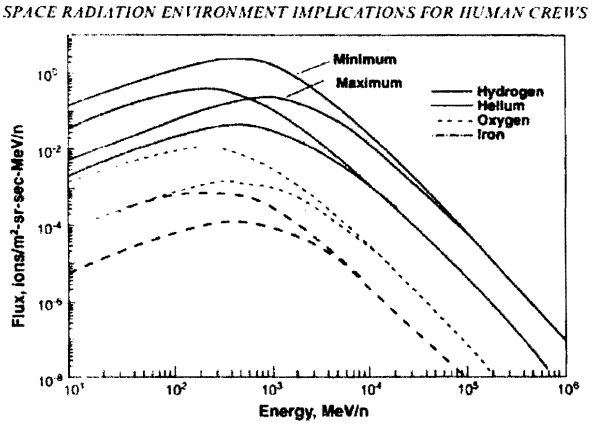

This poses a difficult situation for mission planning due to the contrary behavior of SPEs: Smart and Shea[4] have shown that the probability for a large SPE is highest just before or after the maximum of the solar cycle. Therefore, mission scheduling is unresolved and further research needs to be done in this area. Solar particle events can occur at any time and come in a wide variety of sizes; unfortunately, their sizes usually are not known until they have already terminated. Because of this, models must be built from a worst case scenario.

3.0 SPACE RADIATION TRANSPORT THEORY

3.1 BACKGROUND

Interplanetary magnetic fields caused solar particles to spiral along their trajectory away from the sun such that their path will resemble a braided rope[4]. The spread of the particles is so large that they appear outside the Earth's magnetosphere as an isotropic source incident on the spacecraft. After interaction, the energy of these particles is still so high that they continue in straight-lines; therefore, a straight-line approximation using the 1-D Boltzman equation can be utilized in predicting particle population density.

3.2 HIGH ENERGY APPROXIMATION

BRYNTRN, a deterministic coupled neutron-proton transport computer code characterizes the primary and secondary interactions of solar particles and galactic cosmics rays[3]. It transports incident solar protons and their reaction products (protons, neutrons, 2H, 3H, 3He and 4He) through any shield material and an additional quantity of water. The high-energy nature of the particles allow for a straight-line approximation to be made in the Boltzman transport equation to yield the one-dimensional version for protons and heavior ions[2]:

$$\left[\frac{\partial}{\partial x}-\frac{\partial}{\partial x}S(E)+\sigma_p(E)\right]\phi_p(x,E)=\sum_j\int_E^\infty f_{pj}(E,E')\phi_j(x,E')dE'. \qquad \textbf{(1)}$$

The charged particle term (Coulomb repulsion) is absent for the neutron analog[2]

$$\left[\frac{\partial}{\partial x}+\sigma_n(E)\right]\phi_n(x,E)=\sum_j\int_E^\infty f_{nj}(E,E')\phi_j(x,E')dE'. \qquad \textbf{(2)}$$

$f_{pj}(E,E')$ is the differential cross section for elastic and inelastic collision processes .

$\phi_j(x,E')$ is the flux of I type ions moving in the direction x with energy E' (MeV).

$\sigma_p(E)$ is the macroscopic absorption cross section (cm^{-1}). The $\frac{\partial S(E)\phi_p}{\partial x}$ is the Coulomb interaction term and $\frac{\partial \phi}{\partial x}$ represents the net transfer of particles into and out of the material. $\sigma_p(E)\phi_p(x,E)$ is the nuclear attenuation term. In comparison to exact analytical benchmarks solutions for continuous space proton input spectrum, BRYNTRN has been verified to within 1 percent accuracy[3].

3.3 DOSE/DOSE EQUIVALENT CALCULATIONS

Doses are calculated using

$$D_i(x,>E) = A_i \int_E^{\infty} S_i(E')\phi_i(x,E')dE' \qquad (3)$$

This provides the dose at some distance x from particles whose energy is greater than ER. A_i is the atomic mass number of the colliding nuclei. S(E) is the collisional stopping power

$$S(E) = \frac{4\pi N Z_p^2 Z_t e^4}{mv^2}\left\{\ln\left|\frac{2mv^2}{(1-\beta^2)I_t}\right| - \beta^2 - \frac{C}{Z_t}\right\} \qquad (4)$$

where Z_p is the charge of the particle, N the density of the target molecules, Z_t the number of electrons per target molecule, m the mass of an electron, v the velocity of the particle, β the ratio of the velocity to the speed of light, I_t the mean excitation energy, and C a velocity-dependent shell correction term[3]. Using the quality factor Q, the dose equivalent can be calculated using the following equation:

$$H_i(x,>E) = A_i \int_E^{\infty} Q_i(E')S_i(E')\phi_i(x,E')dE' \quad \textbf{(5)}$$

For nuclear recoils produced by incident protons and for target fragments, dose and dose equivalents are given by the following equations:

$$D_p{}^*(x,>E) = \sum_j \int_E^{\infty} \overline{E}_j{}'\sigma_{jp}(E')\phi_p(x,E')dE' \quad \textbf{(6)}$$

and

$$H_p{}^*(x,>E) = \sum_j \int_E^{\infty} \overline{E}_j{}'Q_{Fj}(E')\sigma_{jp}(E')\phi_p(x,E')dE' \quad \textbf{(7)}$$

where $\overline{E}_j$ is the average recoil energy of the jth-fragment[2]. For transported neutrons, all dose and dose equivalent contributions result from target nuclei recoils or fragments and are computed using identical equations[3].

4.0 BRYNTRN

4.1 BACKGROUND

BRYNTRN was developed at the NASA Langley Research Center for the purpose of estimating crew dose/dose equivalents from exposure to the space environment. It calculates these using a converging, marching algorithm representing solutions to the 1-D Boltzman transport equation[1]. It uses a mesh point grid of 70 energy points logarithmically distributed so that lower energy particles are more represented that higher-energy. Lower bound energy cutoffs had to be carefully selected so that they did not lie between the same mesh points. Because of the straight-ahead approximation introduced in solving the Boltzman transport equation, BRYNTRN's result compare well to advanced three dimensional transport codes and requires much less computational time.

4.2 IMPLEMENTATION

BRYTRN must be compiled and linked before it can be run. When run, it displays a prompt screen asking for the type of simulation (Solar Particle Event), number of aluminum depths, number of water depths, etc. It's results are outputted to a specified file. The names of these files contained the parameters used in the simulation so that upon inspection of the filename, the user knows the data contained within. BRYTRN is followed by DOSEFIT, an intermediate program that takes the BRYNTRN output and uses aluminum shield files to change the data to a form as a function of water depth and aluminum depth. For every BRYNTRN output, DOSEFIT was run for all the different aluminum shield thicknesses. SUMDLOC then converted these outputs using organ self-

shielding distributions into the dose and dose equivalent quantities displayed in the tables and figures in the results and appendices. The organs of interest are the skin, eyes, and blood forming organs.

5.0 DATA ANALYSIS

In this research, 13 different aluminum areal densities are considered, each with 20 different water depths. Most importantly, 17 different lower energy cutoffs are used on the energy spectrum so that the doses in each of these energy bands can effectively be extracted. The maximum energy used in the spectra is 2500 MeV. The cutoffs are at 0, 10, 20, 30, 40, 50, 60, 70, 80, 90, 100, 110, 120, 140, 160, 180, and 200 MeV. The aluminum densities used are 1, 2, 3, 5, 7, 10, 15, 20, 25, 35, 50, 65, and 85 g/cm^2. The water depths used for each of the aluminum densities are 0, 1, 2, 3, 5, 7, 10, 15, 20, 30, 40, 50, 65, 85, 100, 115, 130, 145, 160, and 175 g. Lastly, each of these water depths are folded into the skin, eye, and blood forming organ self-shielding distributions to yield doses, dose equivalents, and quality factors for the said organs.

It is important to note that the values calculated are from the 1989 large solar particle event in October 19-29. These serve as a worst-case scenario involving a solar particle event developing and exposing deep-space crew members to radiation.

In a BRYTRN calculation, for a particular aluminum density and water depth, the total dose can be symbolically shown as a function of energy in $D_{total}(E) = \int_{E_n}^{2500} f(E)dE$, where E_n is the energy cutoff selected; however, the total dose over a particular range is not the information sought. The dose contributions between the different energy cutoffs is the data valued because it details from which energies the doses originate; therefore, a simple change in the integrand will yield the desired technique to extract the dose information.

For $E_n < E_{n+1}$, $\int_0^{E_n} f(E)dE = \int_0^{2500} f(E)dE - \int_{E_n}^{2500} f(E)dE$.

Similarly, $\int_0^{E_{n+1}} f(E)dE = \int_0^{2500} f(E)dE - \int_{E_{n+1}}^{2500} f(E)dE$. Therefore,

$$\int_{E_n}^{E_{n+1}} f(E)dE = \int_0^{E_{n+1}} f(E)dE - \int_0^{E_n} f(E)dE.$$

Substituting in, $\int_{E_n}^{E_{n+1}} f(E)dE = \int_0^{2500} f(E)dE - \int_{E_{n+1}}^{2500} f(E)dE - \left(\int_0^{2500} f(E)dE - \int_{E_{n1}}^{2500} f(E)dE \right)$. This yields $\int_{E_n}^{E_{n+1}} f(E)dE = \int_{E_{n1}}^{2500} f(E)dE - \int_{E_{n+1}}^{2500} f(E)dE$.

Quality factors are determined using a simple linear interpolation between the successive energies for a particular aluminum density. For example, the quality factors from 0 < E < 2500 and 10 < E < 2500 MeV are averaged due to their close proximity in energy. The quality factor calculated from BRYTRN is the quality factor over the energy range of the calculation; as a result, a simple average can be performed because the energy intervals averaged over are very small compared to the energy range of 2500 MeV.

The result of BRYTRN is particle flux, dose, and dose equivalents for each of the aluminum densities, each with twenty different water depths. A code called DOSEFIT takes this output from BRYTRN and the parameters used to run it (number of aluminum and water depths) and generates data files containing dose and dose equivalents as a function of water depth using different aluminum density data input files. These files contain the data on the individual aluminum densities and the water surrogate. Lastly, a

program, SUMDLOC, developed at NASA Langley, folds the outputs into the organs of interest using the skin, eye, and blood forming organ self-shielding distributions obtained from the computerized anatomical man (CAM).

5.1 SKIN DATA ANALYSIS

In Tables 1 and 2, the highest absorbed dose occurs when aluminum shielding is minimal, 1 g/cm^2. For 1 g/cm^2, 43.2 % of the total dose in the SPE energy range to 2500 MeV occurs in energies 20 <E < 30 MeV. This means that for skin, the energies that contribute most to absorbed dose are those 20 < E < 30. In energies 0 < E < 20, there is zero absorbed dose, indicating that these particles are of no concern and should be disregarded in designing shielding systems. The next energy ranges, from 20 < E < 60 MeV, contribute heavily to the absorbed dose. As expected, when aluminum density increases, the absorbed dose decreases. For each successive aluminum density, the maximum energy contributions move down the energy range. For example, with a aluminum density of 5 g/cm^2, the largest energy contributor is 60 < E < 70 MeV, illustrating that higher energy particles will penetrate further in shielding materials than lower energy particles. Tables 3 and 4 show the percentage contribution of a particular energy range to that particular density's total absorbed dose. The data shows that particles with energies from 20 to 90 MeV are the main contributors to absorbed dose. Similar tables for dose equivalent (cSv) and quality factor are located in the appendices.

Beginning with an aluminum density of 20 g/cm^2, the total dose falls to 12.15 cGy.(or 121.5 mGy) With this density, the largest dose contributor is 120 < E < 140 MeV, with a dose of 4.45 cGy.

The ICRP 60 occupational dose limits specify that an individual receive no more than 150 mSv to the lens of the eye or 500 mSv to the skin, hands, and feet. Table 13, the skin dose equivalents, shows the dose equivalent using an aluminum density of 15 g/cm^2 to be 329.7 mSv. This is the minimum aluminum density that meets the ICRP 60 specification for skin, hands, and feet. Therefore, this research recommends that aluminum have an areal density of at least 15 g/cm^2 to meet ICRP requirements; however, these occupational exposures could be modified for astronauts and other special science personnel.

5.1.1 SKIN ABSORBED DOSE TABLES

Table 1. Skin absorbed dose (cGy) per energy range per aluminum density through 15 g/cm^2

Skin dose (cGy)	Aluminum Densities						
Energy range (MeV)	**1 g/cm^2**	**2 g/cm^2**	**3 g/cm^2**	**5 g/cm^2**	**7 g/cm^2**	**10 g/cm^2**	**15 g/cm^2**
0 < E < 10	0.0000	0.0000	-0.0044	0.0000	-0.0005	0.0000	0.0000
10 < E < 20	0.0000	0.0003	0.0001	0.0004	0.0009	0.0004	0.0003
20 < E < 30	334.4500	0.0037	0.0034	0.0044	0.0034	0.0034	0.0028
30 < E < 40	187.0600	115.1000	0.0107	0.0102	0.0094	0.0080	0.0066
40 < E < 50	105.4500	127.2500	89.7270	0.0177	0.0166	0.0151	0.0123
50 < E < 60	57.7890	57.3920	67.7710	26.3000	0.0728	0.0230	0.0189
60 < E < 70	29.3580	32.4200	35.1690	50.4810	23.4610	0.1667	0.0248
70 < E < 80	11.3950	10.7650	10.6480	12.1550	16.2660	2.7337	0.0159
80 < E < 90	17.0700	15.9540	15.6850	15.7210	17.1850	20.3630	10.0580
90 < E < 100	7.3892	6.2882	5.7755	5.3851	5.3328	5.7283	0.1108
100 < E < 110	5.9481	5.5972	5.2644	4.5622	4.1858	4.1118	0.8794
110 < E < 120	4.6441	4.2336	4.0213	3.9335	3.6226	3.2078	2.7536
120 < E < 140	6.8053	6.2886	5.8578	5.3606	5.1474	4.8408	4.4457
140 < E < 160	2.3035	2.1838	2.0736	1.8974	1.7863	1.6617	1.3898
160 < E < 180	1.7234	1.6272	1.5417	1.4159	1.3489	1.2810	1.0811
180 < E < 200	2.2531	2.1492	2.0486	1.8711	1.7380	1.6167	1.3878
Sum	773.6387	387.2528	245.5927	129.1155	80.1764	45.7614	22.1876

Table 2. Skin absorbed dose (cGy) per energy range per aluminum density through 85 g/cm^2

Skin dose (cGy)	Aluminum Densities					
Energy range (MeV)	**20 g/cm^2**	**25 g/cm^2**	**35 g/cm^2**	**50 g/cm^2**	**65 g/cm^2**	**85 g/cm^2**
0 < E < 10	0.0000	0.0000	0.0000	0.0000	0.0000	0.0000
10 < E < 20	0.0002	0.0002	0.0001	0.0001	0.0000	0.0000
20 < E < 30	0.0022	0.0017	0.0012	0.0006	0.0005	0.0002
30 < E < 40	0.0054	0.0044	0.0030	0.0016	0.0012	0.0006
40 < E < 50	0.0102	0.0084	0.0057	0.0032	0.0022	0.0011
50 < E < 60	0.0156	0.0130	0.0089	0.0051	0.0035	0.0018
60 < E < 70	0.0208	0.0173	0.0121	0.0071	0.0049	0.0026
70 < E < 80	0.0125	0.0105	0.0075	0.0045	0.0031	0.0017
80 < E < 90	0.0342	0.0255	0.0185	0.0115	0.0080	0.0045
90 < E < 100	0.1108	0.0161	0.0110	0.0071	0.0050	0.0029
100 < E < 110	0.8794	0.0421	0.0122	0.0079	0.0056	0.0033
110 < E < 120	2.7536	0.2957	0.0139	0.0088	0.0063	0.0038
120 < E < 140	4.4457	3.1315	0.1475	0.0202	0.0146	0.0089
140 < E < 160	1.3898	1.3220	0.5179	0.0136	0.0098	0.0061
160 < E < 180	1.0811	0.9920	0.8524	0.0374	0.0271	0.0176
180 < E < 200	1.3878	1.2971	1.1316	0.4592	0.3612	0.2626
Sum	12.1493	7.1776	2.7435	0.5879	0.4532	0.3176

Table 3. Skin dose percentage contribution per energy range per aluminum density through 15 g/cm^2

Skin dose percentage	**Aluminum Densities**						
Energy range (MeV)	**1 g/cm^2**	**2 g/cm^2**	**3 g/cm^2**	**5 g/cm^2**	**7 g/cm^2**	**10 g/cm^2**	**15 g/cm^2**
0 < E < 10	0.0%	0.0%	0.0%	0.0%	0.0%	0.0%	0.0%
10 < E < 20	0.0%	0.0%	0.0%	0.0%	0.0%	0.0%	0.0%
20 < E < 30	43.2%	0.0%	0.0%	0.0%	0.0%	0.0%	0.0%
30 < E < 40	24.2%	29.7%	0.0%	0.0%	0.0%	0.0%	0.0%
40 < E < 50	13.6%	32.9%	36.5%	0.0%	0.0%	0.0%	0.1%
50 < E < 60	7.5%	14.8%	27.6%	20.4%	0.1%	0.1%	0.1%
60 < E < 70	3.8%	8.4%	14.3%	39.1%	29.3%	0.4%	0.1%
70 < E < 80	1.5%	2.8%	4.3%	9.4%	20.3%	6.0%	0.1%
80 < E < 90	2.2%	4.1%	6.4%	12.2%	21.4%	44.5%	45.3%
90 < E < 100	1.0%	1.6%	2.4%	4.2%	6.7%	12.5%	0.5%
100 < E < 110	0.8%	1.4%	2.1%	3.5%	5.2%	9.0%	4.0%
110 < E < 120	0.6%	1.1%	1.6%	3.0%	4.5%	7.0%	12.4%
120 < E < 140	0.9%	1.6%	2.4%	4.2%	6.4%	10.6%	20.0%
140 < E < 160	0.3%	0.6%	0.8%	1.5%	2.2%	3.6%	6.3%
160 < E < 180	0.2%	0.4%	0.6%	1.1%	1.7%	2.8%	4.9%
180 < E < 200	0.3%	0.6%	0.8%	1.4%	2.2%	3.5%	6.3%

Table 4. Skin dose percentage contribution per energy range per aluminum density through 85 g/cm^2

Skin dose percentage	**Aluminum Densities**					
Energy range (MeV)	**20 g/cm^2**	**25 g/cm^2**	**35 g/cm^2**	**50 g/cm^2**	**65 g/cm^2**	**85 g/cm^2**
0 < E < 10	0.0%	0.0%	0.0%	0.0%	0.0%	0.0%
10 < E < 20	0.0%	0.0%	0.0%	0.0%	0.0%	0.0%
20 < E < 30	0.0%	0.0%	0.0%	0.1%	0.1%	0.1%
30 < E < 40	0.0%	0.1%	0.1%	0.3%	0.3%	0.2%
40 < E < 50	0.1%	0.1%	0.2%	0.5%	0.5%	0.3%
50 < E < 60	0.1%	0.2%	0.3%	0.9%	0.8%	0.6%
60 < E < 70	0.2%	0.2%	0.4%	1.2%	1.1%	0.8%
70 < E < 80	0.1%	0.1%	0.3%	0.8%	0.7%	0.5%
80 < E < 90	0.3%	0.4%	0.7%	2.0%	1.8%	1.4%
90 < E < 100	0.9%	0.2%	0.4%	1.2%	1.1%	0.9%
100 < E < 110	7.2%	0.6%	0.4%	1.3%	1.2%	1.0%
110 < E < 120	22.7%	4.1%	0.5%	1.5%	1.4%	1.2%
120 < E < 140	36.6%	43.6%	5.4%	3.4%	3.2%	2.8%
140 < E < 160	11.4%	18.4%	18.9%	2.3%	2.2%	1.9%
160 < E < 180	8.9%	13.8%	31.1%	6.4%	6.0%	5.5%
180 < E < 200	11.4%	18.1%	41.2%	78.1%	79.7%	82.7%

5.2 EYE DATA ANALYSIS

The eye data shows that the primary dose contributors for low aluminum density thicknesses are in the energies $20 < E < 80$ MeV, with the majority from $20 < E < 50$ MeV. At an aluminum density of 20 g/cm^2, the largest energy contributors are at higher energies, $120 < E < 140$ MeV, representing 40.7% of a total absorbed dose of 12.01 cGy.

Using the dose equivalent data from the appendices, Table 18 shows the minimum aluminum density required to meet the eye requirement is 25 g/cm^2. This results in a 108.0 mSv dose equivalent. The largest energy contributor to this dose is the $120 < E < 140$ energy band, constituting 39.5% of the dose.

5.2.1 EYE ABSORBED DOSE TABLES

Table 5. Eye absorbed dose (cGy) per energy range per aluminum density through 15 g/cm^2

Eye dose (cGy)	Aluminum Densities						
Energy range (MeV)	**1 g/cm^2**	**2 g/cm^2**	**3 g/cm^2**	**5 g/cm^2**	**7 g/cm^2**	**10 g/cm^2**	**15 g/cm^2**
0 < E < 10	0.0000	0.0000	0.0000	0.0000	0.0014	0.0000	0.0000
10 < E < 20	0.0002	0.0001	0.0001	0.0002	-0.0005	0.0002	0.0001
20 < E < 30	100.9200	0.0026	0.0047	0.0038	0.0034	0.0034	0.0027
30 < E < 40	62.3110	34.7420	0.0120	0.0113	0.0106	-0.0173	0.0077
40 < E < 50	182.3200	87.5770	27.0920	0.0228	0.0203	0.0449	0.0152
50 < E < 60	60.9840	74.8840	76.4250	8.3877	0.0465	0.0286	0.0234
60 < E < 70	37.1310	38.5120	39.8540	47.8070	10.1310	0.0863	0.0304
70 < E < 80	12.8190	12.6720	13.0140	13.6770	18.2850	1.1767	0.0184
80 < E < 90	18.6730	17.9800	17.7440	18.4560	20.3720	17.4170	9.6162
90 < E < 100	6.9533	6.4465	6.2387	6.0497	6.0333	6.7103	0.0740
100 < E < 110	5.5312	5.3095	5.1321	4.7738	4.6362	4.6807	0.5870
110 < E < 120	4.6311	4.2063	3.9976	3.8464	3.6717	3.5148	2.2985
120 < E < 140	7.0226	6.5373	6.1535	5.6388	5.2939	4.9245	4.8909
140 < E < 160	2.3553	2.2428	2.1455	2.0033	1.9085	1.7806	1.4574
160 < E < 180	1.7207	1.6330	1.5589	1.4607	1.4151	1.3593	1.1201
180 < E < 200	2.2177	2.1095	2.0100	1.8458	1.7350	1.6424	1.4677
Sum	505.5901	294.8546	201.3821	113.9843	73.5633	43.3524	21.6096

Table 6. Eye absorbed dose (cGy) per energy range per aluminum density through 85 g/cm^2

Eye dose (cGy)	Aluminum Densities					
Energy range (MeV)	**20 g/cm^2**	**25 g/cm^2**	**35 g/cm^2**	**50 g/cm^2**	**65 g/cm^2**	**85 g/cm^2**
0 < E < 10	0.0000	0.0000	0.0000	0.0000	0.0000	0.0000
10 < E < 20	0.0002	0.0001	0.0001	0.0000	0.0000	0.0000
20 < E < 30	0.0022	0.0017	0.0011	0.0006	0.0004	0.0002
30 < E < 40	0.0063	0.0051	0.0035	0.0019	0.0011	0.0005
40 < E < 50	0.0124	0.0103	0.0069	0.0039	0.0022	0.0010
50 < E < 60	0.0195	0.0161	0.0111	0.0063	0.0036	0.0017
60 < E < 70	0.0254	0.0212	0.0149	0.0087	0.0051	0.0025
70 < E < 80	0.0152	0.0128	0.0091	0.0055	0.0033	0.0016
80 < E < 90	0.0379	0.0304	0.0221	0.0137	0.0084	0.0044
90 < E < 100	0.0740	0.0182	0.0130	0.0082	0.0052	0.0028
100 < E < 110	0.5870	0.0350	0.0141	0.0092	0.0059	0.0033
110 < E < 120	2.2985	0.2118	0.0157	0.0101	0.0066	0.0037
120 < E < 140	4.8909	2.9237	0.1241	0.0228	0.0152	0.0089
140 < E < 160	1.4574	1.4704	0.4524	0.0144	0.0098	0.0059
160 < E < 180	1.1201	1.0410	0.8658	0.0346	0.0243	0.0156
180 < E < 200	1.4677	1.3653	1.2072	0.4476	0.3473	0.2528
Sum	12.0146	7.1632	2.7608	0.5874	0.4385	0.3050

Table 7. Eye absorbed dose contribution percentage per energy range per aluminum density through 15 g/cm^2

Eye Dose percentage	Aluminum Densities						
Energy range (MeV)	1 g/cm^2	2 g/cm^2	3 g/cm^2	5 g/cm^2	7 g/cm^2	10 g/cm^2	15 g/cm^2
0 < E < 10	0.0%	0.0%	0.0%	0.0%	0.0%	0.0%	0.0%
10 < E < 20	0.0%	0.0%	0.0%	0.0%	0.0%	0.0%	0.0%
20 < E < 30	20.0%	0.0%	0.0%	0.0%	0.0%	0.0%	0.0%
30 < E < 40	12.3%	11.8%	0.0%	0.0%	0.0%	0.0%	0.0%
40 < E < 50	36.1%	29.7%	13.5%	0.0%	0.0%	0.1%	0.1%
50 < E < 60	12.1%	25.4%	38.0%	7.4%	0.1%	0.1%	0.1%
60 < E < 70	7.3%	13.1%	19.8%	41.9%	13.8%	0.2%	0.1%
70 < E < 80	2.5%	4.3%	6.5%	12.0%	24.9%	2.7%	0.1%
80 < E < 90	3.7%	6.1%	8.8%	16.2%	27.7%	40.2%	44.5%
90 < E < 100	1.4%	2.2%	3.1%	5.3%	8.2%	15.5%	0.3%
100 < E < 110	1.1%	1.8%	2.5%	4.2%	6.3%	10.8%	2.7%
110 < E < 120	0.9%	1.4%	2.0%	3.4%	5.0%	8.1%	10.6%
120 < E < 140	1.4%	2.2%	3.1%	4.9%	7.2%	11.4%	22.6%
140 < E < 160	0.5%	0.8%	1.1%	1.8%	2.6%	4.1%	6.7%
160 < E < 180	0.3%	0.6%	0.8%	1.3%	1.9%	3.1%	5.2%
180 < E < 200	0.4%	0.7%	1.0%	1.6%	2.4%	3.8%	6.8%

Table 8. Eye absorbed dose contribution percentage per energy range per aluminum density through 85 g/cm^2

Eye dose percentage	Aluminum Densities					
Energy range (MeV)	20 g/cm^2	25 g/cm^2	35 g/cm^2	50 g/cm^2	65 g/cm^2	85 g/cm^2
0 < E < 10	0.0%	0.0%	0.0%	0.0%	0.0%	0.0%
10 < E < 20	0.0%	0.0%	0.0%	0.0%	0.0%	0.0%
20 < E < 30	0.0%	0.0%	0.0%	0.1%	0.1%	0.1%
30 < E < 40	0.1%	0.1%	0.1%	0.3%	0.2%	0.2%
40 < E < 50	0.1%	0.1%	0.3%	0.7%	0.5%	0.3%
50 < E < 60	0.2%	0.2%	0.4%	1.1%	0.8%	0.5%
60 < E < 70	0.2%	0.3%	0.5%	1.5%	1.2%	0.8%
70 < E < 80	0.1%	0.2%	0.3%	0.9%	0.8%	0.5%
80 < E < 90	0.3%	0.4%	0.8%	2.3%	1.9%	1.4%
90 < E < 100	0.6%	0.3%	0.5%	1.4%	1.2%	0.9%
100 < E < 110	4.9%	0.5%	0.5%	1.6%	1.3%	1.1%
110 < E < 120	19.1%	3.0%	0.6%	1.7%	1.5%	1.2%
120 < E < 140	40.7%	40.8%	4.5%	3.9%	3.5%	2.9%
140 < E < 160	12.1%	20.5%	16.4%	2.5%	2.2%	1.9%
160 < E < 180	9.3%	14.5%	31.4%	5.9%	5.5%	5.1%
180 < E < 200	12.2%	19.1%	43.7%	76.2%	79.2%	82.9%

5.3 BLOOD-FORMING ORGANS DATA ANALYSIS

The data shows that blood forming organs are more susceptible to higher energy particles than either the skin or eyes. At low aluminum densities, energies from 80 MeV to 120 MeV are important contributors to dose. Again, consistently, the 120 to 140 MeV energy range is responsible for most of the absorbed dose for the different aluminum densities. Using an aluminum density of 15 g/cm^2 greatly reduces the dose received from 46.3 cGy using 1 g/cm^2 to 7.4 cGy. All the energies below 120 MeV become small contributors, with the primary dose coming energies between 120 and 160 MeV.

The ICRP 60 report recommends no more than 500 mSv per year for blood forming organs. Table 21 shows that an aluminum density of 3 g/cm^2 meets this requirement, resulting in a dose equivalent of 452.7 mSv. At this aluminum density, the there are two peaks in the energy contributions: at $80 < E < 90$ MeV, comprising 20.8% of the dose equivalent (93.9 mSv) and at $120 < E < 140$ MeV, 15.8% of the dose equivalent (71.3 mSv).

5.3.1 BLOOD FORMING ORGANS ABSORBED DOSE TABLES

Table 9. Blood forming organs absorbed dose (cGy) per energy range per aluminum density through 15 g/cm^2

BFO dose (cGy)	Aluminum Densities						
Energy range (MeV)	1 g/cm^2	2 g/cm^2	3 g/cm^2	5 g/cm^2	7 g/cm^2	10 g/cm^2	15 g/cm^2
0 < E < 10	0.0000	0.0000	0.0000	0.0000	0.0000	0.0000	0.0000
10 < E < 20	0.0002	0.0002	0.0001	0.0002	0.0002	0.0001	0.0001
20 < E < 30	0.1455	0.0024	0.0023	0.0021	0.0018	0.0017	0.0014
30 < E < 40	0.0532	-0.0434	0.0072	0.0067	0.0062	0.0055	0.0045
40 < E < 50	0.5326	0.1436	0.0244	0.0141	0.0131	0.0116	0.0095
50 < E < 60	3.3653	0.6469	0.2352	0.0129	0.0213	0.0191	0.0158
60 < E < 70	5.5833	4.5573	2.6329	0.2955	0.0339	0.0257	0.0215
70 < E < 80	4.7360	3.2265	2.0810	1.0661	0.1488	0.0167	0.0133
80 < E < 90	8.8777	7.8593	6.7059	4.1894	2.1154	0.3457	0.0348
90 < E < 100	5.0096	4.0973	3.5231	2.7724	2.0148	0.8919	0.0523
100 < E < 110	4.0777	4.1469	3.9185	2.9787	2.3074	1.4346	0.2512
110 < E < 120	3.5351	3.2303	3.0843	3.0027	2.5577	1.7755	0.6939
120 < E < 140	5.8452	5.6420	5.3876	4.8420	4.4201	3.7546	2.4045
140 < E < 160	1.9094	1.9214	1.9219	1.8728	1.7881	1.6323	1.2911
160 < E < 180	1.3302	1.3122	1.3026	1.3050	1.3163	1.2941	1.1516
180 < E < 200	1.6816	1.6495	1.6204	1.5704	1.5312	1.4963	1.4636
Sum	46.2851	38.3924	32.3986	23.9311	18.2763	12.7052	7.4091

Table 10. Blood forming organs absorbed dose (cGy) per energy range per aluminum density through 85 g/cm^2

BFO dose (cGy)	Aluminum Densities					
Energy range (MeV)	20 g/cm^2	25 g/cm^2	35 g/cm^2	50 g/cm^2	65 g/cm^2	85 g/cm^2
0 < E < 10	0.0000	0.0000	0.0000	0.0000	0.0000	0.0000
10 < E < 20	0.0001	0.0000	0.0000	0.0000	0.0000	0.0000
20 < E < 30	0.0011	0.0009	0.0006	0.0003	0.0002	0.0001
30 < E < 40	0.0037	0.0030	0.0020	0.0011	0.0006	0.0002
40 < E < 50	0.0079	0.0065	0.0044	0.0024	0.0013	0.0006
50 < E < 60	0.0130	0.0108	0.0074	0.0042	0.0023	0.0010
60 < E < 70	0.0180	0.0151	0.0105	0.0062	0.0034	0.0016
70 < E < 80	0.0112	0.0095	0.0068	0.0041	0.0023	0.0011
80 < E < 90	0.0279	0.0238	0.0173	0.0108	0.0064	0.0032
90 < E < 100	0.0171	0.0143	0.0106	0.0068	0.0041	0.0022
100 < E < 110	0.0264	0.0160	0.0119	0.0078	0.0048	0.0026
110 < E < 120	0.0968	0.0212	0.0131	0.0087	0.0055	0.0030
120 < E < 140	1.0557	0.2789	0.0332	0.0202	0.0130	0.0074
140 < E < 160	0.9257	0.4989	0.0473	0.0114	0.0075	0.0044
160 < E < 180	0.9321	0.6789	0.1590	0.0136	0.0092	0.0056
180 < E < 200	1.3852	1.2254	0.7115	0.1034	0.0784	0.0562
Sum	4.5219	2.8032	1.0357	0.2012	0.1390	0.0891

Table 11. Blood forming organs absorbed dose contribution percentage per energy range per aluminum density through 15 g/cm^2

BFO dose percentage	Aluminum Densities						
Energy range (MeV)	1 g/cm^2	2 g/cm^2	3 g/cm^2	5 g/cm^2	7 g/cm^2	10 g/cm^2	15 g/cm^2
0 < E < 10	0.0%	0.0%	0.0%	0.0%	0.0%	0.0%	0.0%
10 < E < 20	0.0%	0.0%	0.0%	0.0%	0.0%	0.0%	0.0%
20 < E < 30	0.3%	0.0%	0.0%	0.0%	0.0%	0.0%	0.0%
30 < E < 40	0.1%	0.1%	0.0%	0.0%	0.0%	0.0%	0.1%
40 < E < 50	1.2%	0.4%	0.1%	0.1%	0.1%	0.1%	0.1%
50 < E < 60	7.3%	1.7%	0.7%	0.1%	0.1%	0.1%	0.2%
60 < E < 70	12.1%	11.9%	8.1%	1.2%	0.2%	0.2%	0.3%
70 < E < 80	10.2%	8.4%	6.4%	4.5%	0.8%	0.1%	0.2%
80 < E < 90	19.2%	20.5%	20.7%	17.5%	11.6%	2.7%	0.5%
90 < E < 100	10.8%	10.7%	10.9%	11.6%	11.0%	7.0%	0.7%
100 < E < 110	8.8%	10.8%	12.1%	12.4%	12.6%	11.3%	3.4%
110 < E < 120	7.6%	8.4%	9.5%	12.5%	14.0%	14.0%	9.4%
120 < E < 140	12.6%	14.7%	16.6%	20.2%	24.2%	29.6%	32.5%
140 < E < 160	4.1%	5.0%	5.9%	7.8%	9.8%	12.8%	17.4%
160 < E < 180	2.9%	3.4%	4.0%	5.5%	7.2%	10.2%	15.5%
180 < E < 200	3.6%	4.3%	5.0%	6.6%	8.4%	11.8%	19.8%

Table 12. Blood forming organs absorbed dose contribution percentage per energy range per aluminum density through 85 g/cm^2

BFO dose percentage	Aluminum Densities					
Energy range (MeV)	20 g/cm^2	25 g/cm^2	35 g/cm^2	50 g/cm^2	65 g/cm^2	85 g/cm^2
0 < E < 10	0.0%	0.0%	0.0%	0.0%	0.0%	0.0%
10 < E < 20	0.0%	0.0%	0.0%	0.0%	0.0%	0.0%
20 < E < 30	0.0%	0.0%	0.1%	0.2%	0.1%	0.1%
30 < E < 40	0.1%	0.1%	0.2%	0.6%	0.4%	0.3%
40 < E < 50	0.2%	0.2%	0.4%	1.2%	0.9%	0.6%
50 < E < 60	0.3%	0.4%	0.7%	2.1%	1.6%	1.1%
60 < E < 70	0.4%	0.5%	1.0%	3.1%	2.5%	1.8%
70 < E < 80	0.2%	0.3%	0.7%	2.0%	1.7%	1.3%
80 < E < 90	0.6%	0.8%	1.7%	5.4%	4.6%	3.6%
90 < E < 100	0.4%	0.5%	1.0%	3.4%	3.0%	2.4%
100 < E < 110	0.6%	0.6%	1.1%	3.9%	3.5%	2.9%
110 < E < 120	2.1%	0.8%	1.3%	4.3%	4.0%	3.4%
120 < E < 140	23.3%	10.0%	3.2%	10.0%	9.4%	8.3%
140 < E < 160	20.5%	17.8%	4.6%	5.7%	5.4%	4.9%
160 < E < 180	20.6%	24.2%	15.3%	6.8%	6.6%	6.3%
180 < E < 200	30.6%	43.7%	68.7%	51.4%	56.4%	63.1%

6.0 CONCLUDING REMARKS

Using BRYNTRN and MATLAB, organ doses and dose equivalents were able to be extracted into the useful form as a function of particle energy and aluminum thickness. These are presented in tabular form and are also graphically depicted in the appendix. The data shows that the minimum aluminum shield thickness should be 25 g/cm^2 to meet the ICRP 60 dose limits. This value is from the eye/ocular lens data, the most conservative of the three organs in which calculations were run. Also, it was noticed that the differing aluminum depths had different primary energy contributors- as aluminum depth increased, the primary contributors increased in energy. Also, the energies 120 to 140 MeV are highly active among all the organs in this research and should be carefully dealt with in future research. This data is indicative of a worst-case scenario modeled using the October 19, 1989 data. It can be used as an upper bound for doses received by space crew personnel.

For future research, probability models that can accurately predict SPEs need to be developed. Also, dose limits need to be developed for missions outside the Earth's magnetosphere. This research utilized the ICRP 60 occupational dose limits, which can hardly be extrapolated to the dynamics of deep-space radiation protection. The minimal aluminum thickness this research determines to be needed is likely to be too heavy and costly. Lastly, the duration of SPEs cannot be reliably predicted[4]. This has a huge impact on the dose quantities, as longer-term events increase dose. New shielding technologies that mitigate the energies shown to be prevalent in this research should be researched.

7.0 REFERENCES

1. Townsend, L. W., *Implications of the Space Radiation Environment for Human Exploration in Deep Space.* Radiation Protection Dosimetry, pp.1-7 (2004).

2. Richardson, K. Martin, "Cumulative Doses from Large Solar Particle Events during Interplanetary Mission." University of Tennessee, 2000.

3. J. W. Wilson, L. W. Townsend, J. E. Nealy, S.Y. Chun, B.S. Hong, W. W. Buck, S. L. Lamkin, B. D. Ganapol, F. Khan, and F. A. Cucinotta, "BRYNTRN: A Baryon Transport Model." NASA Technical Paper #2887. 1989.

4. D. F. Smart and Shea, "Solar Radiation." Encyclopedia of Applied Physics. American Institute of Physics, New York City, NY 1996 (in press).

5. R. W. Langley and M. P. Billings, "A New Model for Estimating Space Proton Dose to Body Organs." *Nuclear Technology.* **15**, 68-74, July 1972.

6. Atwell

8.0 APPENDIX

8.1 DOSE EQUIVALENT TABLES: SKIN, EYE, BLOOD FORMING ORGANS

Table 13. Skin dose equivalent (cSv) per energy range per aluminum density through 15 g/cm^2

Skin dose eq. (cSv)	Aluminum Densities						
Energy range (MeV)	1 g/cm^2	2 g/cm^2	3 g/cm^2	5 g/cm^2	7 g/cm^2	10 g/cm^2	15 g/cm^2
0 < E < 10	0.0000	0.0000	0.0000	0.0000	0.0000	0.0000	0.0000
10 < E < 20	0.0040	0.0046	0.0039	0.0049	0.0034	0.0023	0.0024
20 < E < 30	902.8600	0.0531	0.0489	0.0456	0.0432	0.0379	0.0304
30 < E < 40	213.2500	316.2500	0.1079	0.0979	0.0903	0.0811	0.0661
40 < E < 50	136.1300	154.0500	195.9000	0.1573	0.1466	0.1294	0.1073
50 < E < 60	69.1250	65.7550	85.1880	63.5150	0.3275	0.1758	0.1454
60 < E < 70	35.5130	40.2190	42.3970	65.9970	45.5530	0.5308	0.1740
70 < E < 80	14.5830	13.7050	13.0820	14.9350	21.6590	5.9106	0.0992
80 < E < 90	22.2290	20.4590	20.1770	19.8890	21.2480	31.1200	14.7300
90 < E < 100	9.9989	8.4502	7.6250	7.0195	6.8912	7.1888	0.2761
100 < E < 110	7.7841	7.4141	7.0613	6.1161	5.5242	5.3281	1.6233
110 < E < 120	6.2572	5.6606	5.3233	5.2454	4.8893	4.2687	4.3548
120 < E < 140	9.3579	8.6590	8.0500	7.2979	6.9708	6.5630	5.9368
140 < E < 160	3.2405	3.0772	2.9202	2.6651	2.5002	2.3150	1.9053
160 < E < 180	2.4946	2.3594	2.2306	2.0341	1.9255	1.8215	1.5074
180 < E < 200	3.3568	3.2133	3.0640	2.7936	2.5856	2.3899	2.0145
Sum	1436.1840	649.3295	393.1791	197.8134	120.3578	67.8629	32.9730

Table 14. Skin dose equivalent (cSv) per energy range per aluminum density through 85 g/cm^2

Skin dose eq. (cSv)	Aluminum Densities					
Energy range (MeV)	20 g/cm^2	25 g/cm^2	35 g/cm^2	50 g/cm^2	65 g/cm^2	85 g/cm^2
0 < E < 10	0.0000	0.0000	0.0000	0.0000	0.0000	0.0000
10 < E < 20	0.0020	0.0015	0.0010	0.0005	0.0005	0.0002
20 < E < 30	0.0248	0.0202	0.0133	0.0072	0.0058	0.0028
30 < E < 40	0.0542	0.0446	0.0299	0.0165	0.0127	0.0063
40 < E < 50	0.0883	0.0726	0.0493	0.0276	0.0208	0.0103
50 < E < 60	0.1208	0.1002	0.0688	0.0393	0.0293	0.0147
60 < E < 70	0.1453	0.1214	0.0847	0.0495	0.0369	0.0189
70 < E < 80	0.0814	0.0687	0.0486	0.0291	0.0217	0.0113
80 < E < 90	0.1912	0.1549	0.1116	0.0685	0.0513	0.0276
90 < E < 100	0.2761	0.0877	0.0627	0.0396	0.0298	0.0165
100 < E < 110	1.6233	0.1369	0.0667	0.0428	0.0324	0.0182
110 < E < 120	4.3548	0.5750	0.0714	0.0460	0.0349	0.0200
120 < E < 140	5.9368	4.7184	0.3432	0.1002	0.0766	0.0450
140 < E < 160	1.9053	1.7709	0.8463	0.0573	0.0439	0.0264
160 < E < 180	1.5074	1.3739	1.2314	0.0951	0.0730	0.0461
180 < E < 200	2.0145	1.8638	1.5922	0.7295	0.5968	0.4313
Sum	18.3261	11.1103	4.6212	1.3484	1.0661	0.6955

Table 15. Skin dose equivalent (cSv) contribution percentage per energy range per aluminum density through 15 g/cm^2

Skin dose eq. percentage	Aluminum Densities						
Energy range (MeV)	**1 g/cm^2**	**2 g/cm^2**	**3 g/cm^2**	**5 g/cm^2**	**7 g/cm^2**	**10 g/cm^2**	**15 g/cm^2**
0 < E < 10	0.0%	0.0%	0.0%	0.0%	0.0%	0.0%	0.0%
10 < E < 20	0.0%	0.0%	0.0%	0.0%	0.0%	0.0%	0.0%
20 < E < 30	62.9%	0.0%	0.0%	0.0%	0.0%	0.1%	0.1%
30 < E < 40	14.8%	48.7%	0.0%	0.0%	0.1%	0.1%	0.2%
40 < E < 50	9.5%	23.7%	49.8%	0.1%	0.1%	0.2%	0.3%
50 < E < 60	4.8%	10.1%	21.7%	32.1%	0.3%	0.3%	0.4%
60 < E < 70	2.5%	6.2%	10.8%	33.4%	37.8%	0.8%	0.5%
70 < E < 80	1.0%	2.1%	3.3%	7.6%	18.0%	8.7%	0.3%
80 < E < 90	1.5%	3.2%	5.1%	10.1%	17.7%	45.9%	44.7%
90 < E < 100	0.7%	1.3%	1.9%	3.5%	5.7%	10.6%	0.8%
100 < E < 110	0.5%	1.1%	1.8%	3.1%	4.6%	7.9%	4.9%
110 < E < 120	0.4%	0.9%	1.4%	2.7%	4.1%	6.3%	13.2%
120 < E < 140	0.7%	1.3%	2.0%	3.7%	5.8%	9.7%	18.0%
140 < E < 160	0.2%	0.5%	0.7%	1.3%	2.1%	3.4%	5.8%
160 < E < 180	0.2%	0.4%	0.6%	1.0%	1.6%	2.7%	4.6%
180 < E < 200	0.2%	0.5%	0.8%	1.4%	2.1%	3.5%	6.1%

Table 16. Skin dose equivalent (cSv) contribution percentage per energy range per aluminum density through 85 g/cm^2

Skin dose eq. percentage	Aluminum Densities					
Energy range (MeV)	**20 g/cm^2**	**25 g/cm^2**	**35 g/cm^2**	**50 g/cm^2**	**65 g/cm^2**	**85 g/cm^2**
0 < E < 10	0.0%	0.0%	0.0%	0.0%	0.0%	0.0%
10 < E < 20	0.0%	0.0%	0.0%	0.0%	0.0%	0.0%
20 < E < 30	0.1%	0.2%	0.3%	0.5%	0.5%	0.4%
30 < E < 40	0.3%	0.4%	0.6%	1.2%	1.2%	0.9%
40 < E < 50	0.5%	0.7%	1.1%	2.0%	1.9%	1.5%
50 < E < 60	0.7%	0.9%	1.5%	2.9%	2.7%	2.1%
60 < E < 70	0.8%	1.1%	1.8%	3.7%	3.5%	2.7%
70 < E < 80	0.4%	0.6%	1.1%	2.2%	2.0%	1.6%
80 < E < 90	1.0%	1.4%	2.4%	5.1%	4.8%	4.0%
90 < E < 100	1.5%	0.8%	1.4%	2.9%	2.8%	2.4%
100 < E < 110	8.9%	1.2%	1.4%	3.2%	3.0%	2.6%
110 < E < 120	23.8%	5.2%	1.5%	3.4%	3.3%	2.9%
120 < E < 140	32.4%	42.5%	7.4%	7.4%	7.2%	6.5%
140 < E < 160	10.4%	15.9%	18.3%	4.2%	4.1%	3.8%
160 < E < 180	8.2%	12.4%	26.6%	7.1%	6.8%	6.6%
180 < E < 200	11.0%	16.8%	34.5%	54.1%	56.0%	62.0%

Table 17. Eye dose equivalent (cSv) per energy range per aluminum density through 15 g/cm^2

Eye dose eq. (cSv)	Aluminum Densities						
Energy range (MeV)	**1 g/cm^2**	**2 g/cm^2**	**3 g/cm^2**	**5 g/cm^2**	**7 g/cm^2**	**10 g/cm^2**	**15 g/cm^2**
0 < E < 10	0.0000	0.0000	0.0000	0.0000	0.0000	0.0000	0.0000
10 < E < 20	0.0017	0.0020	0.0016	0.0031	0.0020	0.0015	0.0012
20 < E < 30	272.4700	0.0472	0.0431	-0.1967	0.0382	0.0335	0.0275
30 < E < 40	102.0600	95.5100	0.1141	0.3400	0.0952	0.0848	0.0691
40 < E < 50	280.2900	159.9300	59.2460	0.1722	0.1594	0.1416	0.1172
50 < E < 60	65.7890	76.0230	122.9000	20.3620	0.2592	0.1957	0.1617
60 < E < 70	43.1890	48.6000	45.1780	71.7230	20.2840	0.3464	0.1936
70 < E < 80	15.5620	15.2140	15.3010	16.2260	27.7330	2.5227	0.1085
80 < E < 90	23.3790	22.3070	21.9000	22.5170	24.1480	26.4740	13.5100
90 < E < 100	9.0868	8.3014	7.9474	7.6512	7.4619	8.1950	0.2057
100 < E < 110	7.1798	6.8971	6.6995	6.1758	5.9285	5.8147	1.0642
110 < E < 120	6.2165	5.5957	5.2575	5.0451	4.8090	4.5272	3.5474
120 < E < 140	9.5118	8.8657	8.3365	7.6051	7.1074	6.5632	6.4064
140 < E < 160	3.2624	3.1048	2.9664	2.7599	2.6219	2.4448	1.9470
160 < E < 180	2.4546	2.3267	2.2144	2.0584	1.9818	1.8962	1.5436
180 < E < 200	3.2699	3.1144	2.9667	2.7176	2.5431	2.3896	2.0940
Sum	843.7225	455.8390	301.0722	165.1597	105.1726	61.6308	30.9971

Table 18. Eye dose equivalent (cSv) per energy range per aluminum density through 85 g/cm^2

Eye dose eq. (cSv)	Aluminum Densities					
Energy range (MeV)	**20 g/cm^2**	**25 g/cm^2**	**35 g/cm^2**	**50 g/cm^2**	**65 g/cm^2**	**85 g/cm^2**
0 < E < 10	0.0000	0.0000	0.0000	0.0000	0.0000	0.0000
10 < E < 20	0.0011	0.0008	0.0005	0.0003	0.0002	0.0001
20 < E < 30	0.0224	0.0183	0.0120	0.0065	0.0040	0.0018
30 < E < 40	0.0566	0.0465	0.0313	0.0172	0.0103	0.0046
40 < E < 50	0.0963	0.0793	0.0538	0.0301	0.0178	0.0081
50 < E < 60	0.1343	0.1112	0.0764	0.0435	0.0258	0.0119
60 < E < 70	0.1616	0.1350	0.0942	0.0550	0.0330	0.0156
70 < E < 80	0.0905	0.0762	0.0539	0.0322	0.0196	0.0095
80 < E < 90	0.2059	0.1710	0.1231	0.0755	0.0469	0.0235
90 < E < 100	0.2057	0.0952	0.0689	0.0434	0.0274	0.0143
100 < E < 110	1.0642	0.1262	0.0730	0.0468	0.0300	0.0159
110 < E < 120	3.5474	0.4169	0.0775	0.0501	0.0326	0.0177
120 < E < 140	6.4064	4.2681	0.3034	0.1088	0.0720	0.0403
140 < E < 160	1.9470	1.9131	0.7193	0.0608	0.0409	0.0236
160 < E < 180	1.5436	1.4081	1.2174	0.0913	0.0634	0.0388
180 < E < 200	2.0940	1.9333	1.6610	0.6932	0.5369	0.3836
Sum	17.5769	10.7991	4.5659	1.3547	0.9608	0.6092

Table 19. Eye dose equivalent (cSv) contribution percentage per energy range per aluminum density through 15 g/cm^2

Eye dose eq. percentage	Aluminum Densities						
Energy range (MeV)	**1 g/cm^2**	**2 g/cm^2**	**3 g/cm^2**	**5 g/cm^2**	**7 g/cm^2**	**10 g/cm^2**	**15 g/cm^2**
0 < E < 10	0.0%	0.0%	0.0%	0.0%	0.0%	0.0%	0.0%
10 < E < 20	0.0%	0.0%	0.0%	0.0%	0.0%	0.0%	0.0%
20 < E < 30	32.3%	0.0%	0.0%	-0.1%	0.0%	0.1%	0.1%
30 < E < 40	12.1%	21.0%	0.0%	0.2%	0.1%	0.1%	0.2%
40 < E < 50	33.2%	35.1%	19.7%	0.1%	0.2%	0.2%	0.4%
50 < E < 60	7.8%	16.7%	40.8%	12.3%	0.2%	0.3%	0.5%
60 < E < 70	5.1%	10.7%	15.0%	43.4%	19.3%	0.6%	0.6%
70 < E < 80	1.8%	3.3%	5.1%	9.8%	26.4%	4.1%	0.4%
80 < E < 90	2.8%	4.9%	7.3%	13.6%	23.0%	43.0%	43.6%
90 < E < 100	1.1%	1.8%	2.6%	4.6%	7.1%	13.3%	0.7%
100 < E < 110	0.9%	1.5%	2.2%	3.7%	5.6%	9.4%	3.4%
110 < E < 120	0.7%	1.2%	1.7%	3.1%	4.6%	7.3%	11.4%
120 < E < 140	1.1%	1.9%	2.8%	4.6%	6.8%	10.6%	20.7%
140 < E < 160	0.4%	0.7%	1.0%	1.7%	2.5%	4.0%	6.3%
160 < E < 180	0.3%	0.5%	0.7%	1.2%	1.9%	3.1%	5.0%
180 < E < 200	0.4%	0.7%	1.0%	1.6%	2.4%	3.9%	6.8%

Table 20. Eye dose equivalent (cSv) contribution percentage per energy range per aluminum density through 85 g/cm^2

Eye dose eq. percentage	Aluminum Densities					
Energy range (MeV)	**20 g/cm^2**	**25 g/cm^2**	**35 g/cm^2**	**50 g/cm^2**	**65 g/cm^2**	**85 g/cm^2**
0 < E < 10	0.0%	0.0%	0.0%	0.0%	0.0%	0.0%
10 < E < 20	0.0%	0.0%	0.0%	0.0%	0.0%	0.0%
20 < E < 30	0.1%	0.2%	0.3%	0.5%	0.4%	0.3%
30 < E < 40	0.3%	0.4%	0.7%	1.3%	1.1%	0.8%
40 < E < 50	0.5%	0.7%	1.2%	2.2%	1.9%	1.3%
50 < E < 60	0.8%	1.0%	1.7%	3.2%	2.7%	1.9%
60 < E < 70	0.9%	1.2%	2.1%	4.1%	3.4%	2.6%
70 < E < 80	0.5%	0.7%	1.2%	2.4%	2.0%	1.6%
80 < E < 90	1.2%	1.6%	2.7%	5.6%	4.9%	3.9%
90 < E < 100	1.2%	0.9%	1.5%	3.2%	2.9%	2.3%
100 < E < 110	6.1%	1.2%	1.6%	3.5%	3.1%	2.6%
110 < E < 120	20.2%	3.9%	1.7%	3.7%	3.4%	2.9%
120 < E < 140	36.4%	39.5%	6.6%	8.0%	7.5%	6.6%
140 < E < 160	11.1%	17.7%	15.8%	4.5%	4.3%	3.9%
160 < E < 180	8.8%	13.0%	26.7%	6.7%	6.6%	6.4%
180 < E < 200	11.9%	17.9%	36.4%	51.2%	55.9%	63.0%

Table 21. Blood forming organs dose equivalent (cSv) per energy range per aluminum density through 15 g/cm^2

BFO dose eq. (cSv)	Aluminum Densities						
Energy range (MeV)	1 g/cm^2	2 g/cm^2	3 g/cm^2	5 g/cm^2	7 g/cm^2	10 g/cm^2	15 g/cm^2
0 < E < 10	0.0000	0.0000	0.0000	0.0000	-0.5753	0.0000	0.0000
10 < E < 20	0.0008	0.0007	0.0006	0.0007	0.0005	0.0005	0.0004
20 < E < 30	0.3757	0.0232	0.0224	0.0206	0.0190	0.0167	0.0136
30 < E < 40	0.1119	-0.0756	0.0615	0.0569	0.0526	0.0467	0.0383
40 < E < 50	0.9425	0.4688	0.0232	0.1016	0.0941	0.0837	0.0690
50 < E < 60	6.8438	1.2389	0.5534	0.1223	0.1357	0.1212	0.1005
60 < E < 70	7.5527	7.1643	4.6216	0.6727	0.1780	0.1500	0.1253
70 < E < 80	6.6912	4.9653	2.9103	1.8856	0.3331	0.0872	0.0722
80 < E < 90	11.8730	10.5540	9.3924	6.0556	3.3542	0.7093	0.1687
90 < E < 100	6.8754	5.5716	4.6941	3.7634	2.8573	1.3998	0.1472
100 < E < 110	5.1015	5.3523	5.2339	4.0228	3.1323	2.0546	0.4554
110 < E < 120	4.6945	4.2156	3.9530	3.9203	3.4436	2.4293	1.0591
120 < E < 140	7.6842	7.4474	7.1318	6.3935	5.8209	5.0016	3.3212
140 < E < 160	2.5360	2.5501	2.5537	2.4942	2.3792	2.1810	1.7273
160 < E < 180	1.8428	1.8082	1.7843	1.7684	1.7740	1.7411	1.5530
180 < E < 200	2.4243	2.3745	2.3290	2.2481	2.1800	2.1076	2.0309
Sum	65.5503	53.6593	45.2652	33.5267	25.1792	18.1304	10.8820

Table 22. Blood forming organs dose equivalent (cSv) per energy range per aluminum density through 85 g/cm^2

BFO dose eq. (cSv)	Aluminum Densities					
Energy range (MeV)	20 g/cm^2	25 g/cm^2	35 g/cm^2	50 g/cm^2	65 g/cm^2	85 g/cm^2
0 < E < 10	0.0000	0.0000	0.0000	0.0000	0.0000	0.0000
10 < E < 20	0.0003	0.0002	0.0002	0.0001	0.0000	0.0000
20 < E < 30	0.0111	0.0090	0.0060	0.0032	0.0017	0.0007
30 < E < 40	0.0314	0.0258	0.0173	0.0096	0.0050	0.0021
40 < E < 50	0.0568	0.0468	0.0317	0.0177	0.0094	0.0040
50 < E < 60	0.0833	0.0690	0.0474	0.0270	0.0145	0.0064
60 < E < 70	0.1048	0.0875	0.0612	0.0358	0.0196	0.0089
70 < E < 80	0.0608	0.0512	0.0363	0.0218	0.0122	0.0057
80 < E < 90	0.1403	0.1192	0.0862	0.0531	0.0306	0.0150
90 < E < 100	0.0798	0.0678	0.0499	0.0316	0.0187	0.0095
100 < E < 110	0.0973	0.0729	0.0540	0.0349	0.0211	0.0110
110 < E < 120	0.2078	0.0831	0.0580	0.0381	0.0234	0.0125
120 < E < 140	1.5866	0.5129	0.1314	0.0848	0.0533	0.0294
140 < E < 160	1.2728	0.7316	0.1120	0.0463	0.0297	0.0168
160 < E < 180	1.2619	0.9415	0.2653	0.0503	0.0329	0.0192
180 < E < 200	1.9078	1.6873	1.0185	0.2044	0.1487	0.1013
Sum	6.9026	4.5057	1.9754	0.6587	0.4209	0.2425

Table 23. Blood forming organs dose equivalent (cSv) contribution percentage per energy range per aluminum density through 15 g/cm^2

BFO dose eq. percentage	Aluminum Densities						
Energy range (MeV)	1 g/cm^2	2 g/cm^2	3 g/cm^2	5 g/cm^2	7 g/cm^2	10 g/cm^2	15 g/cm^2
0 < E < 10	0.0%	0.0%	0.0%	0.0%	-2.3%	0.0%	0.0%
10 < E < 20	0.0%	0.0%	0.0%	0.0%	0.0%	0.0%	0.0%
20 < E < 30	0.6%	0.0%	0.0%	0.1%	0.1%	0.1%	0.1%
30 < E < 40	0.2%	-0.1%	0.1%	0.2%	0.2%	0.3%	0.4%
40 < E < 50	1.5%	0.9%	0.1%	0.3%	0.4%	0.5%	0.6%
50 < E < 60	10.6%	2.3%	1.2%	0.4%	0.5%	0.7%	0.9%
60 < E < 70	11.7%	13.4%	10.2%	2.0%	0.7%	0.8%	1.2%
70 < E < 80	10.3%	9.3%	6.4%	5.6%	1.3%	0.5%	0.7%
80 < E < 90	18.3%	19.7%	20.8%	18.1%	13.3%	3.9%	1.6%
90 < E < 100	10.6%	10.4%	10.4%	11.2%	11.3%	7.7%	1.4%
100 < E < 110	7.9%	10.0%	11.6%	12.0%	12.4%	11.3%	4.2%
110 < E < 120	7.2%	7.9%	8.7%	11.7%	13.7%	13.4%	9.7%
120 < E < 140	11.9%	13.9%	15.8%	19.1%	23.1%	27.6%	30.5%
140 < E < 160	3.9%	4.8%	5.6%	7.4%	9.4%	12.0%	15.9%
160 < E < 180	2.8%	3.4%	3.9%	5.3%	7.0%	9.6%	14.3%
180 < E < 200	3.7%	4.4%	5.1%	6.7%	8.7%	11.6%	18.7%

Table 24. Blood forming organs dose equivalent (cSv) contribution percentage per energy range per aluminum density through 85 g/cm^2

BFO dose eq. percentage	Aluminum Densities					
Energy range (MeV)	20 g/cm^2	25 g/cm^2	35 g/cm^2	50 g/cm^2	65 g/cm^2	85 g/cm^2
0 < E < 10	0.0%	0.0%	0.0%	0.0%	0.0%	0.0%
10 < E < 20	0.0%	0.0%	0.0%	0.0%	0.0%	0.0%
20 < E < 30	0.2%	0.2%	0.3%	0.5%	0.4%	0.3%
30 < E < 40	0.5%	0.6%	0.9%	1.5%	1.2%	0.9%
40 < E < 50	0.8%	1.0%	1.6%	2.7%	2.2%	1.7%
50 < E < 60	1.2%	1.5%	2.4%	4.1%	3.4%	2.6%
60 < E < 70	1.5%	1.9%	3.1%	5.4%	4.7%	3.7%
70 < E < 80	0.9%	1.1%	1.8%	3.3%	2.9%	2.4%
80 < E < 90	2.0%	2.6%	4.4%	8.1%	7.3%	6.2%
90 < E < 100	1.2%	1.5%	2.5%	4.8%	4.5%	3.9%
100 < E < 110	1.4%	1.6%	2.7%	5.3%	5.0%	4.5%
110 < E < 120	3.0%	1.8%	2.9%	5.8%	5.6%	5.2%
120 < E < 140	23.0%	11.4%	6.7%	12.9%	12.7%	12.1%
140 < E < 160	18.4%	16.2%	5.7%	7.0%	7.0%	6.9%
160 < E < 180	18.3%	20.9%	13.4%	7.6%	7.8%	7.9%
180 < E < 200	27.6%	37.4%	51.6%	31.0%	35.3%	41.8%

8.2 Quality Factor Tables: Skin, Eye, Blood Forming Organs

Table 25. Skin quality factors per energy range per aluminum density through 15 g/cm^2

Skin quality factor	Aluminum Densities						
Energy range (MeV)	1 g/cm^2	2 g/cm^2	3 g/cm^2	5 g/cm^2	7 g/cm^2	10 g/cm^2	15 g/cm^2
0 < E < 10	1.8558	1.6756	1.6011	1.5337	1.5038	1.4876	1.493
10 < E < 20	1.8558	1.6756	1.6011	1.5334	1.5038	1.4876	1.493
20 < E < 30	1.536	1.6764	1.601	1.5332	1.5035	1.4872	1.4924
30 < E < 40	1.2443	1.4515	1.6007	1.5328	1.5028	1.4862	1.4906
40 < E < 50	1.2658	1.2336	1.4349	1.5319	1.5016	1.4843	1.4875
50 < E < 60	1.2792	1.271	1.2739	1.4204	1.4995	1.4817	1.4831
60 < E < 70	1.3205	1.3186	1.3019	1.3103	1.4033	1.4758	1.4777
70 < E < 80	1.3484	1.3431	1.3369	1.3231	1.3118	1.4516	1.4731
80 < E < 90	1.3693	1.3682	1.3656	1.356	1.3426	1.3909	1.4741
90 < E < 100	1.388	1.3916	1.3906	1.3864	1.3804	1.3649	1.4725
100 < E < 110	1.4049	1.408	1.4071	1.4035	1.4007	1.392	1.4548
110 < E < 120	1.4281	1.4311	1.4293	1.4236	1.4198	1.4148	1.4212
120 < E < 140	1.4647	1.4693	1.4694	1.4643	1.4583	1.4531	1.4295
140 < E < 160	1.5063	1.5116	1.5121	1.5091	1.5038	1.4968	1.474
160 < E < 180	1.5369	1.5428	1.544	1.5423	1.5382	1.5313	1.5093
180 < E < 200	1.5847	1.5909	1.5927	1.5927	1.5908	1.5859	1.57

Table 26. Skin quality factors per energy range per aluminum density through 85 g/cm^2

Skin quality factor	Aluminum Densities					
Energy range (MeV)	20 g/cm^2	25 g/cm^2	35 g/cm^2	50 g/cm^2	65 g/cm^2	85 g/cm^2
0 < E < 10	1.5183	1.556	1.6572	1.8552	1.8719	1.7757
10 < E < 20	1.5182	1.5559	1.6571	1.8551	1.8717	1.7756
20 < E < 30	1.5174	1.5548	1.6555	1.8529	1.8695	1.7742
30 < E < 40	1.5149	1.5515	1.6507	1.8462	1.863	1.77
40 < E < 50	1.5104	1.5457	1.6421	1.8339	1.8515	1.7626
50 < E < 60	1.5041	1.5373	1.6296	1.8159	1.8348	1.7516
60 < E < 70	1.4962	1.5268	1.6137	1.7926	1.8133	1.7373
70 < E < 80	1.4896	1.518	1.6002	1.7724	1.7946	1.7247
80 < E < 90	1.482	1.5078	1.5843	1.748	1.7719	1.709
90 < E < 100	1.4725	1.4969	1.5672	1.7211	1.747	1.6915
100 < E < 110	1.4548	1.4886	1.5547	1.701	1.7281	1.6779
110 < E < 120	1.4212	1.4755	1.5415	1.6793	1.7079	1.6631
120 < E < 140	1.4295	1.454	1.5183	1.6438	1.6745	1.6383
140 < E < 160	1.474	1.4603	1.4905	1.6064	1.6393	1.6118
160 < E < 180	1.5093	1.4983	1.486	1.5799	1.6138	1.5919
180 < E < 200	1.57	1.5607	1.5392	1.5606	1.5879	1.568

Table 27. Eye quality factors per energy range per aluminum density through 15 g/cm^2

Eye quality factor	Aluminum Densities						
Energy range (MeV)	**1 g/cm^2**	**2 g/cm^2**	**3 g/cm^2**	**5 g/cm^2**	**7 g/cm^2**	**10 g/cm^2**	**15 g/cm^2**
0 < E < 10	1.6684	1.5463	1.496	1.4513	1.4335	1.4277	1.4432
10 < E < 20	1.6684	1.5463	1.496	1.4513	1.4335	1.4277	1.4431
20 < E < 30	1.5405	1.5462	1.4959	1.4511	1.4333	1.4274	1.4426
30 < E < 40	1.3922	1.4664	1.4956	1.4506	1.4325	1.4263	1.4408
40 < E < 50	1.2788	1.2765	1.4422	1.4496	1.4311	1.4242	1.4375
50 < E < 60	1.2179	1.223	1.3052	1.4108	1.429	1.4212	1.4326
60 < E < 70	1.2753	1.2854	2.7505	1.3214	1.383	1.4169	1.4265
70 < E < 80	1.3114	1.3028	2.794	1.2827	1.3061	1.4046	1.4214
80 < E < 90	1.3423	1.3364	1.331	1.3204	1.3033	1.3531	1.4249
90 < E < 100	1.37	1.3675	1.3643	1.3571	1.3468	1.327	1.4265
100 < E < 110	1.3885	1.3879	1.3851	1.3792	1.3731	1.3584	1.4135
110 < E < 120	1.408	1.4089	1.4066	1.4017	1.3966	1.3877	1.3888
120 < E < 140	1.4424	1.4442	1.4435	1.4389	1.4336	1.4275	1.4021
140 < E < 160	1.4844	1.486	1.4854	1.4813	1.4759	1.4696	1.4489
160 < E < 180	1.5151	1.5177	1.518	1.5157	1.5113	1.5044	1.4847
180 < E < 200	1.5584	1.5618	1.563	1.5635	1.5624	1.5589	1.5456

Table 28. Eye quality factors per energy range per aluminum density through 85 g/cm^2

Eye quality factor	Aluminum Densities					
Energy range (MeV)	**20 g/cm^2**	**25 g/cm^2**	**35 g/cm^2**	**50 g/cm^2**	**65 g/cm^2**	**85 g/cm^2**
0 < E < 10	1.4752	1.5182	1.6281	1.8364	1.7591	1.6526
10 < E < 20	1.4752	1.5182	1.6281	1.8363	1.759	1.6525
20 < E < 30	1.4744	1.5172	1.6267	1.8345	1.7576	1.6517
30 < E < 40	1.4719	1.5139	1.622	1.828	1.7527	1.6488
40 < E < 50	1.4672	1.5078	1.6131	1.8155	1.7434	1.6432
50 < E < 60	1.4603	1.4988	1.5998	1.7967	1.7294	1.6348
60 < E < 70	1.4516	1.4874	1.5828	1.7722	1.711	1.6235
70 < E < 80	1.4443	1.4777	1.5683	1.7509	1.6949	1.6134
80 < E < 90	1.436	1.4666	1.5513	1.7252	1.6751	1.6007
90 < E < 100	1.4265	1.4549	1.533	1.697	1.6532	1.5863
100 < E < 110	1.4135	1.4461	1.5196	1.6758	1.6365	1.575
110 < E < 120	1.3888	1.4346	1.5055	1.653	1.6184	1.5625
120 < E < 140	1.4021	1.4184	1.4819	1.6155	1.5882	1.5411
140 < E < 160	1.4489	1.4311	1.4566	1.5761	1.5561	1.5182
160 < E < 180	1.4847	1.4733	1.4556	1.5484	1.5332	1.5013
180 < E < 200	1.5456	1.5373	1.5128	1.531	1.5159	1.4875

Table 29. Blood forming organs quality factors per energy range per aluminum density through 15 g/cm^2

BFO quality factor	Aluminum Densities						
Energy range (MeV)	1 g/cm^2	2 g/cm^2	3 g/cm^2	5 g/cm^2	7 g/cm^2	10 g/cm^2	15 g/cm^2
0 < E < 10	1.4057	1.4044	1.4049	1.4107	1.4206	1.4404	1.4821
10 < E < 20	1.4057	1.4044	1.4049	1.4107	1.4206	1.4404	1.4821
20 < E < 30	1.4075	1.4042	1.4047	1.4104	1.4202	1.4398	1.4814
30 < E < 40	1.4073	1.4041	1.4036	1.4091	1.4187	1.4379	1.4789
40 < E < 50	1.4033	1.3919	1.402	1.4065	1.4246	1.4342	1.4739
50 < E < 60	1.3772	1.3843	1.3878	1.4029	1.42	1.4284	1.4663
60 < E < 70	1.3532	1.377	1.3692	1.3857	1.405	1.421	1.4563
70 < E < 80	1.349	1.3561	1.3627	1.3721	1.3985	1.4147	1.4478
80 < E < 90	1.3462	1.3478	1.3556	1.3661	1.3837	1.4043	1.4378
90 < E < 100	1.3444	1.3474	1.3513	1.3586	1.3691	1.3901	1.4266
100 < E < 110	1.3528	1.3537	1.3552	1.3596	1.3668	1.381	1.4164
110 < E < 120	1.3696	1.3687	1.3675	1.3679	1.3701	1.3788	1.4051
120 < E < 140	1.4017	1.4008	1.4001	1.3967	1.3931	1.3952	1.4041
140 < E < 160	1.4493	1.4461	1.4429	1.4367	1.4309	1.4254	1.4203
160 < E < 180	1.4872	1.485	1.4824	1.4767	1.4708	1.4618	1.4499
180 < E < 200	1.5369	1.5364	1.5357	1.5338	1.531	1.5251	1.5148

Table 30. Blood forming organs quality factors per energy range per aluminum density through 85 g/cm^2

BFO quality factor	Aluminum Densities					
Energy range (MeV)	20 g/cm^2	25 g/cm^2	35 g/cm^2	50 g/cm^2	65 g/cm^2	85 g/cm^2
0 < E < 10	1.532	1.5884	1.7165	1.9351	1.8051	1.6804
10 < E < 20	1.532	1.5884	1.7165	1.9351	1.8051	1.6804
20 < E < 30	1.5312	1.5874	1.7152	1.9336	1.8041	1.6799
30 < E < 40	1.5281	1.5837	1.7106	1.9279	1.8004	1.6778
40 < E < 50	1.5219	1.5764	1.7011	1.9163	1.7927	1.6735
50 < E < 60	1.5123	1.565	1.6865	1.8981	1.7805	1.6665
60 < E < 70	1.4998	1.55	1.6669	1.8734	1.7636	1.6566
70 < E < 80	1.489	1.537	1.6497	1.8514	1.7484	1.6474
80 < E < 90	1.4763	1.5215	1.6288	1.8238	1.7287	1.6351
90 < E < 100	1.4626	1.5047	1.6059	1.7929	1.7064	1.6208
100 < E < 110	1.4524	1.4922	1.5886	1.769	1.6887	1.6091
110 < E < 120	1.4409	1.479	1.57	1.7428	1.6691	1.5957
120 < E < 140	1.4266	1.4575	1.5396	1.6984	1.6352	1.5721
140 < E < 160	1.4242	1.441	1.5079	1.6506	1.5984	1.5461
160 < E < 180	1.4439	1.4467	1.4891	1.6158	1.5713	1.5266
180 < E < 200	1.5057	1.4973	1.4988	1.5694	1.5344	1.4993

8.3 FIGURES

Figure 1. Skin absorbed dose per energy range per aluminum density

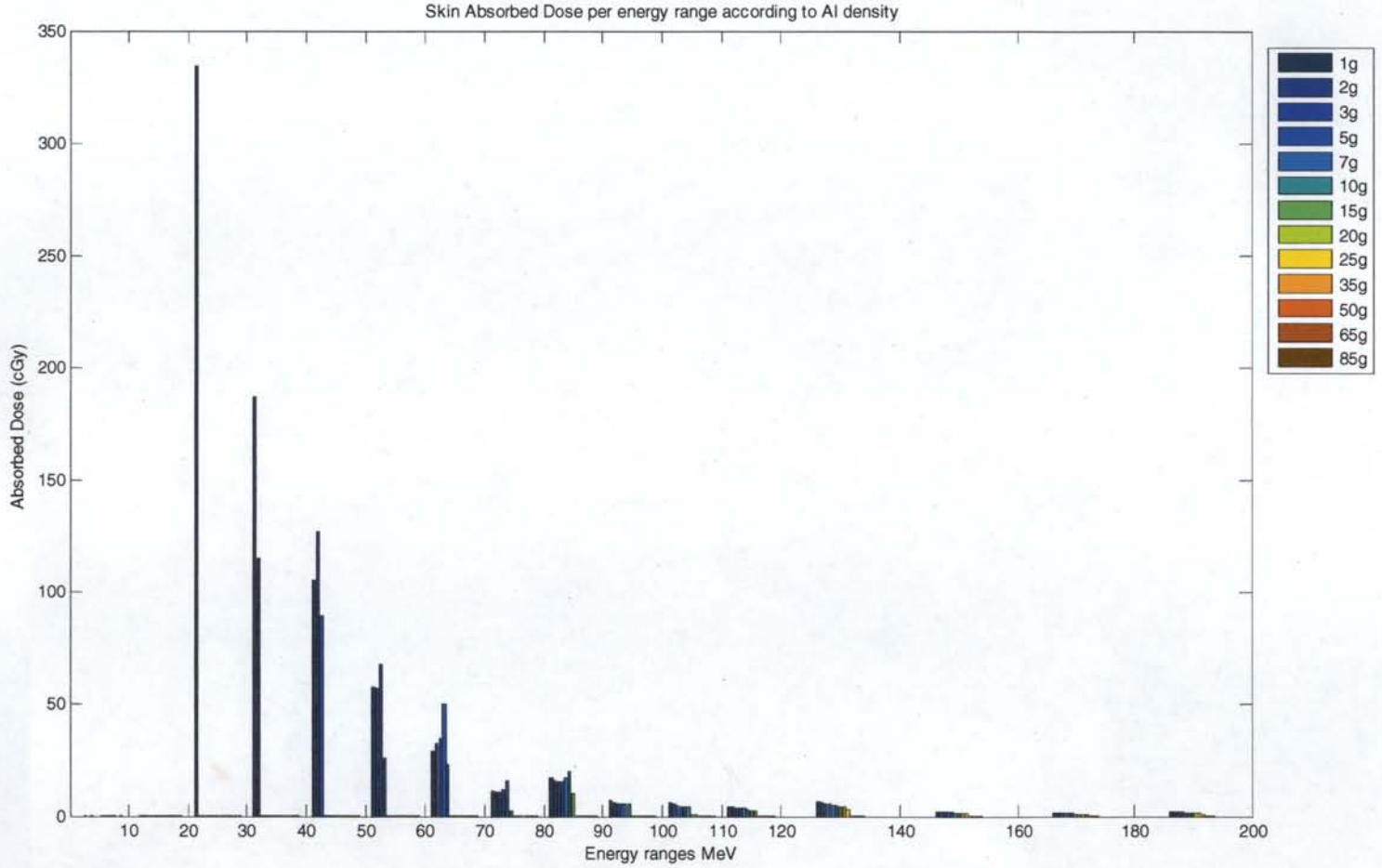

Figure 2. Skin dose equivalent per energy range per aluminum density

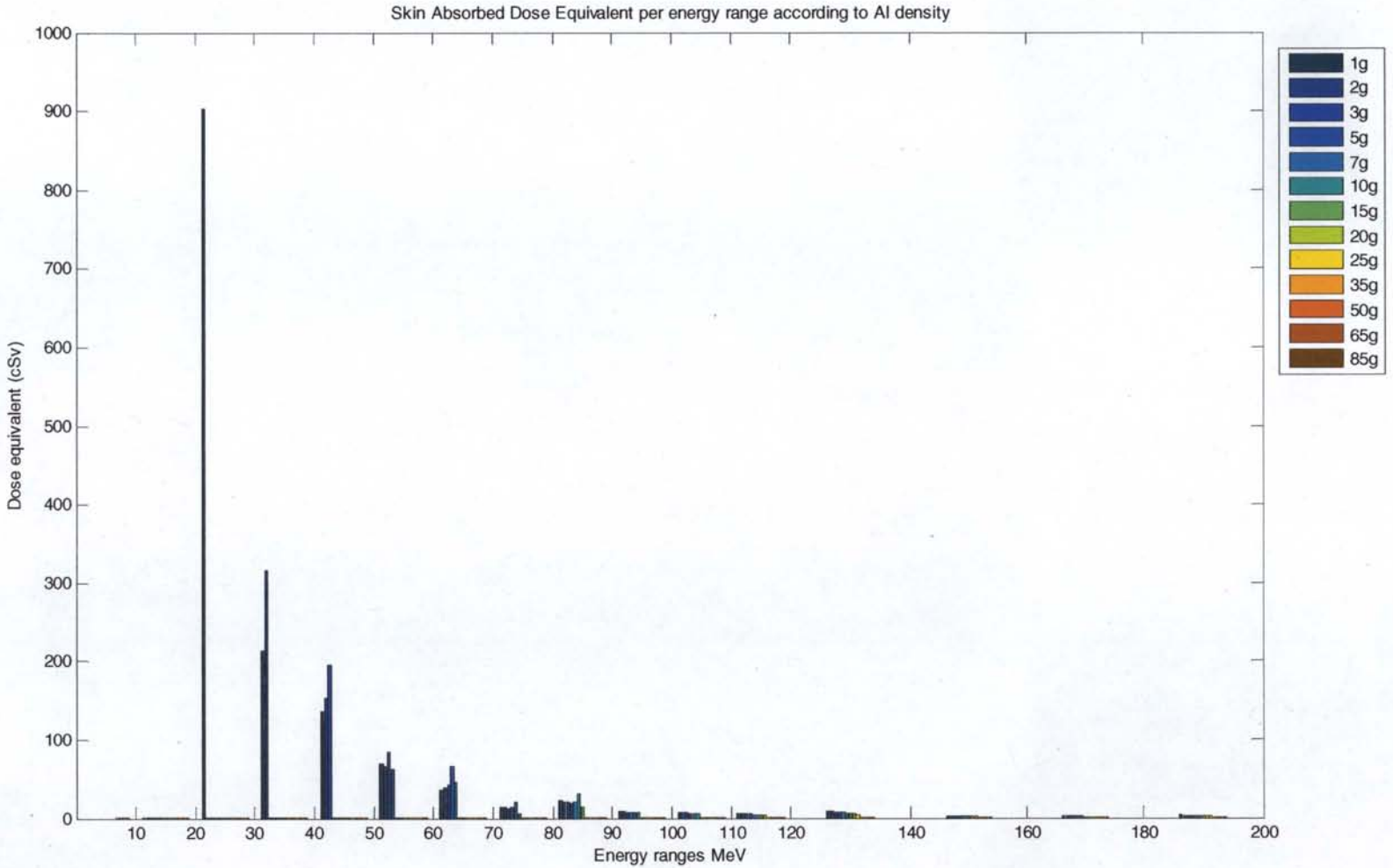

Figure 3. Eye absorbed dose per energy range per aluminum density

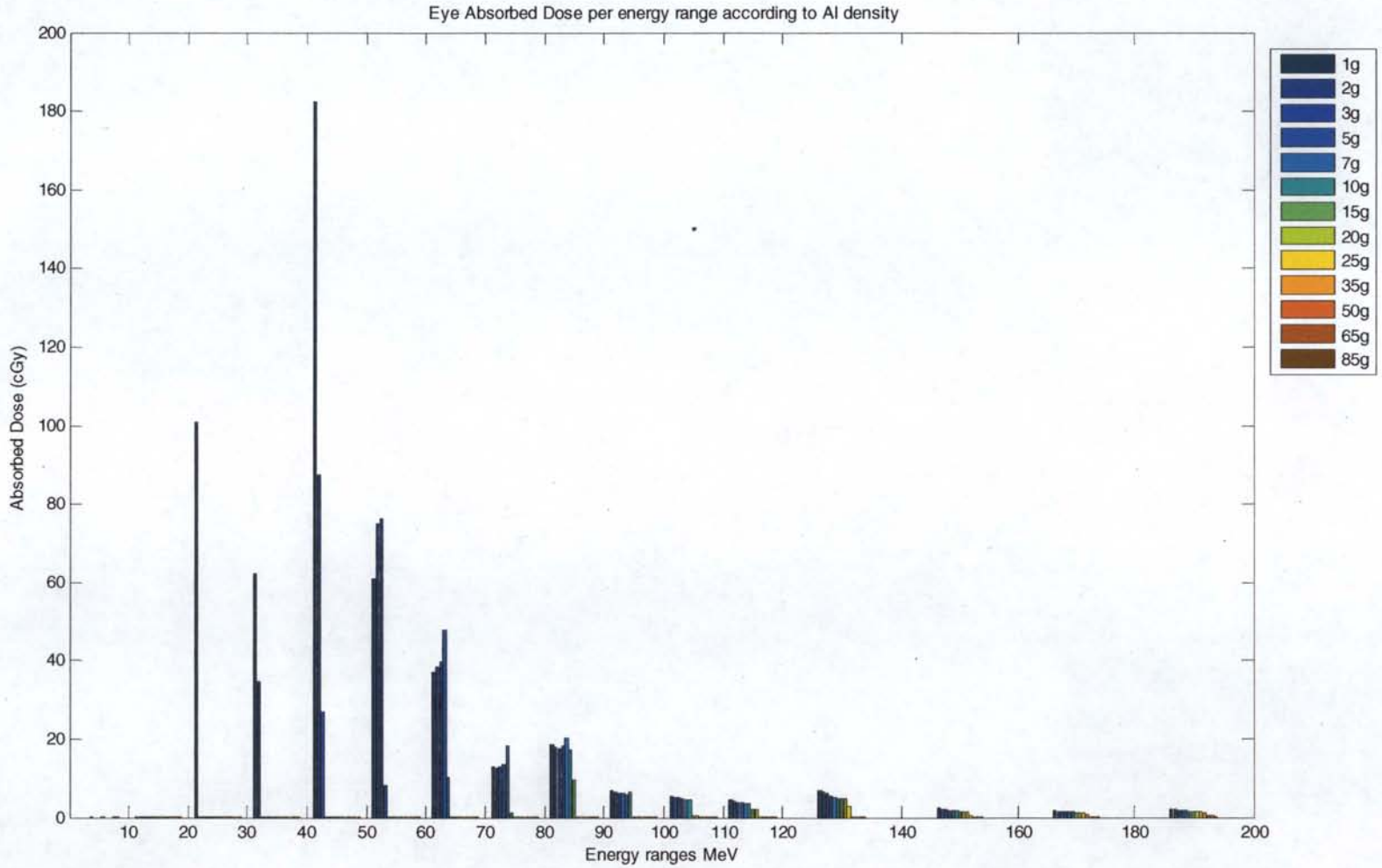

Figure 4. Eye dose equivalent per energy range per aluminum density

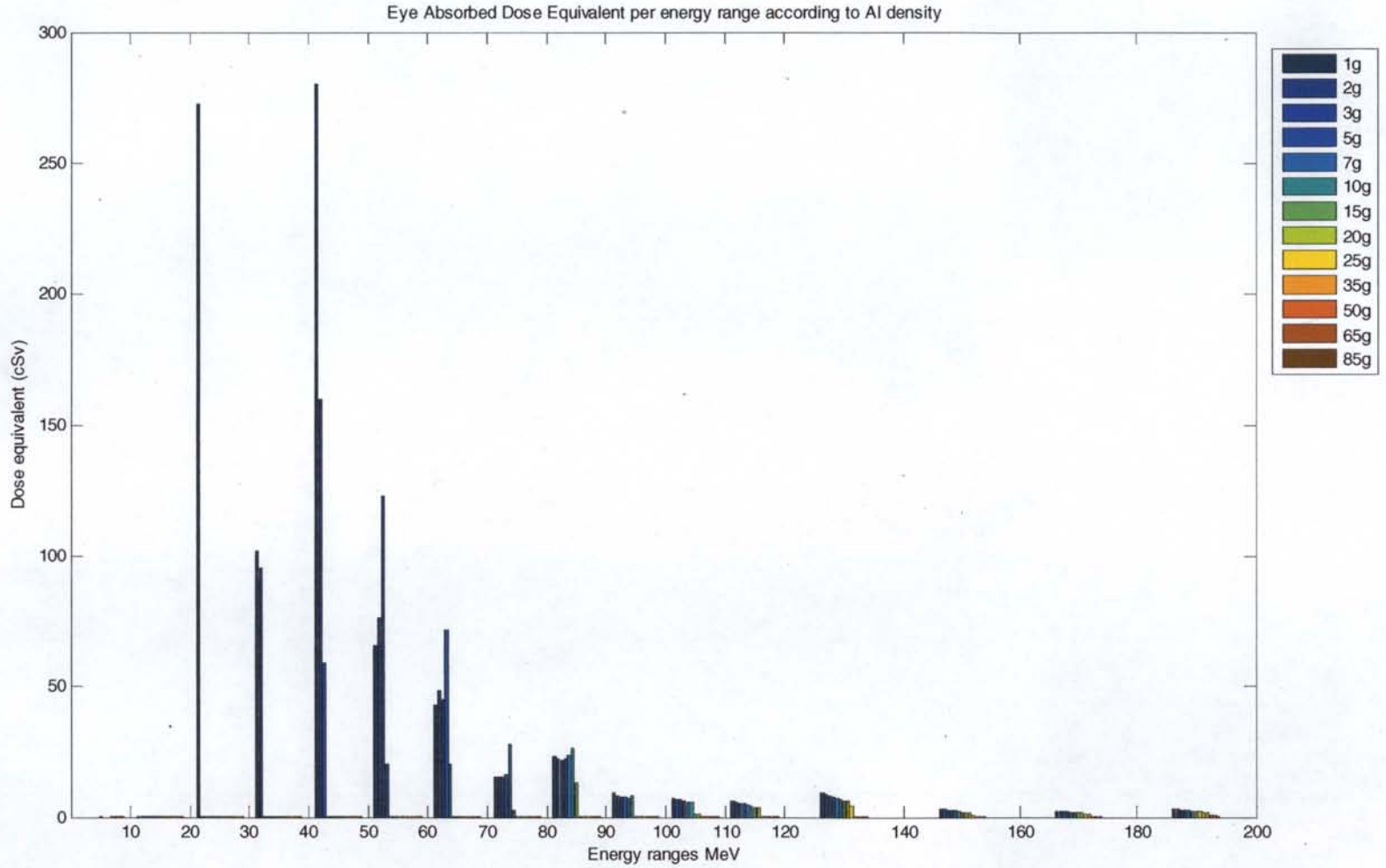

Figure 5. Blood forming organs absorbed dose per energy range per aluminum density

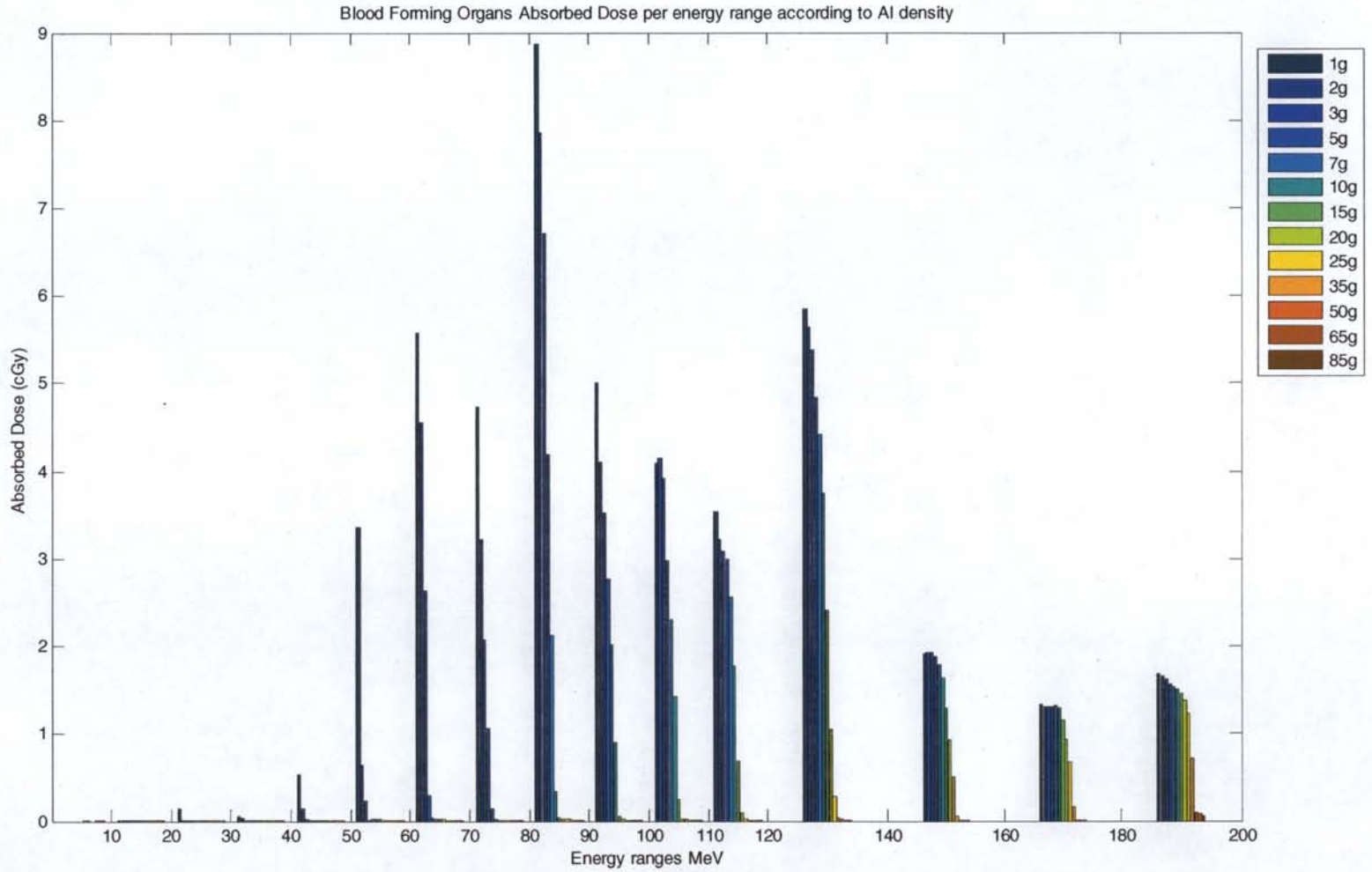

Figure 6. Blood forming organs dose equivalent per energy range per aluminum density

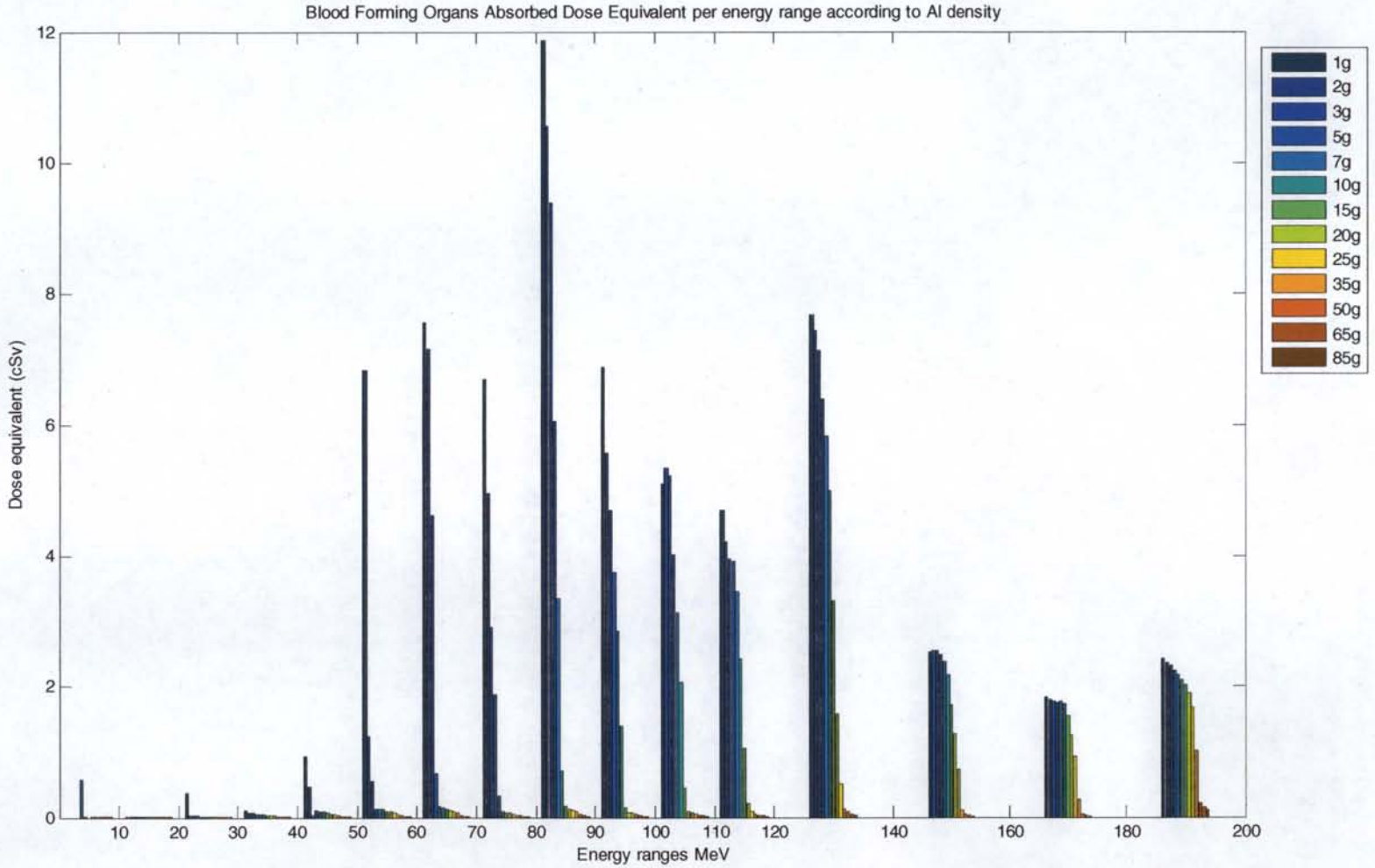

Figure 7. Skin absorbed dose per energy range per aluminum density through 15 g/cm^2

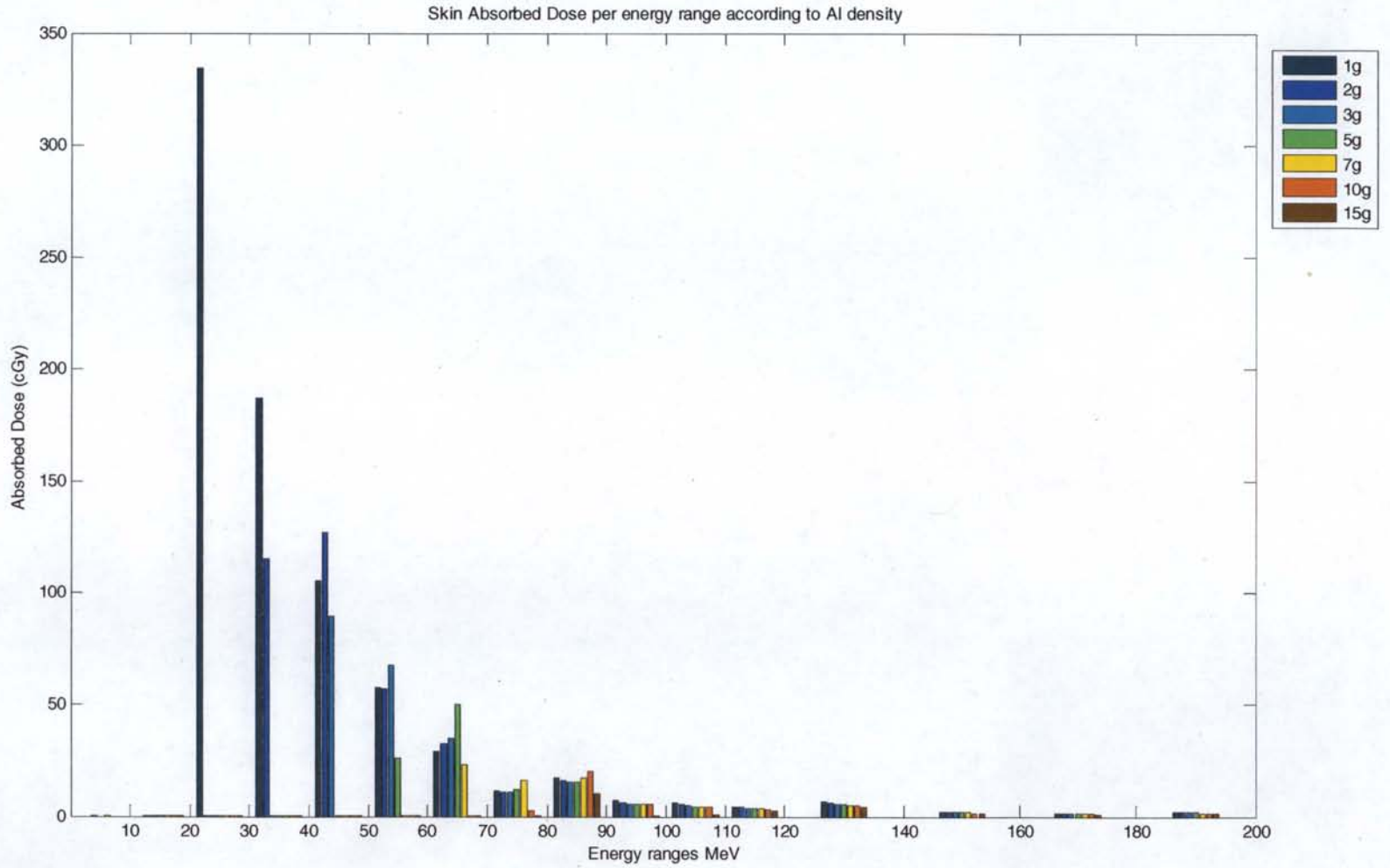

Figure 8. Skin dose equivalent per energy range per aluminum density through 15 g/cm^2

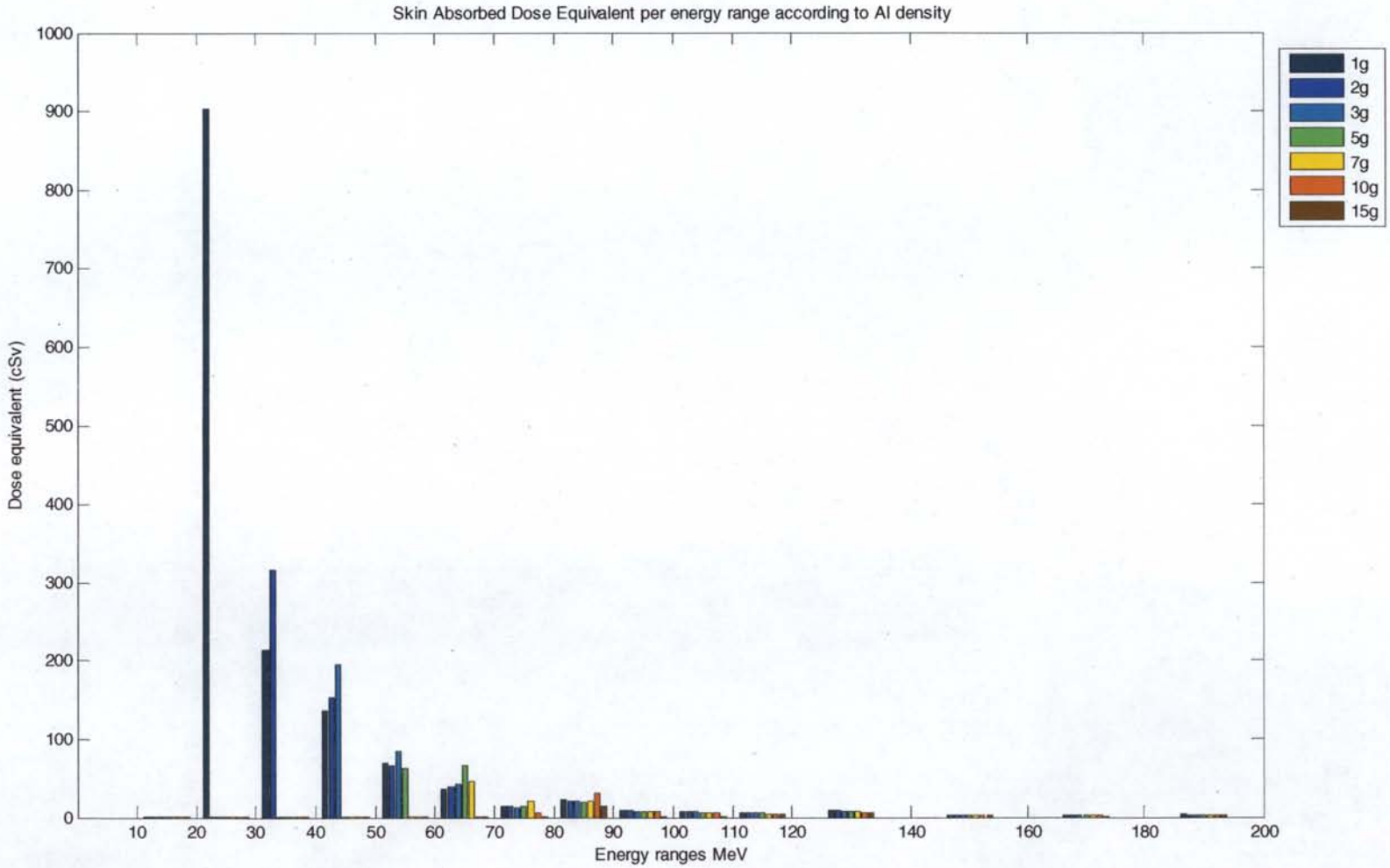

Figure 9. Eye absorbed dose per energy range per aluminum density through 15 g/cm^2

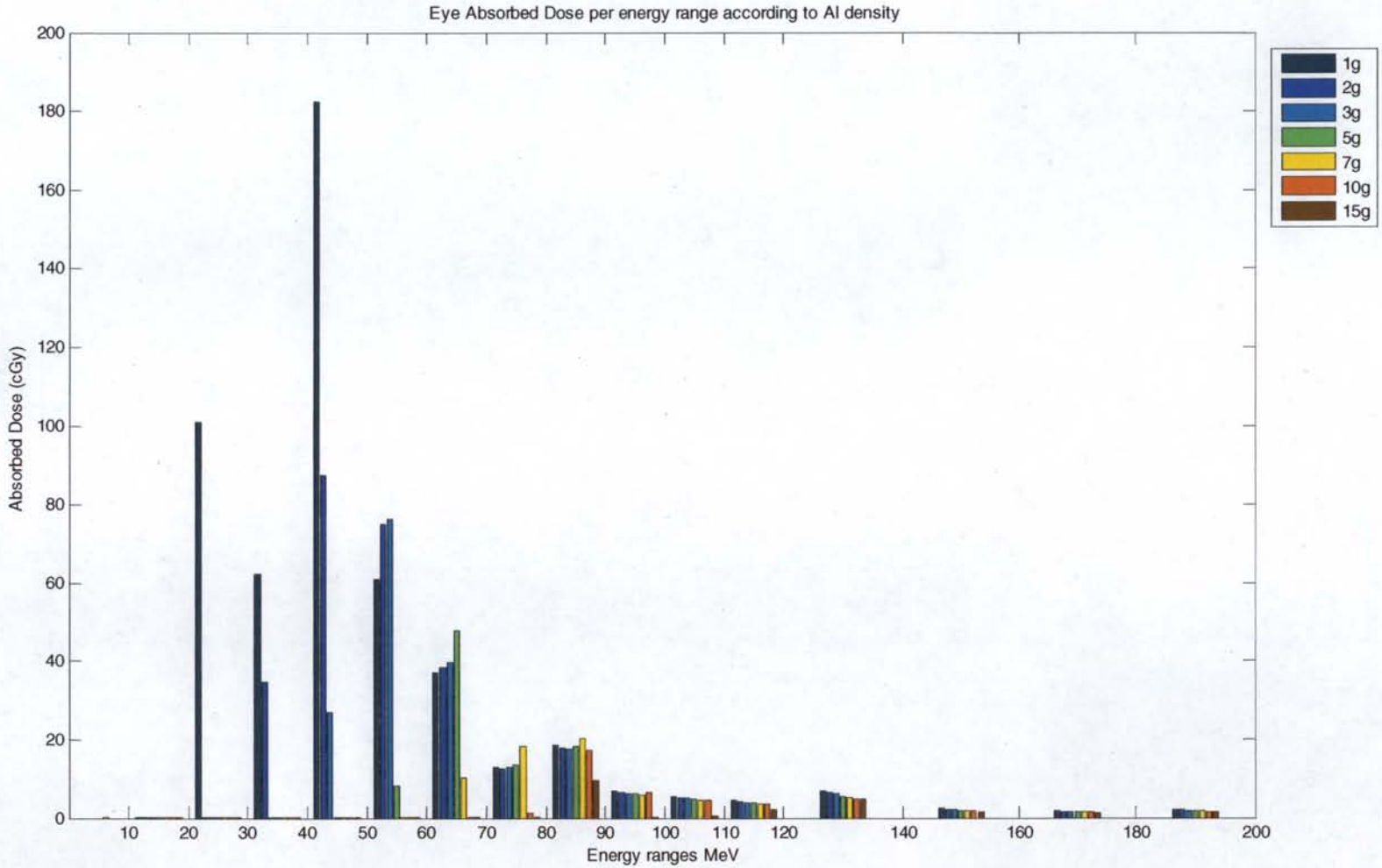

Figure 10. Eye dose equivalent per energy range per aluminum density through 15 g/cm^2

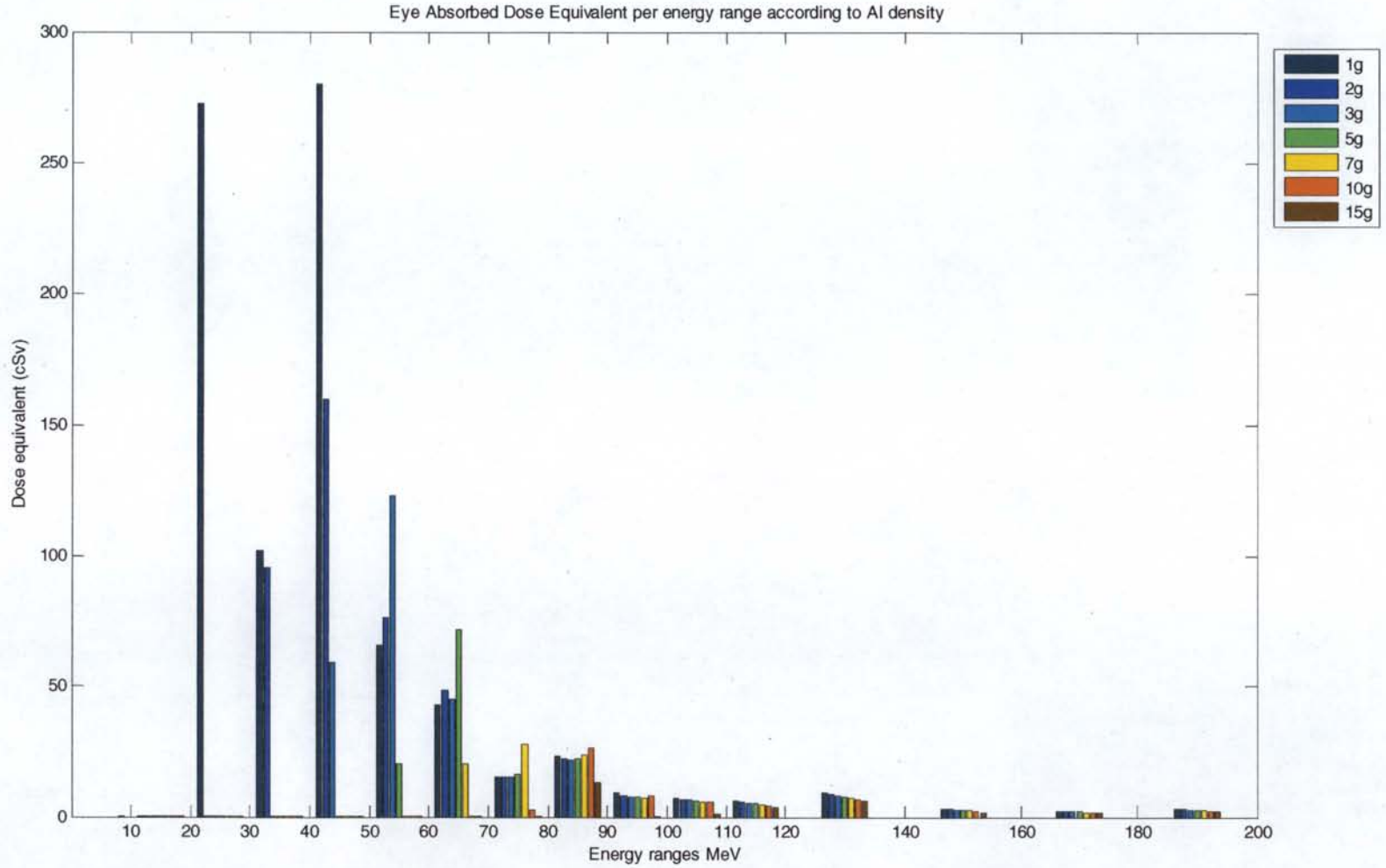

Figure 11. Blood forming organs absorbed dose per energy range per aluminum density through 15 g/cm^2

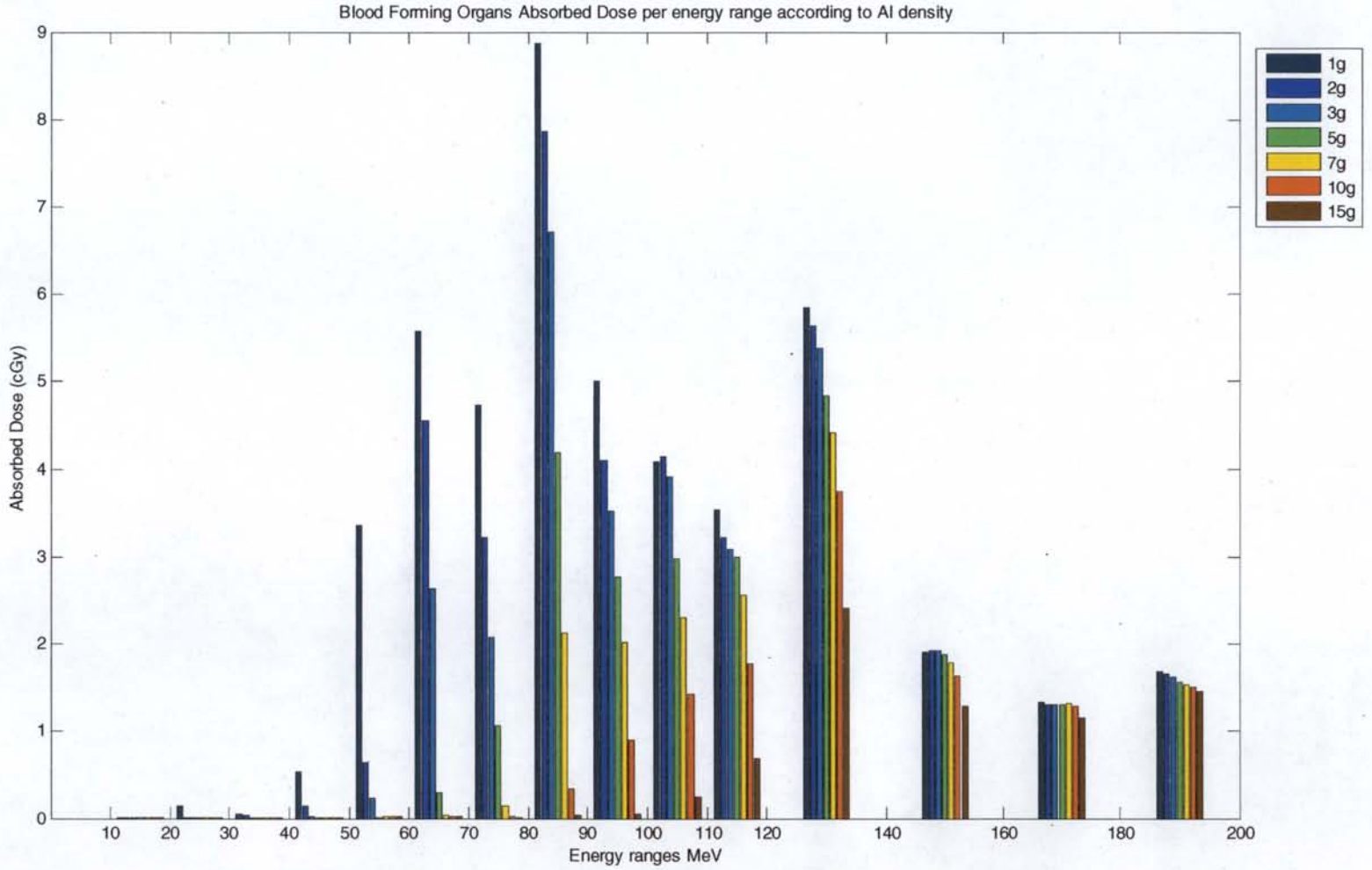

Figure 12. Blood forming organs dose equivalent per energy range per aluminum density through 15 g/cm^2

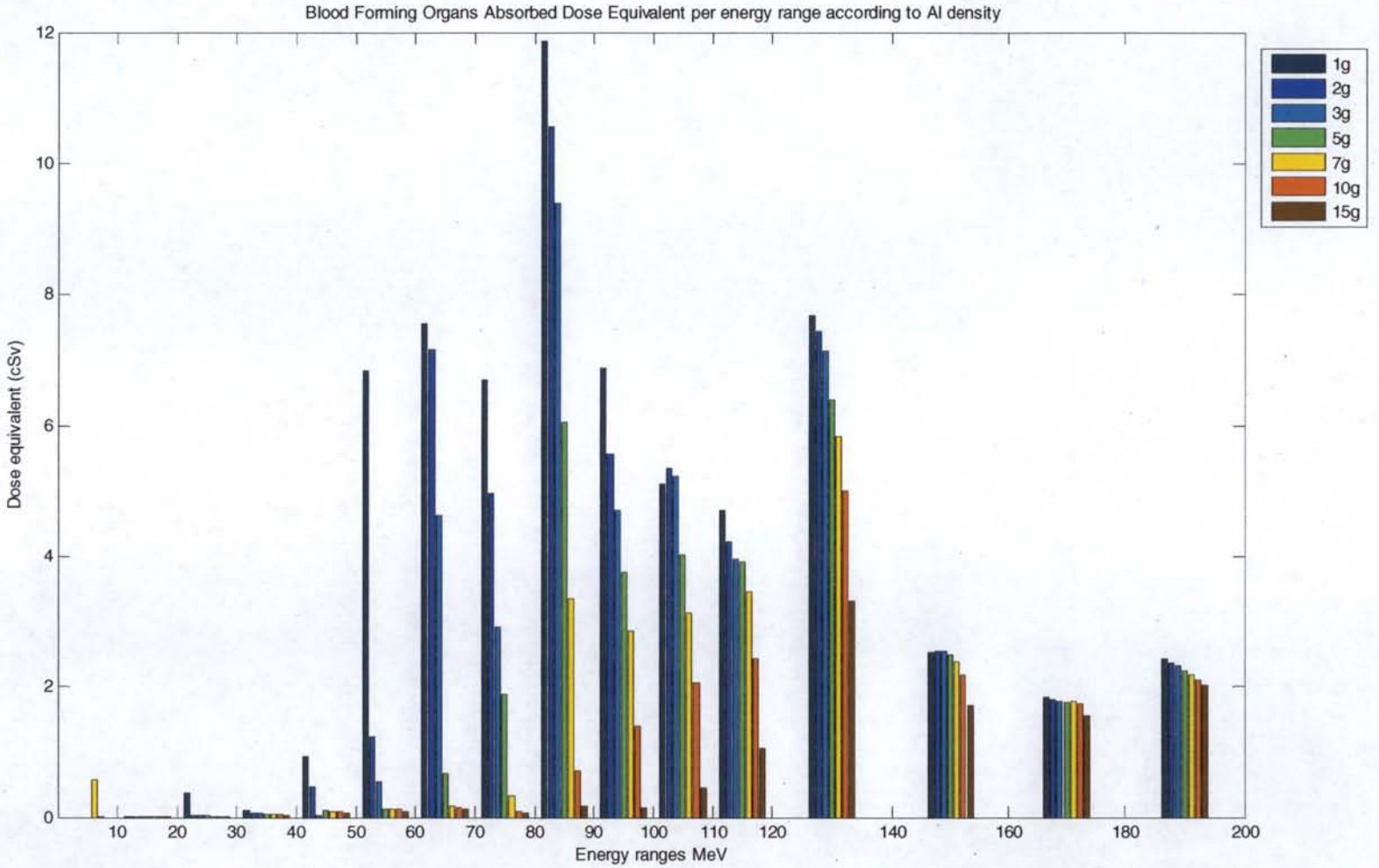

Figure 13. Skin absorbed dose per energy range per aluminum density through 85 g/cm^2

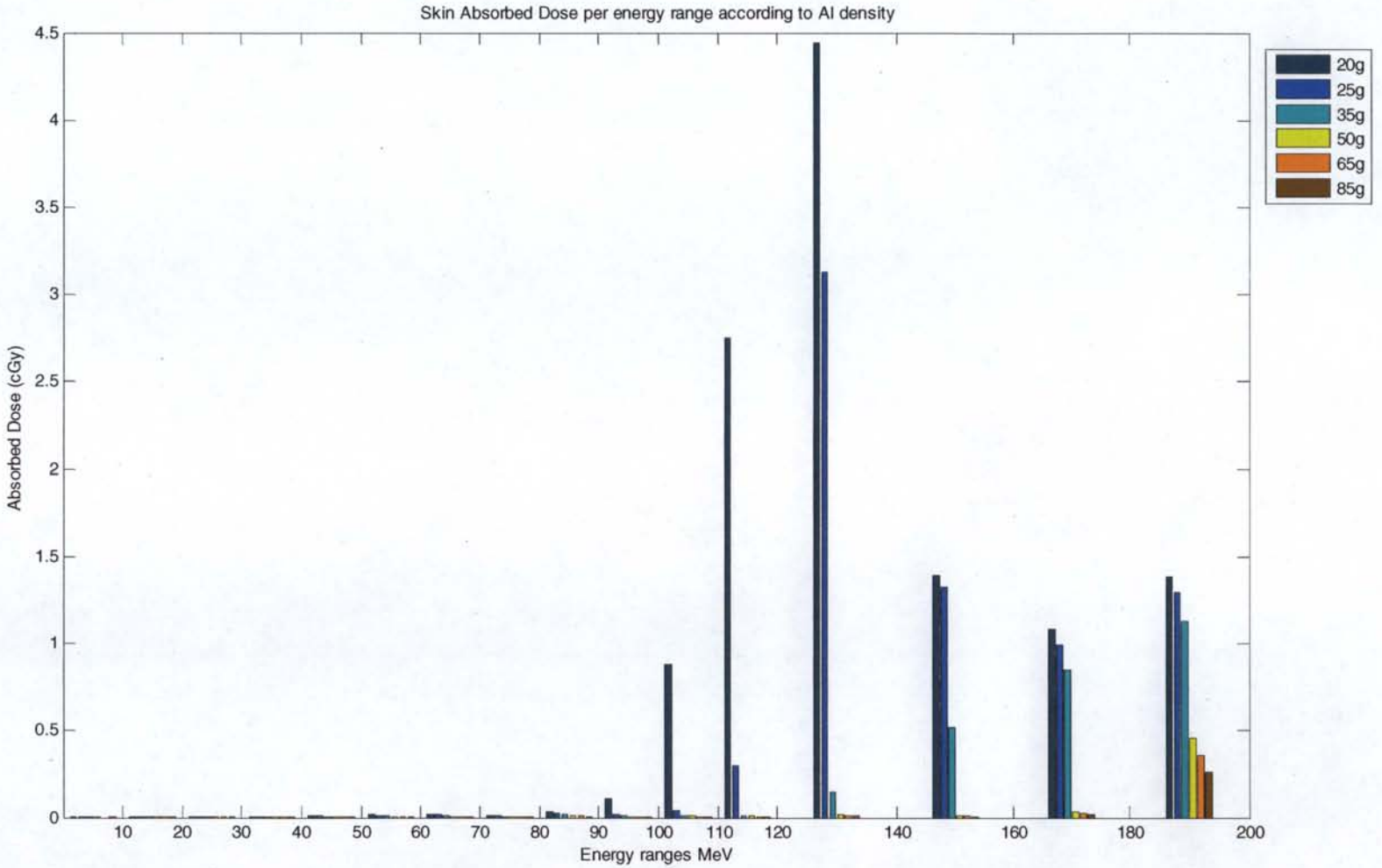

Figure 14. Skin dose equivalent per energy range per aluminum density through 85 g/cm^2

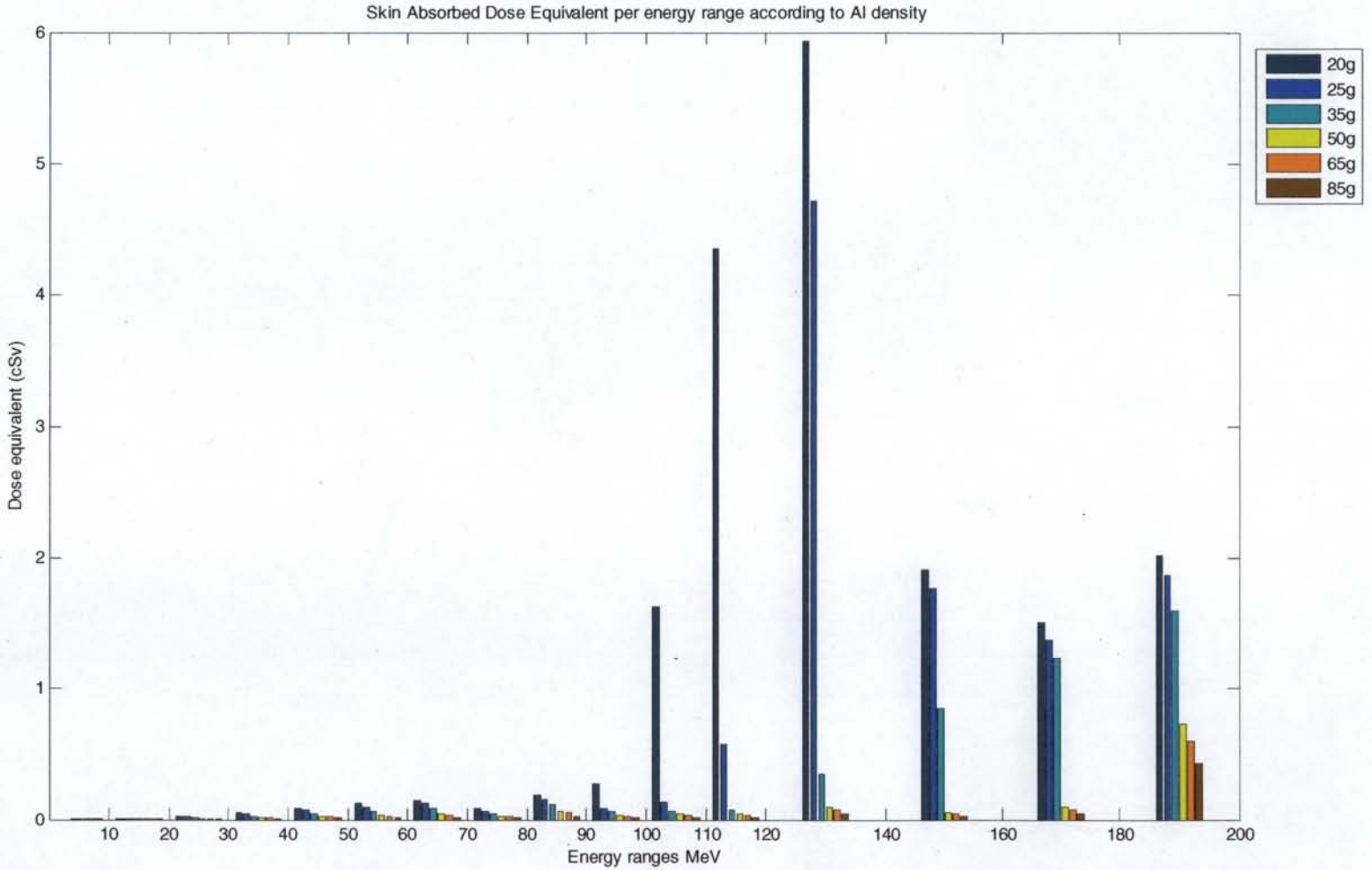

Figure 15. Eye absorbed dose per energy range per aluminum density through 85 g/cm^2

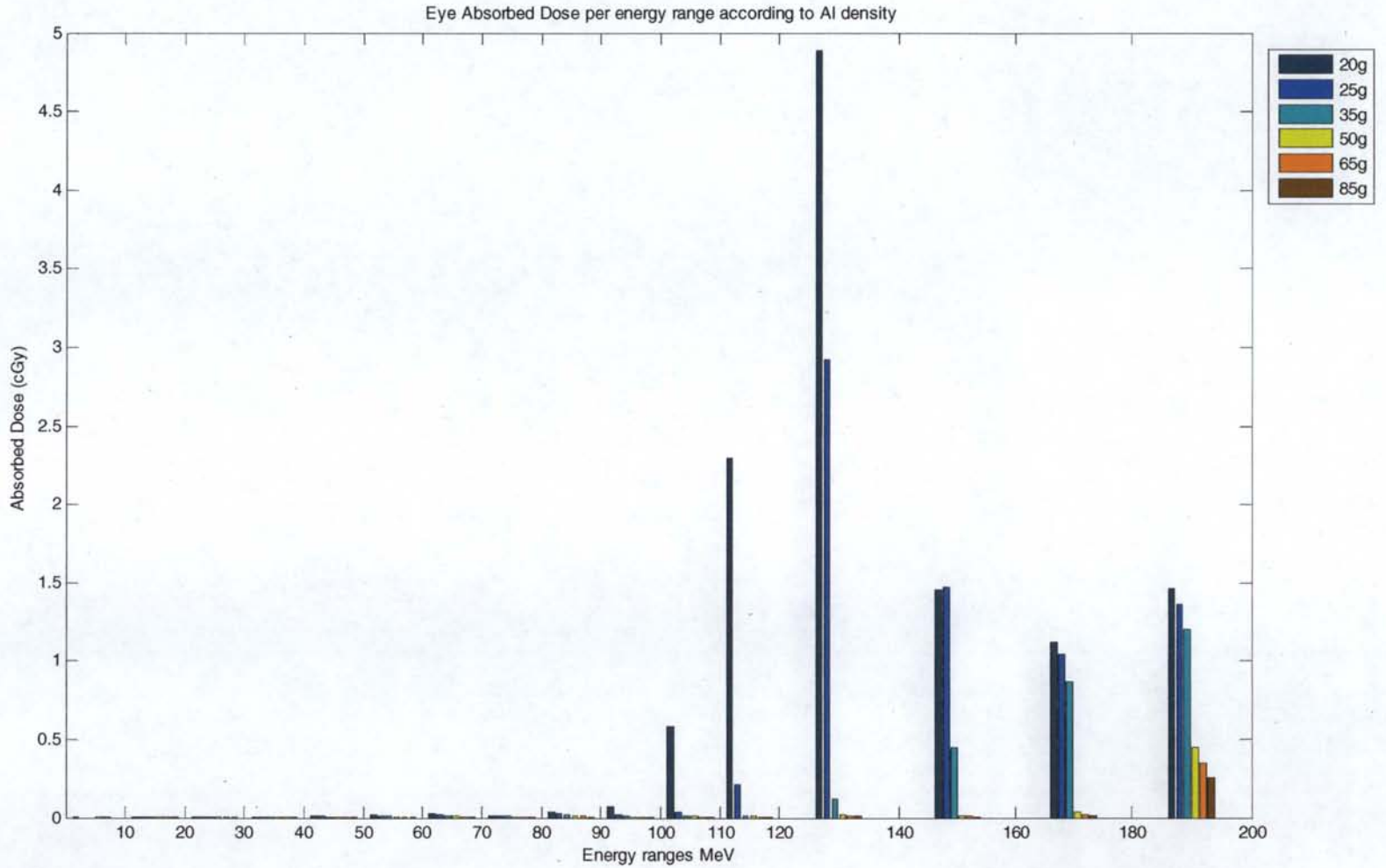

Figure 16. Eye dose equivalent per energy range per aluminum density through 85 g/cm^2

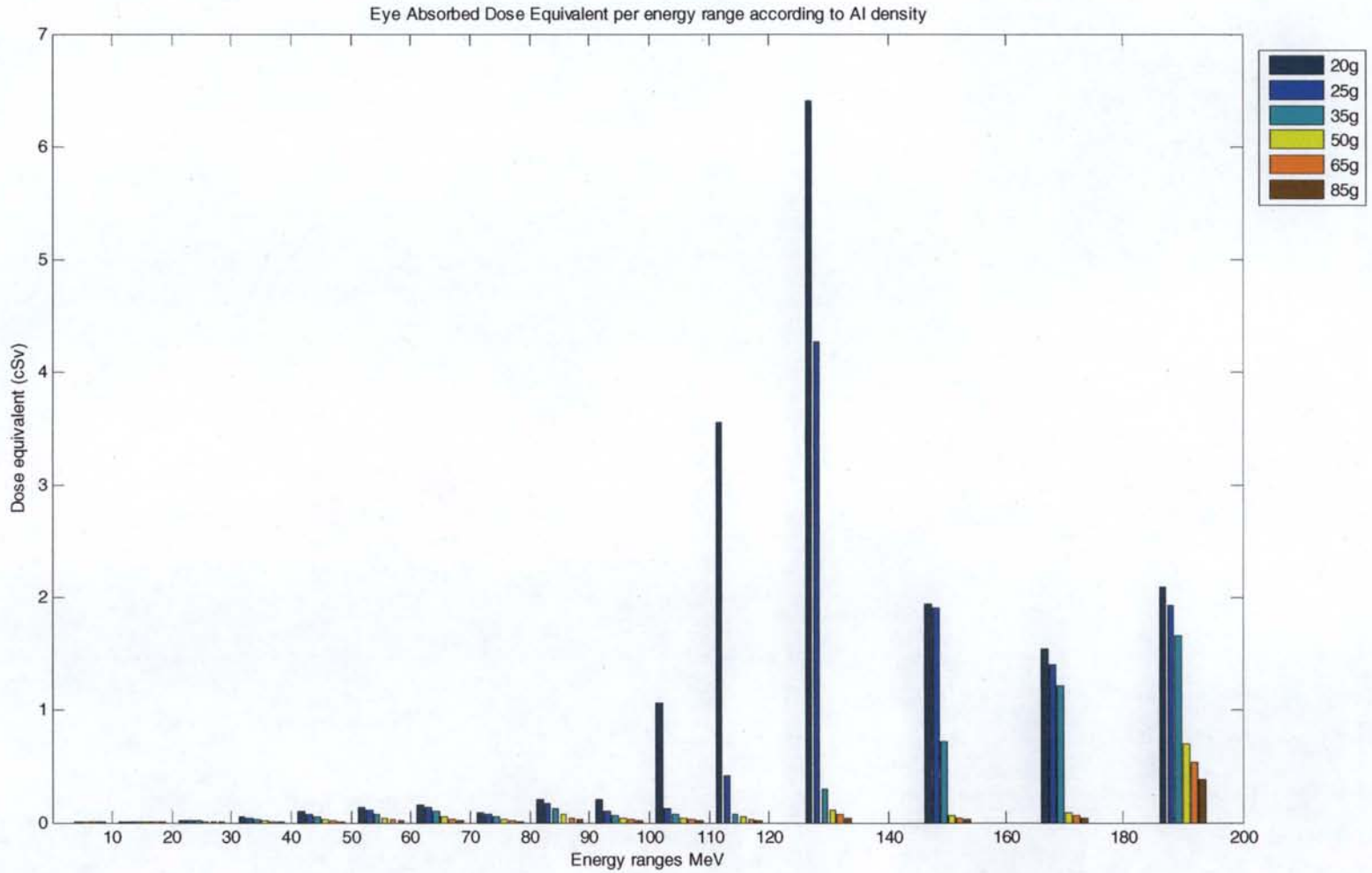

Figure 17. Blood forming organs absorbed dose per energy range per aluminum density through 85 g/cm^2

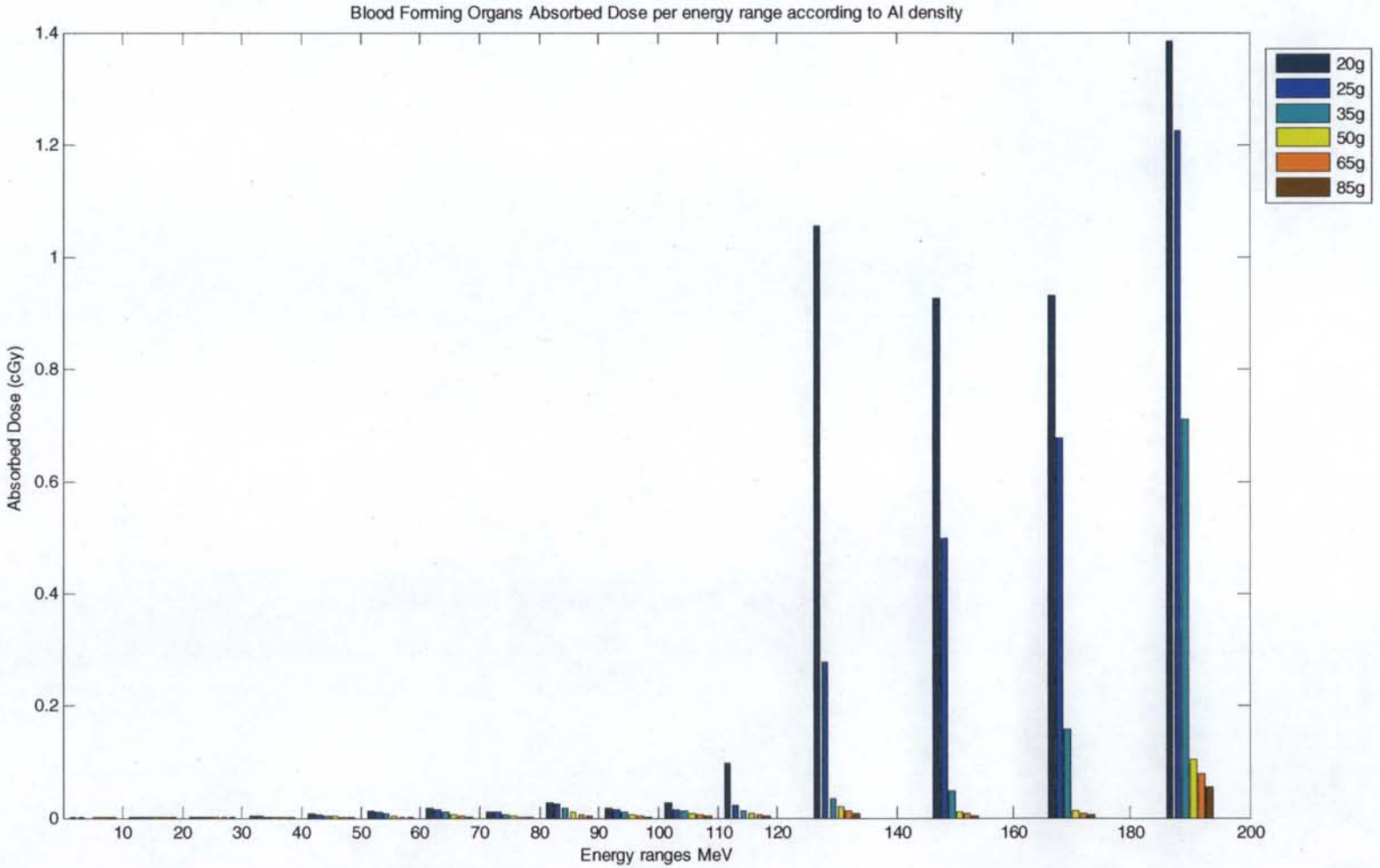

Figure 18. Blood forming organs dose equivalent per energy range per aluminum density through 85 g/cm^2

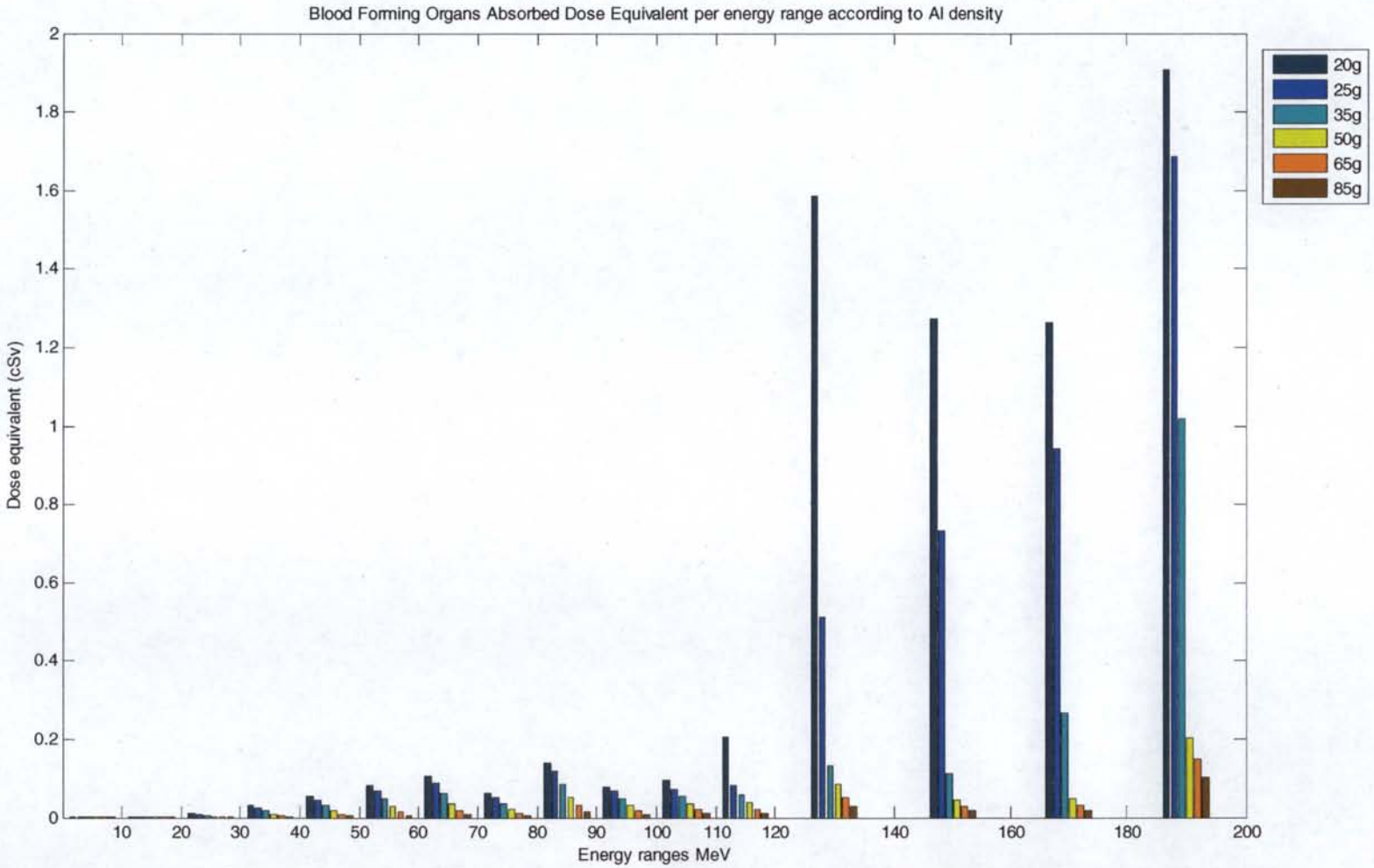

Figure 19. Skin absorbed dose per energy range per aluminum density through 85 g/cm^2

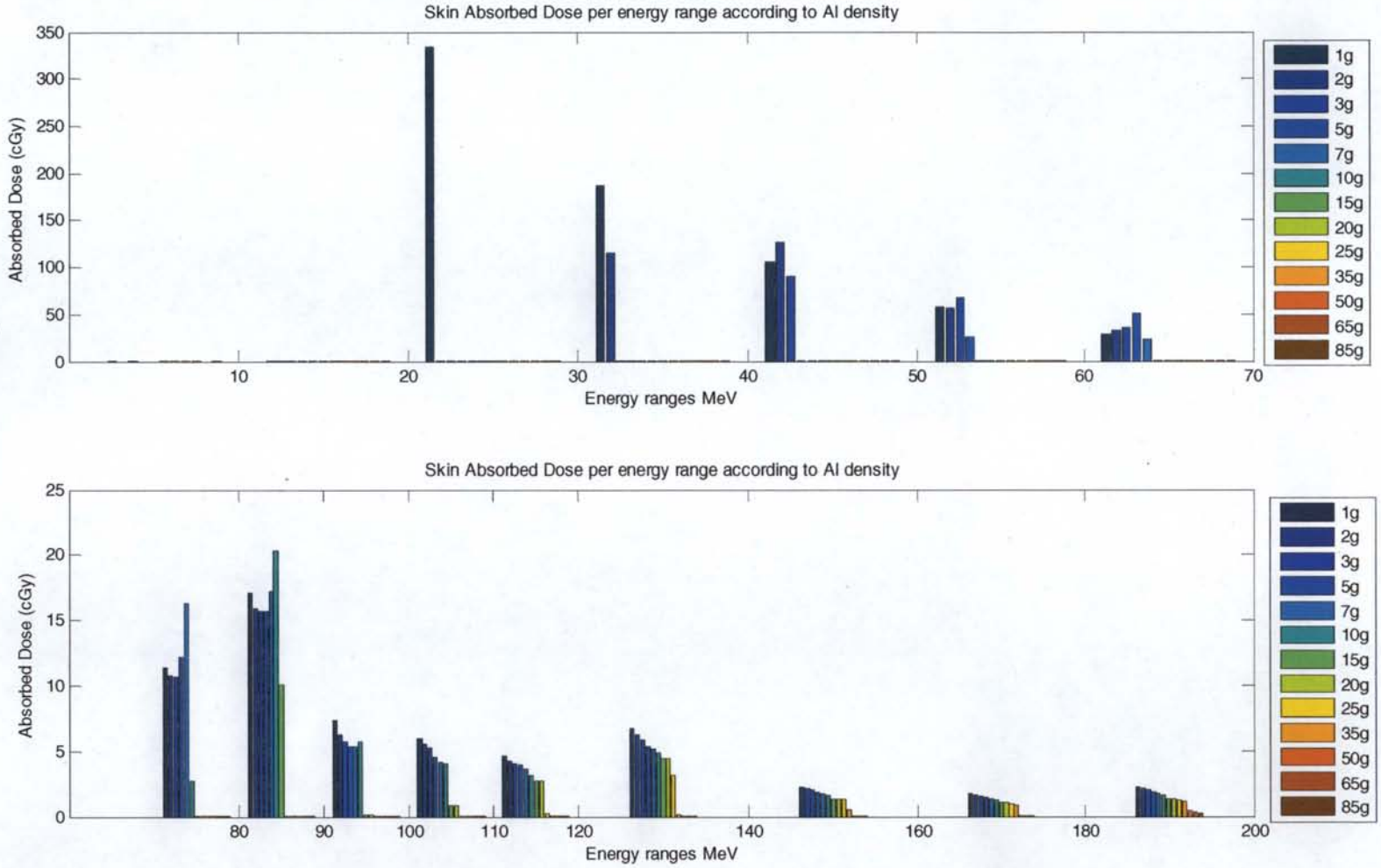

Figure 20. Skin dose equivalent per energy range per aluminum density through 85 g/cm^2

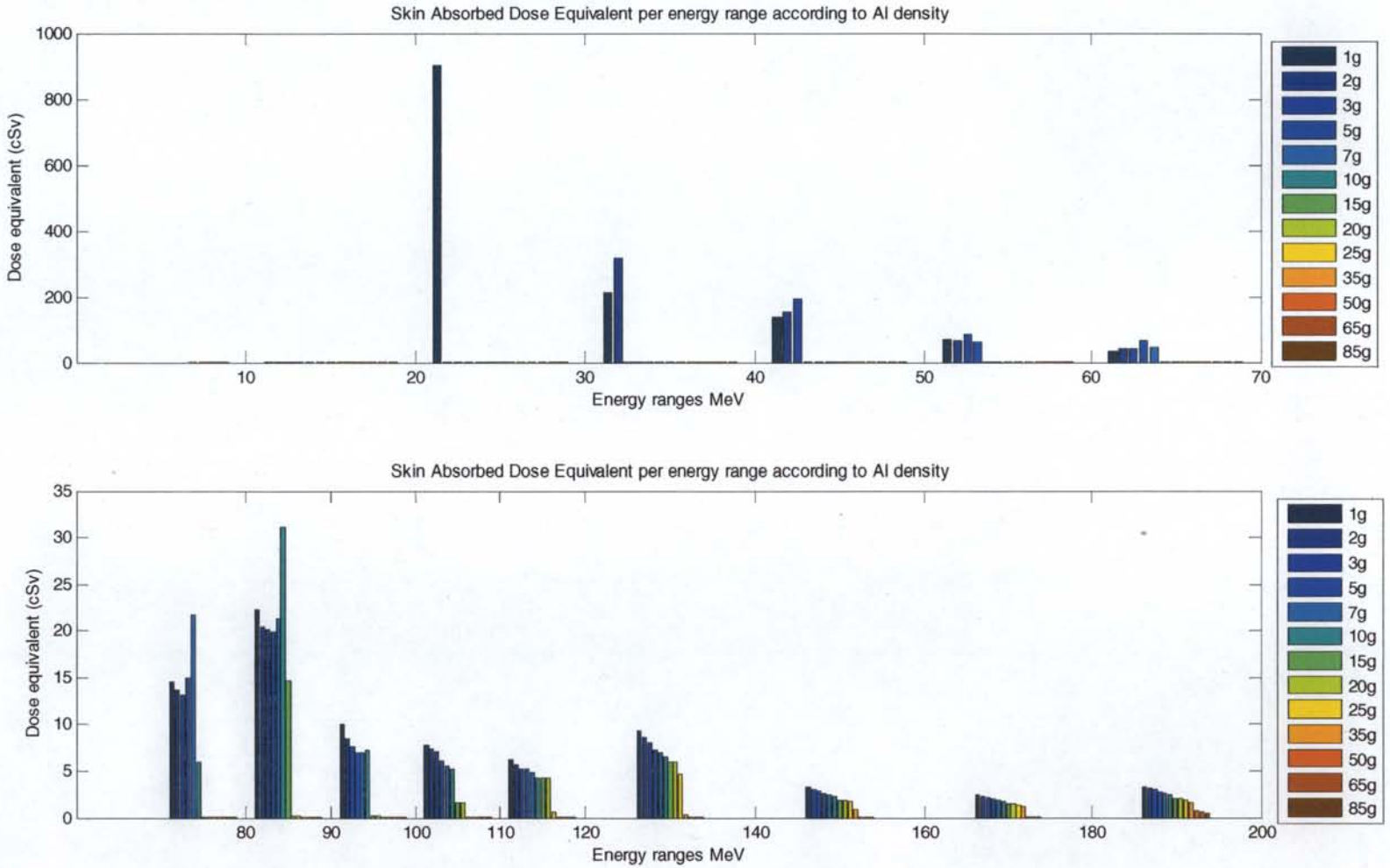

Figure 21. Skin absorbed dose per energy range per aluminum density through 85 g/cm^2

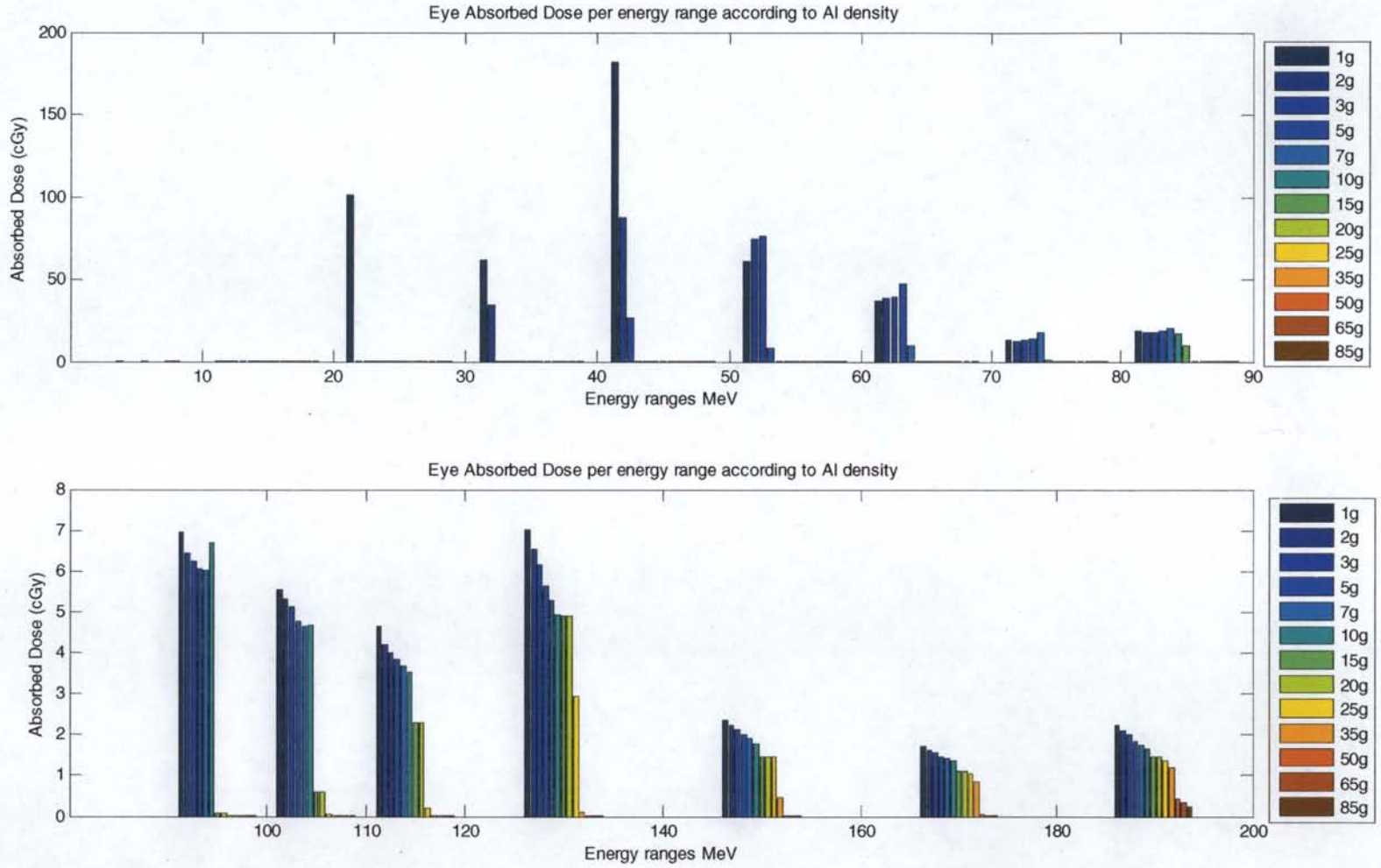

Figure 22. Skin dose equivalent per energy range per aluminum density through 85 g/cm^2

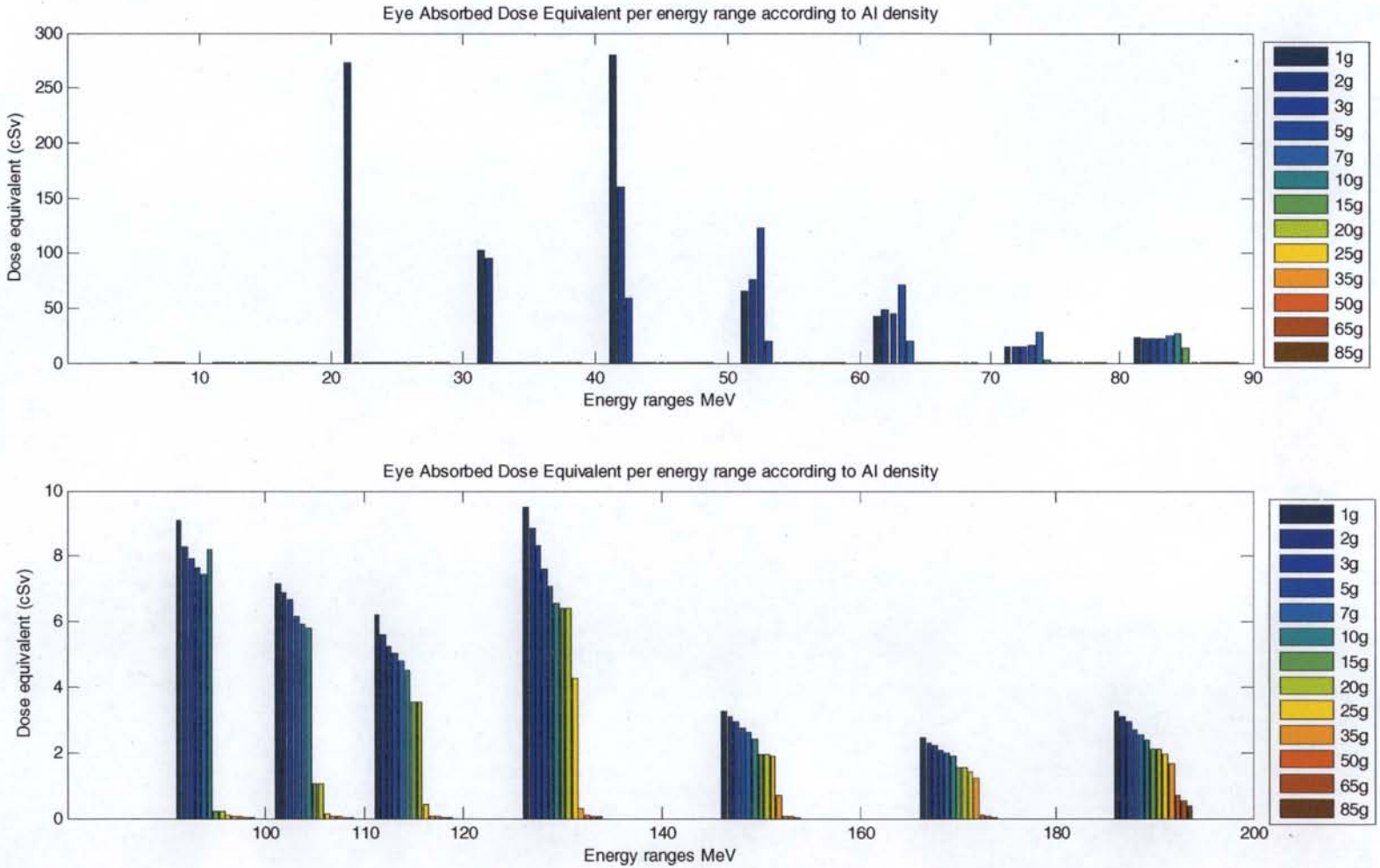

Figure 23. Skin absorbed dose per energy range per aluminum density through 15 g/cm^2

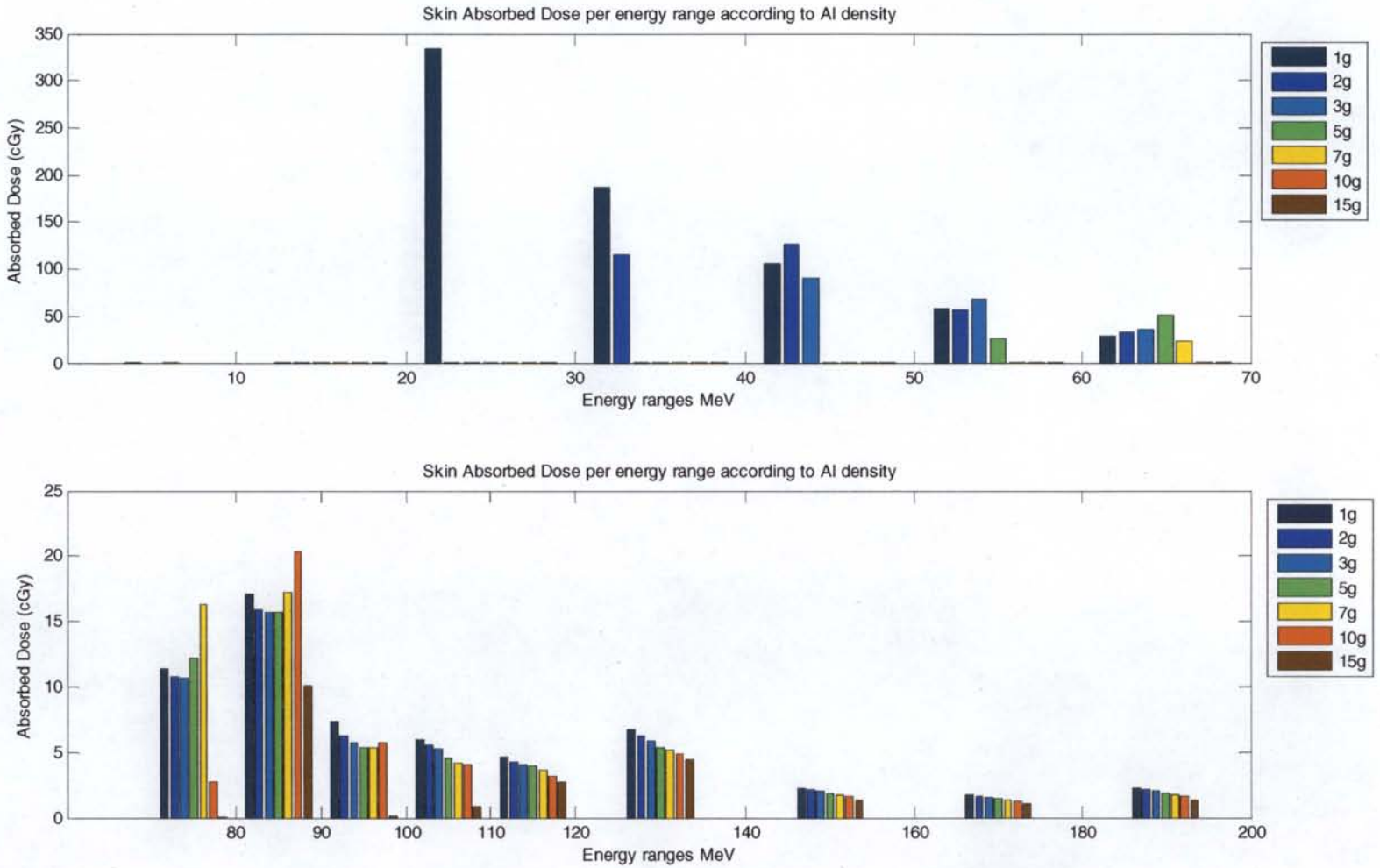

Figure 24. Skin dose equivalent per energy range per aluminum density through 15 g/cm^2

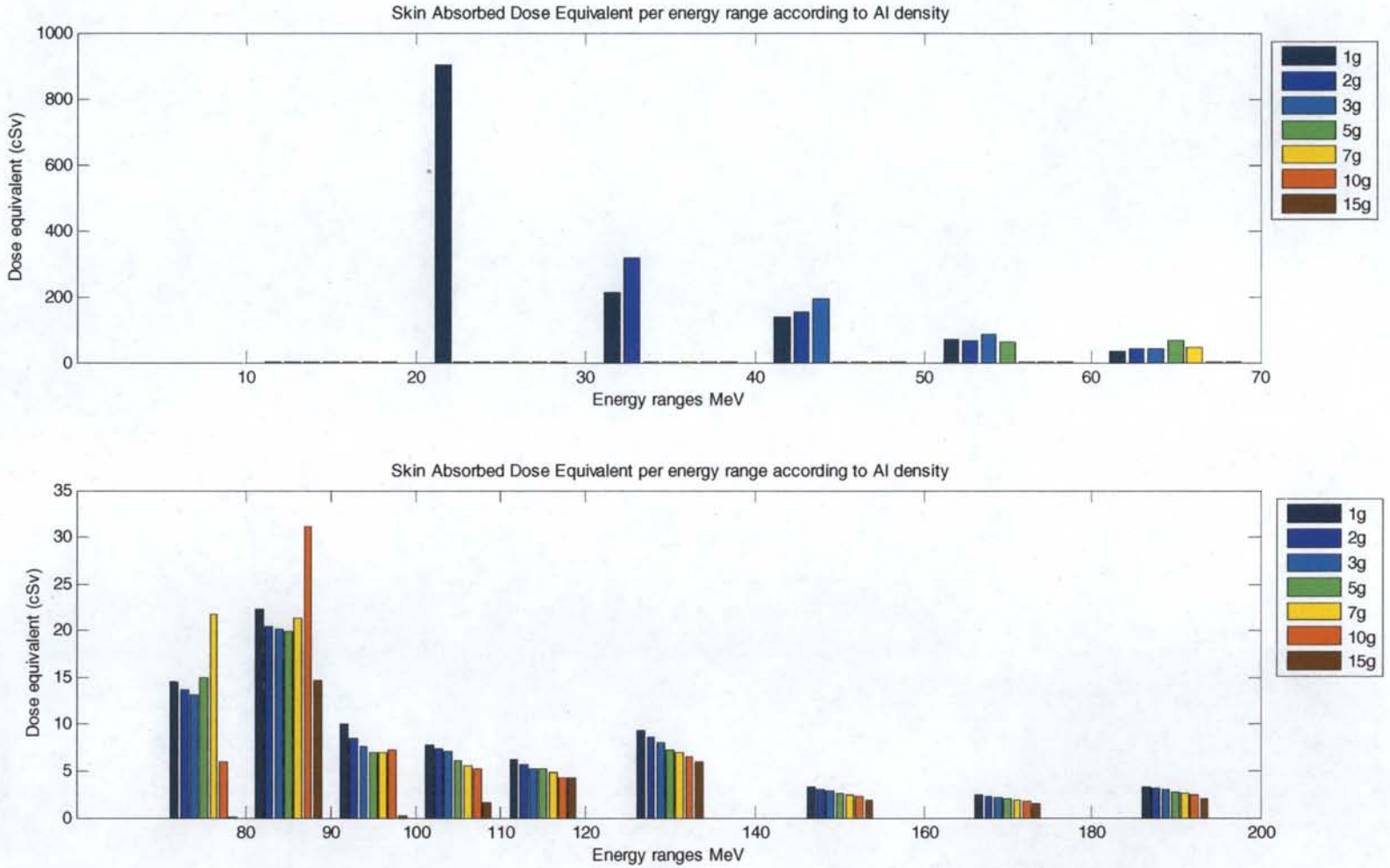

Figure 25. Eye absorbed dose per energy range per aluminum density through 15 g/cm^2

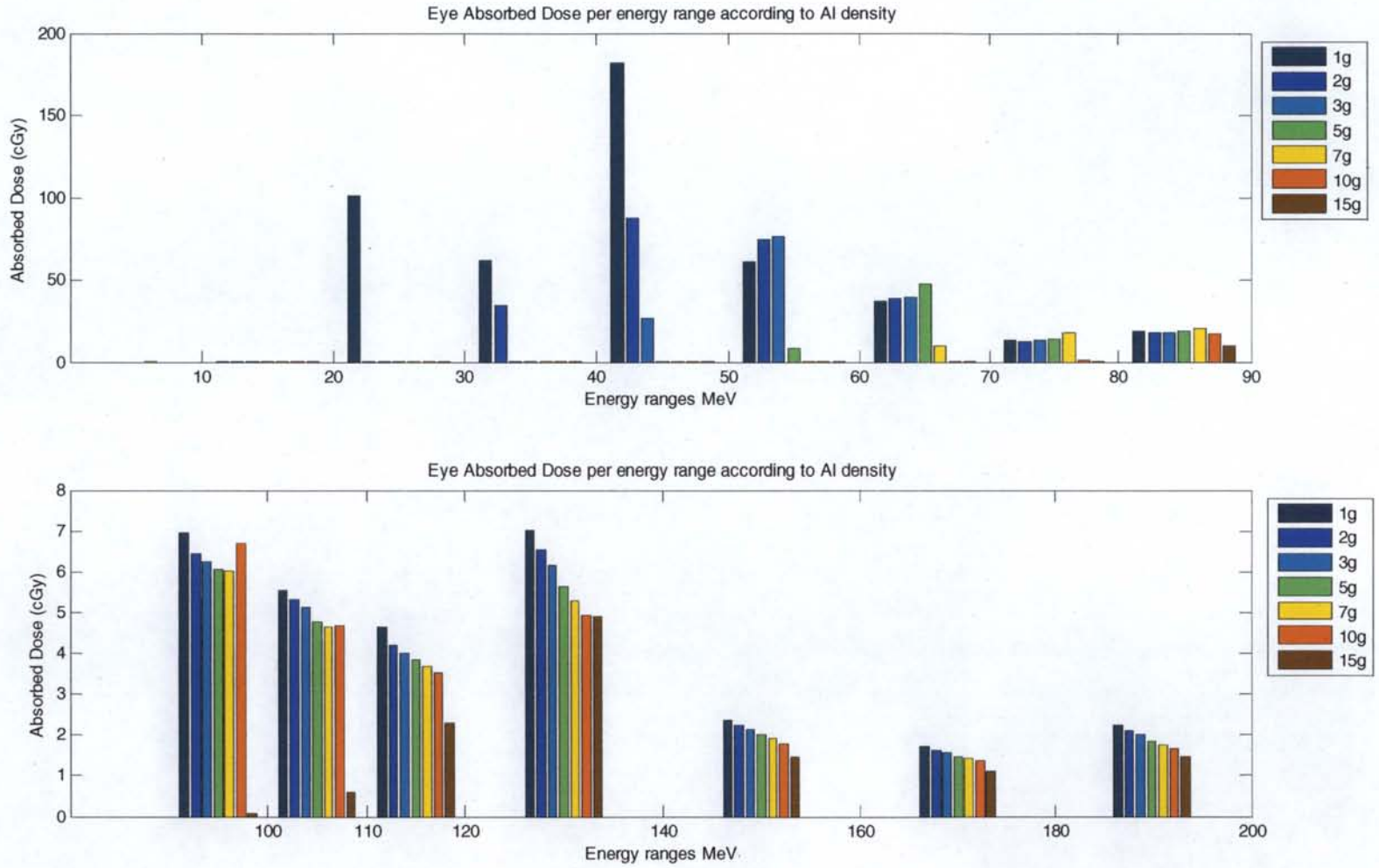

Figure 26. Eye dose equivalent per energy range per aluminum density through 15 g/cm^2

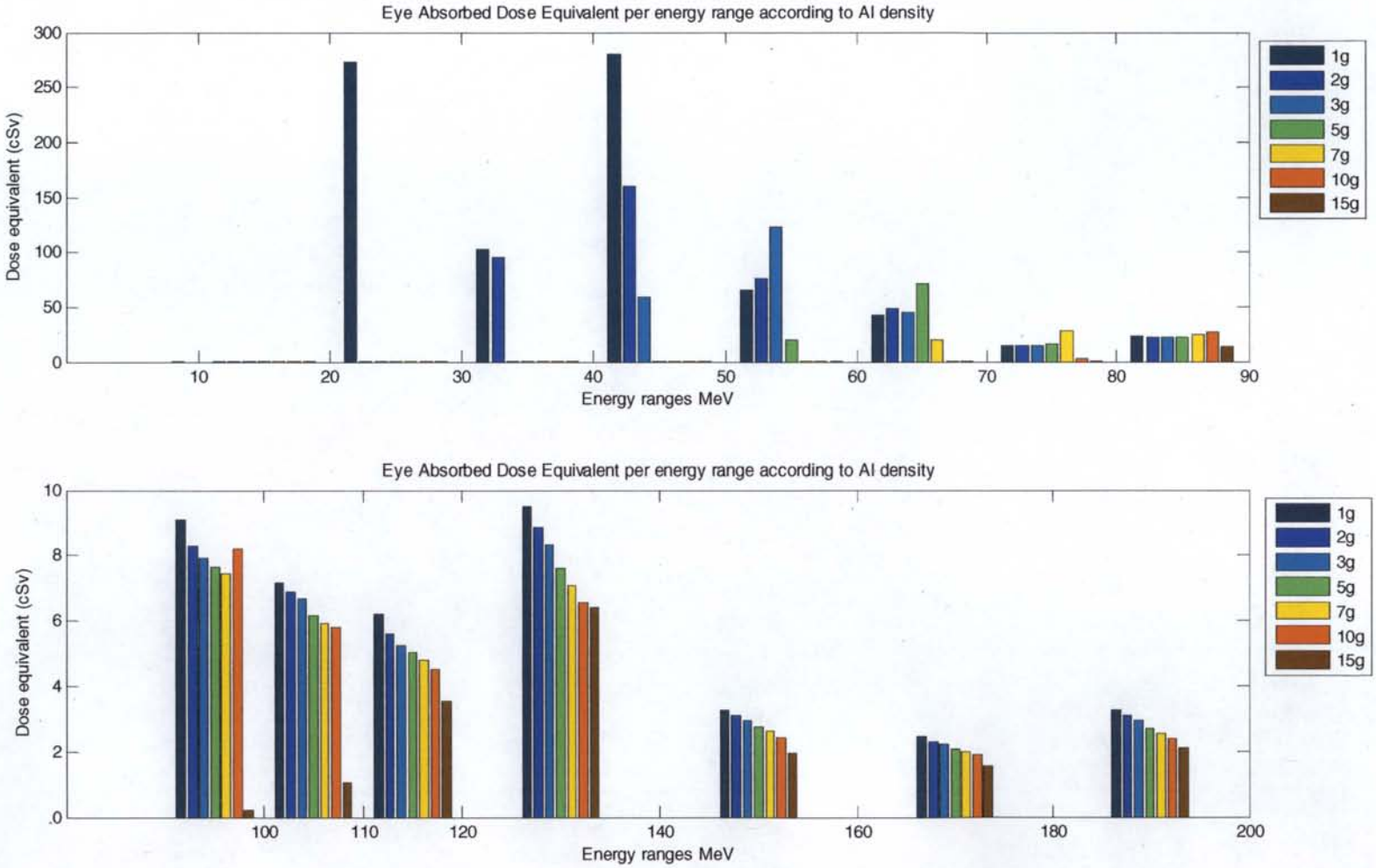

8.4 MATLAB CODE

```
% Caleb Bastian - NE 598

clc;
clear all;

max1=110;

% load data
load('g1');
load('g2');
load('g3');
load('g5');
load('g7');
load('g10');
load('g15');
load('g20');
load('g25');
load('g35');
load('g50');
load('g65');
load('g85');


ind_dose=[2 5 8];
ind_doseq=[3 6 9];
ticks=[10:10:max1 120:20:200];
energies=[5:10:(max1-5) 115 130:20:190]; %[0 10 20 30 40 50 60 70 80];


% Get doses by Al density
skindose=horzcat(g1(:,2),g2(:,2),g3(:,2),g5(:,2),g7(:,2),g10(:,2),g15(:,2)...
    ,g20(:,2),g25(:,2),g35(:,2),g50(:,2),g65(:,2),g85(:,2) );

skindose_eq=horzcat(g1(:,3),g2(:,3),g3(:,3),g5(:,3),g7(:,3),g10(:,3),g15(:,3)...
    ,g20(:,3),g25(:,3),g35(:,3),g50(:,3),g65(:,3),g85(:,3));

skin_QF = horzcat(g1(:,4),g2(:,4),g3(:,4),g5(:,4),g7(:,4),g10(:,4),g15(:,4)...
    ,g20(:,4),g25(:,4),g35(:,4),g50(:,4),g65(:,4),g85(:,4));

eyedose=horzcat(g1(:,5),g2(:,5),g3(:,5),g5(:,5),g7(:,5),g10(:,5),g15(:,5)...
    ,g20(:,5),g25(:,5),g35(:,5),g50(:,5),g65(:,5),g85(:,5));

eyedose_eq=horzcat(g1(:,6),g2(:,6),g3(:,6),g5(:,6),g7(:,6),g10(:,6),g15(:,6)...
    ,g20(:,6),g25(:,6),g35(:,6),g50(:,6),g65(:,6),g85(:,6));

eye_QF = horzcat(g1(:,7),g2(:,7),g3(:,7),g5(:,7),g7(:,7),g10(:,7),g15(:,7)...
```

```
    ,g20(:,7),g25(:,7),g35(:,7),g50(:,7),g65(:,7),g85(:,7));

BFOdose=horzcat(g1(:,8),g2(:,8),g3(:,8),g5(:,8),g7(:,8),g10(:,8),g15(:,8)...
    ,g20(:,8),g25(:,8),g35(:,8),g50(:,8),g65(:,8),g85(:,8));

BFOdose_eq=horzcat(g1(:,9),g2(:,9),g3(:,9),g5(:,9),g7(:,9),g10(:,9),g15(:,9)...
    ,g20(:,9),g25(:,9),g35(:,9),g50(:,9),g65(:,9),g85(:,9));

BFO_QF = horzcat(g1(:,10),g2(:,10),g3(:,10),g5(:,10),g7(:,10),g10(:,10),g15(:,10)...
    ,g20(:,10),g25(:,10),g35(:,10),g50(:,10),g65(:,10),g85(:,10));


% doses in the energy ranges across the Al densities (from the energy the
% calculation was run at to 2500 MeV)
for ii=2:1:length((skindose(:,1)))
    skin_dose(ii-1,:)=skindose(1,:)-skindose(ii,:);
    skin_dose_eq(ii-1,:)=skindose_eq(1,:)-skindose_eq(ii,:);
    eye_dose(ii-1,:)=eyedose(1,:)-eyedose(ii,:);
    eye_dose_eq(ii-1,:)=eyedose_eq(1,:)-eyedose_eq(ii,:);
    BFO_dose(ii-1,:)=BFOdose(1,:)-BFOdose(ii,:);
    BFO_dose_eq(ii-1,:)=BFOdose_eq(1,:)-BFOdose_eq(ii,:);
end

% Get quality factors
for ii=2:1:length((skin_QF(:,1)))
    skinQF(ii-1,:)=(skin_QF(ii-1,:)+skin_QF(ii,:))/2;
    eyeQF(ii-1,:)=(eye_QF(ii-1,:)+eye_QF(ii,:))/2;
    BFOQF(ii-1,:)=(BFO_QF(ii-1,:)+BFO_QF(ii,:))/2;
end
% Gets the actual doses in the energy ranges
% 0 < E < 10
sd(1,:)=skin_dose(1,:);
sdeq(1,:)=skin_dose_eq(1,:);
ed(1,:)=eye_dose(1,:);
edeq(1,:)=eye_dose_eq(1,:);
BFOd(1,:)=BFO_dose(1,:);
BFOdeq(1,:)=BFO_dose_eq(1,:);

for ii=2:1:length(skin_dose(:,1))
    sd(ii,:)=skin_dose(ii,:)-skin_dose(ii-1,:);
    sdeq(ii,:)=skin_dose_eq(ii,:)-skin_dose_eq(ii-1,:);
    ed(ii,:)=eye_dose(ii,:)-eye_dose(ii-1,:);
    edeq(ii,:)=eye_dose_eq(ii,:)-eye_dose_eq(ii-1,:);
    BFOd(ii,:)=BFO_dose(ii,:)-BFO_dose(ii-1,:);
    BFOdeq(ii,:)=BFO_dose_eq(ii,:)-BFO_dose_eq(ii-1,:);

end
```

```
%percentage contribution
for ii=1:1:13
    sum_sd=sum(sd(:,ii));
    sd_perc(:,ii)=sd(:,ii)./sum_sd;
    sum_sdeq=sum(sdeq(:,ii));
    sdeq_perc(:,ii)=sdeq(:,ii)./sum_sdeq;

    sum_ed=sum(ed(:,ii));
    ed_perc(:,ii)=ed(:,ii)./sum_ed;
    sum_edeq=sum(edeq(:,ii));
    edeq_perc(:,ii)=edeq(:,ii)./sum_edeq;

    sum_BFOd=sum(BFOd(:,ii));
    BFOd_perc(:,ii)=BFOd(:,ii)./sum_BFOd;
    sum_BFOdeq=sum(BFOdeq(:,ii));
    BFOdeq_perc(:,ii)=BFOdeq(:,ii)./sum_BFOdeq;
end



% Graph the doses according to energy range
figure(1);
bar(energies,abs(sd))
title('Skin Absorbed Dose per energy range according to Al density')
set(gca,'xtick',ticks)
xlabel('Energy ranges MeV'); ylabel('Absorbed Dose (cGy)');
legend('1g','2g','3g','5g','7g','10g','15g','20g','25g','35g','50g'...
    ,'65g','85g','100g','125g','150g','200g','225g','250g',-1);

figure(2);
bar(energies,abs(sdeq))
title('Skin Absorbed Dose Equivalent per energy range according to Al density')
set(gca,'xtick',ticks)
xlabel('Energy ranges MeV'); ylabel('Dose equivalent (cSv)');
legend('1g','2g','3g','5g','7g','10g','15g','20g','25g','35g','50g'...
    ,'65g','85g','100g','125g','150g','200g','225g','250g',-1);
figure(3);
bar(energies,abs(ed))
title('Eye Absorbed Dose per energy range according to Al density')
set(gca,'xtick',ticks)
xlabel('Energy ranges MeV'); ylabel('Absorbed Dose (cGy)');
legend('1g','2g','3g','5g','7g','10g','15g','20g','25g','35g','50g'...
    ,'65g','85g','100g','125g','150g','200g','225g','250g',-1);

figure(4);
bar(energies,abs(edeq))
```

```
title('Eye Absorbed Dose Equivalent per energy range according to Al density')
set(gca,'xtick',ticks)
xlabel('Energy ranges MeV'); ylabel('Dose equivalent (cSv)');
legend('1g','2g','3g','5g','7g','10g','15g','20g','25g','35g','50g'...
    ,'65g','85g','100g','125g','150g','200g','225g','250g',-1);

figure(5);
bar(energies,abs(BFOd))
title('Blood Forming Organs Absorbed Dose per energy range according to Al density')
set(gca,'xtick',ticks)
xlabel('Energy ranges MeV'); ylabel('Absorbed Dose (cGy)');
legend('1g','2g','3g','5g','7g','10g','15g','20g','25g','35g','50g'...
    ,'65g','85g','100g','125g','150g','200g','225g','250g',-1);

figure(6);
bar(energies,abs(BFOdeq))
title('Blood Forming Organs Absorbed Dose Equivalent per energy range according to Al
density')
set(gca,'xtick',ticks)
xlabel('Energy ranges MeV'); ylabel('Dose equivalent (cSv)');
legend('1g','2g','3g','5g','7g','10g','15g','20g','25g','35g','50g'...
    ,'65g','85g','100g','125g','150g','200g','225g','250g',-1);

figure(7);
bar(energies,abs(sd(:,1:7)))
title('Skin Absorbed Dose per energy range according to Al density')
set(gca,'xtick',ticks)
xlabel('Energy ranges MeV');ylabel('Absorbed Dose (cGy)');
legend('1g','2g','3g','5g','7g','10g','15g','20g','25g','35g','50g'...
    ,'65g','85g','100g','125g','150g','200g','225g','250g',-1);

figure(8);
bar(energies,abs(sdeq(:,1:7)))
title('Skin Absorbed Dose Equivalent per energy range according to Al density')
set(gca,'xtick',ticks)
xlabel('Energy ranges MeV'); ylabel('Dose equivalent (cSv)');
legend('1g','2g','3g','5g','7g','10g','15g','20g','25g','35g','50g'...
    ,'65g','85g','100g','125g','150g','200g','225g','250g',-1);
figure(9);
bar(energies,abs(ed(:,1:7)))
title('Eye Absorbed Dose per energy range according to Al density')
set(gca,'xtick',ticks)
xlabel('Energy ranges MeV'); ylabel('Absorbed Dose (cGy)');
legend('1g','2g','3g','5g','7g','10g','15g','20g','25g','35g','50g'...
    ,'65g','85g','100g','125g','150g','200g','225g','250g',-1);

figure(10);
```

```
bar(energies,abs(edeq(:,1:7)))
title('Eye Absorbed Dose Equivalent per energy range according to Al density')
set(gca,'xtick',ticks)
xlabel('Energy ranges MeV'); ylabel('Dose equivalent (cSv)');
legend('1g','2g','3g','5g','7g','10g','15g','20g','25g','35g','50g'...
    ,'65g','85g','100g','125g','150g','200g','225g','250g',-1);

figure(11);
bar(energies,abs(BFOd(:,1:7)))
title('Blood Forming Organs Absorbed Dose per energy range according to Al density')
set(gca,'xtick',ticks)
xlabel('Energy ranges MeV'); ylabel('Absorbed Dose (cGy)');
legend('1g','2g','3g','5g','7g','10g','15g','20g','25g','35g','50g'...
    ,'65g','85g','100g','125g','150g','200g','225g','250g',-1);

figure(12);
bar(energies,abs(BFOdeq(:,1:7)))
title('Blood Forming Organs Absorbed Dose Equivalent per energy range according to Al
density')
set(gca,'xtick',ticks)
xlabel('Energy ranges MeV'); ylabel('Dose equivalent (cSv)');
legend('1g','2g','3g','5g','7g','10g','15g','20g','25g','35g','50g'...
    ,'65g','85g','100g','125g','150g','200g','225g','250g',-1);
figure(13);
bar(energies,abs(sd(:,8:13)))
title('Skin Absorbed Dose per energy range according to Al density')
set(gca,'xtick',ticks)
xlabel('Energy ranges MeV'); ylabel('Absorbed Dose (cGy)');
%legend('1g','2g','3g','5g','7g','10g','15g',...
legend('20g','25g','35g','50g','65g','85g',-1);
%,'100g','125g','150g','200g','225g','250g');

figure(14);
bar(energies,abs(sdeq(:,8:13)))
title('Skin Absorbed Dose Equivalent per energy range according to Al density')
set(gca,'xtick',ticks)
xlabel('Energy ranges MeV');ylabel('Dose equivalent (cSv)');
%legend('1g','2g','3g','5g','7g','10g','15g',...
legend('20g','25g','35g','50g','65g','85g',-1);
%,'100g','125g','150g','200g','225g','250g');
figure(15);
bar(energies,abs(ed(:,8:13)))
title('Eye Absorbed Dose per energy range according to Al density')
set(gca,'xtick',ticks)
xlabel('Energy ranges MeV'); ylabel('Absorbed Dose (cGy)');
%legend('1g','2g','3g','5g','7g','10g','15g',...
```

```
legend('20g','25g','35g','50g','65g','85g',-1);
%,'100g','125g','150g','200g','225g','250g');

figure(16);
bar(energies,abs(edeq(:,8:13)))
title('Eye Absorbed Dose Equivalent per energy range according to Al density')
set(gca,'xtick',ticks)
xlabel('Energy ranges MeV'); ylabel('Dose equivalent (cSv)');
%legend('1g','2g','3g','5g','7g','10g','15g',...
legend('20g','25g','35g','50g','65g','85g',-1);
%,'100g','125g','150g','200g','225g','250g');

figure(17);
bar(energies,abs(BFOd(:,8:13)))
title('Blood Forming Organs Absorbed Dose per energy range according to Al density')
set(gca,'xtick',ticks)
xlabel('Energy ranges MeV'); ylabel('Absorbed Dose (cGy)');
%legend('1g','2g','3g','5g','7g','10g','15g',...
legend('20g','25g','35g','50g','65g','85g',-1);
%,'100g','125g','150g','200g','225g','250g');

figure(18);
bar(energies,abs(BFOdeq(:,8:13)))
title('Blood Forming Organs Absorbed Dose Equivalent per energy range according to Al
density')
set(gca,'xtick',ticks)
xlabel('Energy ranges MeV'); ylabel('Dose equivalent (cSv)');
%legend('1g','2g','3g','5g','7g','10g','15g',...
legend('20g','25g','35g','50g','65g','85g',-1);
%,'100g','125g','150g','200g','225g','250g');

figure(19);
subplot(2,1,1);
bar(energies(1:7),abs(sd(1:7,:)))
title('Skin Absorbed Dose per energy range according to Al density')
set(gca,'xtick',ticks(1:7))
xlabel('Energy ranges MeV'); ylabel('Absorbed Dose (cGy)');
legend('1g','2g','3g','5g','7g','10g','15g','20g','25g','35g','50g'...
    ,'65g','85g','100g','125g','150g','200g','225g','250g',-1);
subplot(2,1,2);
bar(energies(8:16),abs(sd(8:16,:)))
title('Skin Absorbed Dose per energy range according to Al density')
set(gca,'xtick',ticks(8:16))
xlabel('Energy ranges MeV'); ylabel('Absorbed Dose (cGy)');
legend('1g','2g','3g','5g','7g','10g','15g','20g','25g','35g','50g'...
    ,'65g','85g','100g','125g','150g','200g','225g','250g',-1);
```

```
figure(20);
subplot(2,1,1);
bar(energies(1:7),abs(sdeq(1:7,:)))
title('Skin Absorbed Dose Equivalent per energy range according to Al density')
set(gca,'xtick',ticks(1:7))
xlabel('Energy ranges MeV'); ylabel('Dose equivalent (cSv)');
legend('1g','2g','3g','5g','7g','10g','15g','20g','25g','35g','50g'...
    ,'65g','85g','100g','125g','150g','200g','225g','250g',-1);
subplot(2,1,2);
bar(energies(8:16),abs(sdeq(8:16,:)))
title('Skin Absorbed Dose Equivalent per energy range according to Al density')
set(gca,'xtick',ticks(8:16))
xlabel('Energy ranges MeV'); ylabel('Dose equivalent (cSv)');
legend('1g','2g','3g','5g','7g','10g','15g','20g','25g','35g','50g'...
    ,'65g','85g','100g','125g','150g','200g','225g','250g',-1);

figure(21);
subplot(2,1,1);
bar(energies(1:9),abs(ed(1:9,:)))
title('Eye Absorbed Dose per energy range according to Al density')
set(gca,'xtick',ticks(1:9))
xlabel('Energy ranges MeV');ylabel('Absorbed Dose (cGy)');
legend('1g','2g','3g','5g','7g','10g','15g','20g','25g','35g','50g'...
    ,'65g','85g','100g','125g','150g','200g','225g','250g',-1);
subplot(2,1,2);
bar(energies(10:16),abs(ed(10:16,:)))
title('Eye Absorbed Dose per energy range according to Al density')
set(gca,'xtick',ticks(10:16))
xlabel('Energy ranges MeV'); ylabel('Absorbed Dose (cGy)');
legend('1g','2g','3g','5g','7g','10g','15g','20g','25g','35g','50g'...
    ,'65g','85g','100g','125g','150g','200g','225g','250g',-1);

figure(22);
subplot(2,1,1);
bar(energies(1:9),abs(edeq(1:9,:)))
title('Eye Absorbed Dose Equivalent per energy range according to Al density')
set(gca,'xtick',ticks(1:9))
xlabel('Energy ranges MeV'); ylabel('Dose equivalent (cSv)');
legend('1g','2g','3g','5g','7g','10g','15g','20g','25g','35g','50g'...
    ,'65g','85g','100g','125g','150g','200g','225g','250g',-1);
subplot(2,1,2);
bar(energies(10:16),abs(edeq(10:16,:)))
title('Eye Absorbed Dose Equivalent per energy range according to Al density')
set(gca,'xtick',ticks(10:16))
xlabel('Energy ranges MeV'); ylabel('Dose equivalent (cSv)');
legend('1g','2g','3g','5g','7g','10g','15g','20g','25g','35g','50g'...
    ,'65g','85g','100g','125g','150g','200g','225g','250g',-1);
```

```
figure(23);
subplot(2,1,1);
bar(energies(1:7),abs(sd(1:7,1:7)))
title('Skin Absorbed Dose per energy range according to Al density')
set(gca,'xtick',ticks(1:7))
xlabel('Energy ranges MeV'); ylabel('Absorbed Dose (cGy)');
legend('1g','2g','3g','5g','7g','10g','15g','20g','25g','35g','50g'...
    ,'65g','85g','100g','125g','150g','200g','225g','250g',-1);
subplot(2,1,2);
bar(energies(8:16),abs(sd(8:16,1:7)))
title('Skin Absorbed Dose per energy range according to Al density')
set(gca,'xtick',ticks(8:16))
xlabel('Energy ranges MeV'); ylabel('Absorbed Dose (cGy)');
legend('1g','2g','3g','5g','7g','10g','15g','20g','25g','35g','50g'...
    ,'65g','85g','100g','125g','150g','200g','225g','250g',-1);

figure(24);
subplot(2,1,1);
bar(energies(1:7),abs(sdeq(1:7,1:7)))
title('Skin Absorbed Dose Equivalent per energy range according to Al density')
set(gca,'xtick',ticks(1:7))
xlabel('Energy ranges MeV'); ylabel('Dose equivalent (cSv)');
legend('1g','2g','3g','5g','7g','10g','15g','20g','25g','35g','50g'...
    ,'65g','85g','100g','125g','150g','200g','225g','250g',-1);
subplot(2,1,2);
bar(energies(8:16),abs(sdeq(8:16,1:7)))
title('Skin Absorbed Dose Equivalent per energy range according to Al density')
set(gca,'xtick',ticks(8:16))
xlabel('Energy ranges MeV'); ylabel('Dose equivalent (cSv)');
legend('1g','2g','3g','5g','7g','10g','15g','20g','25g','35g','50g'...
    ,'65g','85g','100g','125g','150g','200g','225g','250g',-1);

figure(25);
subplot(2,1,1);
bar(energies(1:9),abs(ed(1:9,1:7)))
title('Eye Absorbed Dose per energy range according to Al density')
set(gca,'xtick',ticks(1:9))
xlabel('Energy ranges MeV'); ylabel('Absorbed Dose (cGy)');
legend('1g','2g','3g','5g','7g','10g','15g','20g','25g','35g','50g'...
    ,'65g','85g','100g','125g','150g','200g','225g','250g',-1);
subplot(2,1,2);
bar(energies(10:16),abs(ed(10:16,1:7)))
title('Eye Absorbed Dose per energy range according to Al density')
set(gca,'xtick',ticks(10:16))
xlabel('Energy ranges MeV'); ylabel('Absorbed Dose (cGy)');
legend('1g','2g','3g','5g','7g','10g','15g','20g','25g','35g','50g'...
```

```
    ,'65g','85g','100g','125g','150g','200g','225g','250g',-1);

figure(26);
subplot(2,1,1);
bar(energies(1:9),abs(edeq(1:9,1:7)))
title('Eye Absorbed Dose Equivalent per energy range according to Al density')
set(gca,'xtick',ticks(1:9))
xlabel('Energy ranges MeV'); ylabel('Dose equivalent (cSv)');
legend('1g','2g','3g','5g','7g','10g','15g','20g','25g','35g','50g'...
    ,'65g','85g','100g','125g','150g','200g','225g','250g',-1);
subplot(2,1,2);
bar(energies(10:16),abs(edeq(10:16,1:7)))
title('Eye Absorbed Dose Equivalent per energy range according to Al density')
set(gca,'xtick',ticks(10:16))
xlabel('Energy ranges MeV'); ylabel('Dose equivalent (cSv)');
legend('1g','2g','3g','5g','7g','10g','15g','20g','25g','35g','50g'...
    ,'65g','85g','100g','125g','150g','200g','225g','250g',-1);
```

8.5 VARIABLES LOADED INTO MATLAB

g1.mat

0	775.75	1439.6	1.8558	507.73	847.12	1.6684	47.899	67.332	1.4057
10	775.75	1439.6	1.8558	507.73	847.12	1.6684	47.899	67.332	1.4057
20	775.75	1439.6	1.8558	507.73	847.12	1.6684	47.898	67.331	1.4057
30	441.3	536.73	1.2162	406.81	574.64	1.4126	48.044	67.707	1.4093
40	254.24	323.48	1.2723	344.5	472.59	1.3718	48.097	67.595	1.4054
50	148.79	187.36	1.2592	162.18	192.3	1.1857	47.565	66.652	1.4013
60	91.001	118.23	1.2992	101.2	126.51	1.2501	44.199	59.808	1.3532
70	61.643	82.717	1.3419	64.064	83.319	1.3006	38.616	52.256	1.3532
80	50.248	68.135	1.355	51.245	67.757	1.3222	33.88	45.564	1.3449
90	33.178	45.906	1.3836	32.572	44.378	1.3625	25.002	33.691	1.3475
100	25.789	35.907	1.3923	25.619	35.292	1.3776	19.993	26.816	1.3413
110	19.841	28.123	1.4174	20.087	28.112	1.3995	15.915	21.714	1.3644
120	15.197	21.865	1.4388	15.456	21.895	1.4166	12.38	17.02	1.3748
140	8.3916	12.508	1.4905	8.4338	12.383	1.4683	6.5347	9.3356	1.4286
160	6.088	9.267	1.5222	6.0785	9.121	1.5005	4.6253	6.7996	1.4701
180	4.3646	6.7725	1.5517	4.3578	6.6664	1.5298	3.2951	4.9568	1.5043
200	2.1115	3.4156	1.6176	2.1401	3.3964	1.5871	1.6135	2.5325	1.5695

g2.mat

0	389.3	652.65	1.6765	296.92	459.13	1.5463	39.966	56.13	1.4044
10	389.3	652.65	1.6747	296.92	459.13	1.5463	39.966	56.13	1.4044
20	389.3	652.65	1.6765	296.92	459.13	1.5463	39.966	56.129	1.4044
30	389.3	652.59	1.6763	296.92	459.08	1.5462	39.964	56.106	1.4039
40	274.19	336.35	1.2267	262.18	363.57	1.3867	40.007	56.181	1.4043
50	146.94	182.29	1.2406	174.6	203.64	1.1663	39.863	55.713	1.3796
60	89.553	116.54	1.3013	99.714	127.61	1.2798	39.217	54.474	1.389
70	57.133	76.32	1.3358	61.202	79.013	1.291	34.659	47.309	1.365
80	46.368	62.616	1.3504	48.53	63.799	1.3146	31.433	42.344	1.3471
90	30.414	42.157	1.3861	30.551	41.492	1.3581	23.574	31.79	1.3486
100	24.126	33.706	1.3971	24.104	33.19	1.3769	19.476	26.219	1.3462
110	18.529	26.292	1.419	18.795	26.293	1.399	15.329	20.866	1.3612
120	14.295	20.632	1.4433	14.589	20.698	1.4188	12.099	16.651	1.3762
140	8.0064	11.973	1.4954	8.0512	11.832	1.4696	6.4569	9.2032	1.4253
160	5.8226	8.8954	1.5277	5.8084	8.7271	1.5025	4.5355	6.6531	1.4669
180	4.1954	6.5361	1.5579	4.1754	6.4004	1.5329	3.2233	4.8448	1.5031
200	2.0462	3.3228	1.6239	2.0658	3.286	1.5906	1.5738	2.4703	1.5696

g3.mat

0	247.57	396.4	1.6011	203.37	304.24	1.496	33.936	47.678	1.4049
10	247.57	396.4	1.6011	203.37	304.24	1.496	33.936	47.678	1.4049
20	247.57	396.39	1.6011	203.37	304.24	1.496	33.936	47.677	1.4049
30	247.57	396.34	1.6009	203.37	304.2	1.4958	33.933	47.655	1.4044
40	247.56	396.23	1.6006	203.36	304.08	1.4953	33.926	47.593	1.4029
50	157.83	200.33	1.2693	176.27	244.84	1.389	33.95	47.57	1.4012
60	90.063	115.15	1.2785	99.84	121.94	1.2213	33.715	47.017	1.3745
70	54.894	72.748	1.3252	59.986	76.761	4.2796	31.082	42.395	1.364
80	44.246	59.666	1.3485	46.972	61.46	1.3084	29.001	39.485	1.3615
90	28.561	39.49	1.3827	29.228	39.56	1.3535	22.295	30.092	1.3497
100	22.785	31.865	1.3985	22.989	31.613	1.3751	18.772	25.398	1.353
110	17.521	24.803	1.4157	17.857	24.913	1.3951	14.854	20.164	1.3575
120	13.499	19.48	1.443	13.86	19.655	1.4182	11.77	16.211	1.3774
140	7.6416	11.43	1.4958	7.7062	11.319	1.4688	6.3819	9.0795	1.4227
160	5.568	8.5098	1.5283	5.5608	8.3526	1.5021	4.46	6.5258	1.4632
180	4.0263	6.2792	1.5596	4.0018	6.1382	1.5338	3.1574	4.7415	1.5017
200	1.9777	3.2152	1.6258	1.9919	3.1715	1.5922	1.537	2.4125	1.5696

g5.mat

0	130.96	200.81	1.534	115.84	168.11	1.4513	25.402	35.835	1.4107
10	130.96	200.81	1.5334	115.84	168.11	1.4513	25.402	35.835	1.4107
20	130.96	200.81	1.5334	115.84	168.11	1.4513	25.402	35.835	1.4107
30	130.96	200.76	1.5331	115.83	168.31	1.451	25.4	35.814	1.41
40	130.95	200.67	1.5324	115.82	167.97	1.4502	25.393	35.757	1.4081
50	130.93	200.51	1.5314	115.8	167.79	1.449	25.379	35.656	1.4049
60	104.63	136.99	1.3093	107.41	147.43	1.3726	25.366	35.533	1.4008
70	54.147	70.997	1.3112	59.604	75.709	1.2702	25.07	34.861	1.3705
80	41.992	56.062	1.3351	45.927	59.483	1.2952	24.004	32.975	1.3737
90	26.271	36.172	1.3769	27.471	36.966	1.3456	19.815	26.919	1.3585
100	20.886	29.153	1.3958	21.422	29.315	1.3685	17.043	23.156	1.3587
110	16.324	23.037	1.4112	16.648	23.139	1.3899	14.064	19.133	1.3604
120	12.39	17.791	1.4359	12.801	18.094	1.4134	11.061	15.213	1.3753
140	7.0296	10.493	1.4928	7.1626	10.489	1.4644	6.2193	8.8194	1.4181
160	5.1321	7.8283	1.5254	5.1594	7.7292	1.4981	4.3465	6.3252	1.4552
180	3.7163	5.7942	1.5592	3.6986	5.6708	1.5332	3.0414	4.5567	1.4982
200	1.8451	3.0007	1.6263	1.8528	2.9532	1.5939	1.471	2.3086	1.5694

g7.mat

0	81.903	123.16	1.5038	75.294	107.93	1.4335	19.69	27.397	1.4206
10	81.903	123.16	1.5038	75.293	107.93	1.4335	19.69	27.973	1.4206
20	81.902	123.16	1.5037	75.293	107.93	1.4335	19.69	27.972	1.4206
30	81.899	123.12	1.5033	75.29	107.89	1.433	19.688	27.953	1.4198
40	81.889	123.03	1.5024	75.279	107.8	1.432	19.682	27.9	1.4176
50	81.873	122.88	1.5009	75.259	107.64	1.4302	19.669	27.806	1.4317
60	81.8	122.55	1.4982	75.213	107.38	1.4277	19.648	27.671	1.4083
70	58.339	76.999	1.3083	65.082	87.095	1.3382	19.614	27.493	1.4017
80	42.073	55.34	1.3153	46.797	59.362	1.274	19.465	27.16	1.3953
90	24.888	34.093	1.3698	26.425	35.214	1.3326	17.35	23.805	1.3721
100	19.555	27.201	1.391	20.391	27.752	1.361	15.335	20.948	1.366
110	15.37	21.677	1.4104	15.755	21.824	1.3852	13.027	17.816	1.3676
120	11.747	16.788	1.4291	12.084	17.015	1.4081	10.47	14.372	1.3727
140	6.5996	9.8171	1.4875	6.7897	9.9073	1.4592	6.0496	8.5513	1.4135
160	4.8132	7.3169	1.5202	4.8812	7.2854	1.4925	4.2615	6.1721	1.4483
180	3.4643	5.3914	1.5562	3.4661	5.3035	1.5301	2.9452	4.398	1.4933
200	1.7263	2.8058	1.6253	1.7311	2.7605	1.5946	1.414	2.2181	1.5687

g10.mat

0	47.344	70.429	1.4876	44.939	64.16	1.4277	14.046	20.232	1.4404
10	47.344	70.429	1.4876	44.939	64.16	1.4277	14.046	20.232	1.4404
20	47.343	70.427	1.4876	44.939	64.158	1.4277	14.046	20.231	1.4403
30	47.34	70.389	1.4869	44.935	64.125	1.427	14.045	20.215	1.4393
40	47.332	70.308	1.4854	44.953	64.04	1.4255	14.039	20.168	1.4366
50	47.317	70.178	1.4832	44.908	63.898	1.4229	14.028	20.084	1.4318
60	47.294	70.002	1.4802	44.879	63.703	1.4194	14.009	19.963	1.4251
70	47.127	69.472	1.4714	44.793	63.356	1.4144	13.983	19.813	1.417
80	44.393	63.561	1.4318	43.616	60.834	1.3947	13.966	19.726	1.4124
90	24.03	32.441	1.35	26.199	34.359	1.3115	13.621	19.017	1.3962
100	18.302	25.252	1.3798	19.488	26.164	1.3426	12.729	17.617	1.384
110	14.19	19.924	1.4041	14.808	20.35	1.3743	11.294	15.562	1.3779
120	10.982	15.656	1.4256	11.293	15.822	1.4011	9.5185	13.133	1.3797
140	6.1412	9.0926	1.4806	6.3683	9.2591	1.4539	5.7639	8.1313	1.4107
160	4.4795	6.7776	1.513	4.5877	6.8143	1.4854	4.1317	5.9503	1.4402
180	3.1985	4.9561	1.5495	3.2284	4.9181	1.5234	2.8376	4.2092	1.4834
200	1.5818	2.5663	1.6224	1.586	2.5286	1.5943	1.3413	2.1016	1.5668

g15.mat

0	47.344	70.429	1.4876	44.939	64.16	1.4277	14.046	20.232	1.4404
10	47.344	70.429	1.4876	44.939	64.16	1.4277	14.046	20.232	1.4404
20	47.343	70.427	1.4876	44.939	64.158	1.4277	14.046	20.231	1.4403
30	47.34	70.389	1.4869	44.935	64.125	1.427	14.045	20.215	1.4393
40	47.332	70.308	1.4854	44.953	64.04	1.4255	14.039	20.168	1.4366
50	47.317	70.178	1.4832	44.908	63.898	1.4229	14.028	20.084	1.4318
60	47.294	70.002	1.4802	44.879	63.703	1.4194	14.009	19.963	1.4251
70	47.127	69.472	1.4714	44.793	63.356	1.4144	13.983	19.813	1.417
80	44.393	63.561	1.4318	43.616	60.834	1.3947	13.966	19.726	1.4124
90	24.03	32.441	1.35	26.199	34.359	1.3115	13.621	19.017	1.3962
100	18.302	25.252	1.3798	19.488	26.164	1.3426	12.729	17.617	1.384
110	14.19	19.924	1.4041	14.808	20.35	1.3743	11.294	15.562	1.3779
120	10.982	15.656	1.4256	11.293	15.822	1.4011	9.5185	13.133	1.3797
140	6.1412	9.0926	1.4806	6.3683	9.2591	1.4539	5.7639	8.1313	1.4107
160	4.4795	6.7776	1.513	4.5877	6.8143	1.4854	4.1317	5.9503	1.4402
180	3.1985	4.9561	1.5495	3.2284	4.9181	1.5234	2.8376	4.2092	1.4834
200	1.5818	2.5663	1.6224	1.586	2.5286	1.5943	1.3413	2.1016	1.5668

g20.mat

0	13.442	20.409	1.5183	13.314	19.641	1.4752	5.6856	8.7105	1.532
10	13.442	20.409	1.5183	13.314	19.641	1.4752	5.6856	8.7105	1.532
20	13.442	20.407	1.5182	13.314	19.64	1.4751	5.6855	8.7101	1.532
30	13.44	20.382	1.5166	13.312	19.618	1.4737	5.6844	8.6991	1.5303
40	13.434	20.328	1.5132	13.306	19.561	1.4701	5.6807	8.6677	1.5258
50	13.424	20.24	1.5077	13.293	19.465	1.4643	5.6728	8.6109	1.5179
60	13.409	20.119	1.5005	13.274	19.331	1.4563	5.6598	8.5276	1.5067
70	13.388	19.974	1.4919	13.248	19.169	1.4469	5.6418	8.4228	1.4929
80	13.375	19.892	1.4873	13.233	19.079	1.4417	5.6306	8.3621	1.4851
90	13.341	19.701	1.4767	13.195	18.873	1.4303	5.6026	8.2217	1.4675
100	13.23	19.425	1.4682	13.121	18.667	1.4227	5.5855	8.1419	1.4577
110	12.351	17.802	1.4413	12.534	17.603	1.4044	5.5592	8.0447	1.4471
120	9.5972	13.447	1.4011	10.236	14.056	1.3732	5.4623	7.8369	1.4347
140	5.1515	7.5103	1.4579	5.3449	7.6491	1.4311	4.4067	6.2503	1.4184
160	3.7617	5.605	1.49	3.8875	5.7021	1.4668	3.4809	4.9776	1.4299
180	2.6806	4.0976	1.5286	2.7674	4.1585	1.5027	2.5489	3.7157	1.4578
200	1.2928	2.0832	1.6114	1.2997	2.0645	1.5885	1.1637	1.8079	1.5536

g25.mat

0	8.3731	13.028	1.556	8.3736	12.713	1.5182	3.9064	6.205	1.5884
10	8.3731	13.028	1.556	8.3736	12.713	1.5182	3.9064	6.205	1.5884
20	8.373	13.027	1.5558	8.3735	12.712	1.5181	3.9064	6.2048	1.5884
30	8.3712	13.007	1.5537	8.3718	12.694	1.5163	3.9055	6.1957	1.5864
40	8.3668	12.962	1.5492	8.3667	12.647	1.5116	3.9025	6.17	1.581
50	8.3584	12.889	1.5421	8.3564	12.568	1.504	3.896	6.1232	1.5717
60	8.3454	12.789	1.5325	8.3403	12.457	1.4936	3.8852	6.0541	1.5583
70	8.328	12.668	1.5211	8.3191	12.322	1.4812	3.8701	5.9666	1.5417
80	8.3175	12.599	1.5148	8.3063	12.246	1.4743	3.8606	5.9154	1.5322
90	8.292	12.444	1.5008	8.2758	12.075	1.459	3.8368	5.7963	1.5107
100	8.2759	12.357	1.4931	8.2576	11.979	1.4507	3.8225	5.7285	1.4986
110	8.2338	12.22	1.4841	8.2226	11.853	1.4415	3.8065	5.6556	1.4858
120	7.9381	11.645	1.467	8.0108	11.436	1.4276	3.7853	5.5725	1.4721
140	4.8066	6.9265	1.441	5.0871	7.1683	1.4091	3.5064	5.0596	1.443
160	3.4846	5.1556	1.4795	3.6167	5.2551	1.453	3.0075	4.328	1.4391
180	2.4926	3.7817	1.5172	2.5757	3.847	1.4936	2.3286	3.3866	1.4543
200	1.1956	1.9179	1.6042	1.2105	1.9137	1.581	1.1032	1.6992	1.5403

g35.mat

0	3.7863	6.2747	1.6572	3.8333	6.2411	1.6281	2.0246	3.4752	1.7165
10	3.7863	6.2747	1.6572	3.8333	6.2411	1.6281	2.0246	3.4752	1.7165
20	3.7862	6.2738	1.657	3.8332	6.2405	1.628	2.0246	3.475	1.7164
30	3.785	6.2604	1.654	3.8321	6.2285	1.6254	2.024	3.4691	1.714
40	3.7821	6.2305	1.6474	3.8286	6.1972	1.6187	2.0219	3.4517	1.7072
50	3.7764	6.1812	1.6368	3.8217	6.1434	1.6075	2.0176	3.42	1.6951
60	3.7675	6.1124	1.6224	3.8106	6.067	1.5921	2.0101	3.3726	1.6778
70	3.7553	6.0276	1.6051	3.7958	5.9727	1.5735	1.9996	3.3114	1.656
80	3.7478	5.979	1.5953	3.7867	5.9188	1.5631	1.9928	3.2751	1.6434
90	3.7293	5.8675	1.5734	3.7646	5.7958	1.5395	1.9755	3.1889	1.6142
100	3.7182	5.8047	1.5611	3.7517	5.7269	1.5265	1.9649	3.139	1.5976
110	3.706	5.7381	1.5483	3.7375	5.6539	1.5127	1.953	3.085	1.5796
120	3.6922	5.6667	1.5348	3.7219	5.5764	1.4983	1.9399	3.027	1.5604
140	3.5446	5.3234	1.5018	3.5978	5.2729	1.4656	1.9067	2.8957	1.5187
160	3.0267	4.4771	1.4792	3.1454	4.5536	1.4477	1.8594	2.7836	1.4971
180	2.1744	3.2458	1.4927	2.2797	3.3362	1.4634	1.7004	2.5183	1.481
200	1.0428	1.6536	1.5858	1.0724	1.6752	1.5621	0.9889	1.4999	1.5166

g50.mat

0	1.4452	2.6812	1.8552	1.4807	2.7191	1.8364	0.88457	1.7117	1.9351
10	1.4452	2.6812	1.8553	1.4807	2.7192	1.8364	0.88457	1.7117	1.9351
20	1.4452	2.6807	1.855	1.4806	2.7189	1.8363	0.88455	1.7116	1.935
30	1.4445	2.6736	1.8508	1.48	2.7124	1.8326	0.88423	1.7084	1.9321
40	1.4429	2.6571	1.8415	1.4781	2.6951	1.8233	0.88312	1.6988	1.9237
50	1.4397	2.6295	1.8264	1.4743	2.665	1.8077	0.88068	1.6811	1.9089
60	1.4347	2.5903	1.8055	1.468	2.6215	1.7858	0.87646	1.6541	1.8872
70	1.4275	2.5407	1.7798	1.4593	2.5665	1.7587	0.87027	1.6183	1.8595
80	1.423	2.5117	1.765	1.4538	2.5343	1.7432	0.86617	1.5965	1.8432
90	1.4115	2.4432	1.7309	1.4402	2.4588	1.7073	0.85537	1.5434	1.8043
100	1.4045	2.4036	1.7114	1.4319	2.4154	1.6868	0.84854	1.5117	1.7815
110	1.3965	2.3608	1.6905	1.4228	2.3686	1.6648	0.84077	1.4768	1.7565
120	1.3877	2.3149	1.6681	1.4127	2.3185	1.6412	0.83204	1.4387	1.7291
140	1.3675	2.2147	1.6195	1.3899	2.2098	1.5899	0.81186	1.3539	1.6676
160	1.354	2.1574	1.5934	1.3755	2.149	1.5623	0.80044	1.3076	1.6336
180	1.3165	2.0623	1.5665	1.3409	2.0576	1.5345	0.78682	1.2573	1.598
200	0.8573	1.3328	1.5546	0.8932	1.3644	1.5274	0.68338	1.053	1.5408

g65.mat

0	1.1872	2.2223	1.8719	1.2	2.1109	1.7591	0.71766	1.2954	1.8051
10	1.1872	2.2223	1.8719	1.2	2.1109	1.7591	0.71766	1.2954	1.8051
20	1.1872	2.2219	1.8715	1.2	2.1107	1.759	0.71765	1.2954	1.8051
30	1.1867	2.2161	1.8674	1.1996	2.1067	1.7562	0.71748	1.2937	1.8031
40	1.1855	2.2034	1.8586	1.1985	2.0964	1.7492	0.7169	1.2887	1.7976
50	1.1833	2.1826	1.8445	1.1963	2.0787	1.7376	0.71561	1.2793	1.7878
60	1.1798	2.1533	1.8251	1.1927	2.0529	1.7212	0.71334	1.2649	1.7732
70	1.1749	2.1165	1.8014	1.1876	2.0198	1.7008	0.7099	1.2452	1.7541
80	1.1718	2.0948	1.7877	1.1843	2.0002	1.689	0.70756	1.233	1.7426
90	1.1637	2.0435	1.756	1.1758	1.9533	1.6612	0.70119	1.2024	1.7148
100	1.1587	2.0138	1.7379	1.1706	1.9259	1.6452	0.69705	1.1836	1.698
110	1.1531	1.9814	1.7183	1.1647	1.8959	1.6278	0.69225	1.1626	1.6794
120	1.1468	1.9465	1.6974	1.1581	1.8633	1.609	0.68675	1.1391	1.6587
140	1.1321	1.8699	1.6517	1.1429	1.7913	1.5674	0.67374	1.0858	1.6116
160	1.1223	1.826	1.627	1.1331	1.7504	1.5449	0.66623	1.0561	1.5852
180	1.0952	1.753	1.6006	1.1088	1.687	1.5215	0.65705	1.0233	1.5574
200	0.7340	1.1562	1.5752	0.7614	1.1501	1.5103	0.57862	0.8745	1.5115

g85.mat

0	0.9129	1.6211	1.7757	0.9227	1.525	1.6526	0.5571	0.9362	1.6804
10	0.9129	1.6211	1.7757	0.9227	1.525	1.6526	0.5571	0.9362	1.6804
20	0.9128	1.6208	1.7755	0.9227	1.524	1.6525	0.5571	0.9361	1.6804
30	0.9126	1.618	1.7729	0.9226	1.5231	1.6509	0.5570	0.9354	1.6794
40	0.9120	1.6118	1.7671	0.9221	1.5185	1.6467	0.5568	0.9333	1.6763
50	0.9109	1.6015	1.758	0.9211	1.5104	1.6397	0.5562	0.9293	1.6707
60	0.9092	1.5868	1.7453	0.9194	1.4986	1.6298	0.5552	0.9229	1.6623
70	0.9066	1.568	1.7294	0.9169	1.483	1.6172	0.5536	0.9140	1.6509
80	0.9049	1.5566	1.7201	0.9153	1.473	1.6097	0.5525	0.9083	1.6439
90	0.9005	1.529	1.698	0.9109	1.4499	1.5916	0.5493	0.8933	1.6263
100	0.8976	1.5126	1.685	0.9081	1.4356	1.5809	0.5471	0.8838	1.6153
110	0.8943	1.4943	1.6708	0.9048	1.4197	1.569	0.5446	0.8728	1.6028
120	0.8906	1.4743	1.6554	0.9010	1.402	1.5559	0.5415	0.8603	1.5887
140	0.8816	1.4294	1.6212	0.8921	1.3618	1.5264	0.5341	0.8309	1.5555
160	0.8755	1.4029	1.6023	0.8862	1.3382	1.51	0.5297	0.8141	1.5367
180	0.8579	1.3568	1.5815	0.8706	1.2994	1.4926	0.5242	0.7949	1.5165
200	0.5953	0.9255	1.5546	0.6178	0.9158	1.4824	0.4680	0.6936	1.4822